Large Eddy Simulation of complex flow over submerged bodies

A DISSERTATION
SUBMITTED TO THE FACULTY OF THE GRADUATE SCHOOL
OF THE UNIVERSITY OF MINNESOTA
BY

Praveen Kumar

IN PARTIAL FULFILLMENT OF THE REQUIREMENTS
FOR THE DEGREE OF
DOCTOR OF PHILOSOPHY

Krishnan Mahesh, Adviser

February, 2018

Acknowledgements

First and foremost, I am grateful to my adviser Prof. Krishnan Mahesh for giving me the opportunity to pursue my doctoral research in his group and for his constant support. He is very approachable, attentive and always keen to discuss and address problems. I have learned a lot from his profound knowledge and experience.

I thank Prof. Ellen Longmire, Prof. Thomas Schwartzentruber and Prof. Michele Guala for being on my examination committee and reviewing my thesis. I am also thankful to Prof. Mihailo Jovanović for being part of my preliminary examination committee. I thank Dr. Peter Chang and his colleagues at the Naval Surface Warfare Center Carderock Division (NSWCCD) for providing us with experimental data for the propeller simulations. This work was supported by the United States Office of Naval Research (ONR) under ONR Grant N00014-14-1-0289 with Dr. Ki-Han Kim as technical monitor. Computing resources were provided by the High Performance Computing Modernization Program (HPCMP) of the Department of Defense, the Innovative and Novel Computational Impact on Theory and Experiment (INCITE) program of the Department of Energy, the Extreme Science and Engineering Discovery Environment (XSEDE) supported by the National Science Foundation and the Minnesota Supercomputing Institute (MSI). I would like to acknowledge Mr. Ray Muno and the entire ENET team for their help and technical support.

The Mahesh research group is very friendly and diverse, which is fun to work in. I had the pleasure to work with very smart and hard working people in the group. I am grateful to Dr. Aman Verma for helping me get started with the codes and relevant literature. Dr. Prahladh Iyer and Dr. Aswin Gnanaskandan are gratefully

acknowledged for teaching me mesh generation and for mentoring me during my initial years in the graduate school. I am thankful to Mr. Karim Alame, Mr. Wyatt Horne and Ms. Yixuan Li for numerous discussions and banters we had. I have benefited a lot from my interaction with the other members of the group, some of whom include Dr. Rajapandiyan Asaithambi, Mr. Jacob Keller, Mr. Marc Regan, Mr. Sreevatsa Anatharamu, Mr. Mrugank Bhatt, Mr. Aditya Madabhushi, Ms. Rong Ma, Mr. Thomas Kroll and Mr. Filipe Brandao. I made many friends outside my lab, who enriched my graduate school experience. Special thanks to my roommates Aditya, Abhineet and Harsh for making my life interesting. I am also thankful to Narendra, Sidharth, Maninder and all other friends for making my stay at the graduate school fun and memorable.

Lastly, I owe a lot to my parents Mr. Sunil Kumar Mishra and Mrs. Kanti Jha, and my younger siblings Rakhi and Prabhat for their constant support. My achievements would not be possible without them.

To my family

Abstract

Predicting the complex flow over a submerged marine vessel in maneuver has two major challenges: the hull boundary layer and the flow due to the propeller. Large eddy simulation (LES) using the dynamic Smagorinsky model (DSM) [1, 2] and discrete kinetic energy conserving numerical method of Mahesh et al. [3] has successfully predicted complex flows in the past. This dissertation discusses four advancements towards reliably using LES to predict and understand the complex flows encountered during maneuvers of submerged marine vessels: (1) understanding skin-friction in axisymmetric boundary layers evolving under pressure gradients, (2) simulating attached flow over axisymmetric hulls and wake evolution, (3) assessing the dependence of the stern flow and axisymmetric wake on hull boundary layer characteristics, and (4) simulating flow through a propeller at design operating condition.

Axisymmetric boundary layers are studied using integral analysis of the governing equations for axial flow over a circular cylinder. The analysis includes the effect of pressure gradient and focuses on the effect of transverse curvature on boundary layer parameters such as shape factor (H) and skin-friction coefficient (C_f), defined as $H = \delta^*/\theta$ and $C_f = \tau_w/(0.5\rho U_e^2)$ respectively, where δ^* is displacement thickness, θ is momentum thickness, τ_w is the shear stress at the wall, ρ is density and U_e is the streamwise velocity at the edge of the boundary layer. Useful relations are obtained relating the mean wall-normal velocity at the edge of the boundary layer (V_e) and C_f to the boundary layer and pressure gradient parameters. The analytical relations reduce to established results for planar boundary layers in the limit of infinite radius of curvature. The relations are

used to obtain C_f which shows good agreement with the data reported in the literature. The analytical results are used to discuss different flow regimes of axisymmetric boundary layers in the presence of pressure gradients.

Wall-resolved LES is used to simulate flow over an axisymmetric body of revolution at a Reynolds number, $Re = 1.1 \times 10^6$, based on freestream velocity and the length of the body. The geometry used in the present work is an idealized submarine hull (DARPA SUBOFF without appendages) at zero angle of pitch and yaw. The computational domain is chosen to avoid confinement effects and capture the wake up to fifteen diameters downstream of the body. The unstructured computational grid is designed to capture the fine near-wall structures as well as the wake. LES results show good agreement with the available experimental data. The axisymmetric turbulent boundary layer has higher skin-friction and higher radial decay of turbulence away from the wall, compared to a planar turbulent boundary layer under similar conditions. The mean streamwise velocity exhibits self-similarity, but the turbulent intensities are not self-similar over the length of the simulated wake, consistent with previous studies reported in the literature. The axisymmetric wake transitions from high-Re to low-Re equilibrium self-similar solutions, as theoretically proposed and observed for axisymmetric wakes in the past.

The recycle-rescale method of Lund et al. [4] is first implemented for unstructured grids and massively parallel platforms and then extended to spatially developing thin axisymmetric turbulent boundary layers. LES of flow over the stern portion of the hull is performed with a prescribed turbulent inflow at a momentum thickness $\theta/a = 0.078$ and a momentum thickness-based Reynolds number $Re_\theta = 2000$, where a is the radius of curvature, to understand the dependence of the flow field in the stern region and the wake, on hull boundary layer characteristics. Additional simulations are performed to study the effect of Re_θ and θ/a at the inflow. The turbulent inflows needed for the simulations are generated from auxiliary simulations employing the recycle-rescale methodology. Results are compared to past studies, and used to describe the effect of incoming TBL on the overall flow field. The pressure coefficient on the body is largely insensitive to the incoming boundary layer characteristics, except in the vicinity

of flow separation, where it is more sensitive to θ/a. Skin-friction on the other hand, is very sensitive to the boundary layer characteristics. The boundary layer characteristics determine the location of flow separation and hence, the flow field in the stern region and the wake. The wake of the body is more sensitive to Re_θ compared to θ/a.

The wake of a five-bladed marine propeller at design operating condition is studied using LES. The mean loads and phase-averaged flow field show good agreement with experiments. Phase-averaged and azimuthal-averaged flow fields are analyzed in detail to examine the mechanisms of wake instability. The propeller wake consisting of tip and hub vortices undergoes streamtube contraction, which is followed by the onset of instabilities as evident from the oscillations of the tip vortices. Simulation results reveal a mutual induction mechanism of instability where instead of the tip vortices interacting among themselves, they interact with the smaller vortices generated by the roll-up of the blade trailing edge wake in the near wake. It is argued that although the mutual-inductance mode is the dominant mode of instability in propellers, the actual mechanism depends on the propeller geometry and the operating conditions. The axial evolution of the propeller wake from near to far field is discussed. Once the propeller wake becomes unstable, the coherent vortical structures break up and evolve into the far wake composed of a fluid mass swirling around an oscillating hub vortex. The hub vortex remains coherent over the length of the computational domain.

Contents

List of Tables

List of Figures

Chapter 1

Introduction

1.1 Motivation

The use of computational fluid dynamics (CFD) for the development of engineering devices is becoming more popular in recent years with the advent of powerful supercomputers. Fluid flows are being simulated using various methodologies depending on the nature of the flow problem and the availability of computational resources. These methodologies can be broadly categorized into potential methods, Reynolds Averaged Navier–Stokes (RANS), large eddy simulation (LES) and direct numerical simulation (DNS). Potential methods offer the quickest turnaround, yield accurate surface pressure for attached flows, and are invaluable for initial design. In DNS, all relevant scales of motion are resolved accurately in space and time, and no model is used. However, the computational cost associated with DNS has limited its use to study turbulent flows in simple geometries [3]. The numerical simulations of fluid problems for engineering applications are most commonly performed using RANS methods. In general, RANS models work well for steady, attached flows but fail for the flow problems where the underlying physics is dominated by large scale unsteady phenomena. LES is an intermediate method between DNS and RANS in which the large scales of motion are resolved, whereas the effect of small scales is modeled. LES is an attractive approach to predict complex turbulent flows because of its better accuracy over RANS and cheaper

computational cost than DNS.

A variety of complex hydrodynamic phenomena affect the overall performance of marine vessels. The turbulent flow affects the hydrodynamic drag, propulsor performance, structural integrity, control-surface effectiveness, and acoustic signature of the vessel. LES is well suited to study such complex turbulent flows [7]. A model marine vessel is shown in Figure 1.1(a). The hull of the vessel is a generic submarine model called DARPA SUBOFF with sail and appendages (AFF8) [5]. The propeller DTMB 4381 [6] is attached to the hull at $0.978L$ from the nose, where L is the length of the hull. The axisymmetric (unappended) hull (AFF1) and the propeller are shown separately in Figures 1.1(b) and (c) respectively. The Re of flow over such marine vessels is typically $\sim O(10^7)$, based on the freestream and length of the hull. Currently, RANS and hybrid variants of RANS-LES methods such as Detached Eddy Simulation (DES), Delayed Detached Eddy Simulation (DDES) etc are used to simulate such high Re flows.

The remainder of this chapter is organized as follows. Section 1.2 provides a brief review of past work relevant to this dissertation, followed by an overview of the principal contributions in Section 1.3, and outline in Section 1.4.

1.2 Review of past work

1.2.1 Axisymmetric boundary layers

Turbulent boundary layers (TBL) are one of the most studied canonical fluid problems, but most past studies are devoted to the flat plate (planar) TBL. A recent review by Smits et al. [8] describes the current understanding and future challenges of wall-bounded flows at high Re. A variety of hydrodynamic engineering applications however, involve axisymmetric TBL, which involve an additional length scale parameter to account for curvature. Several engineering applications have axisymmetric TBL evolving under the influence of pressure gradients due to their geometrical shapes.

The radius-based Reynolds number ($Re_a = aU/\nu$, where U is freestream velocity, ν is kinematic viscosity and a is the radius of cylinder) does not include any effect of wall-shear stress or boundary layer thickness. Therefore, popular non-dimensional

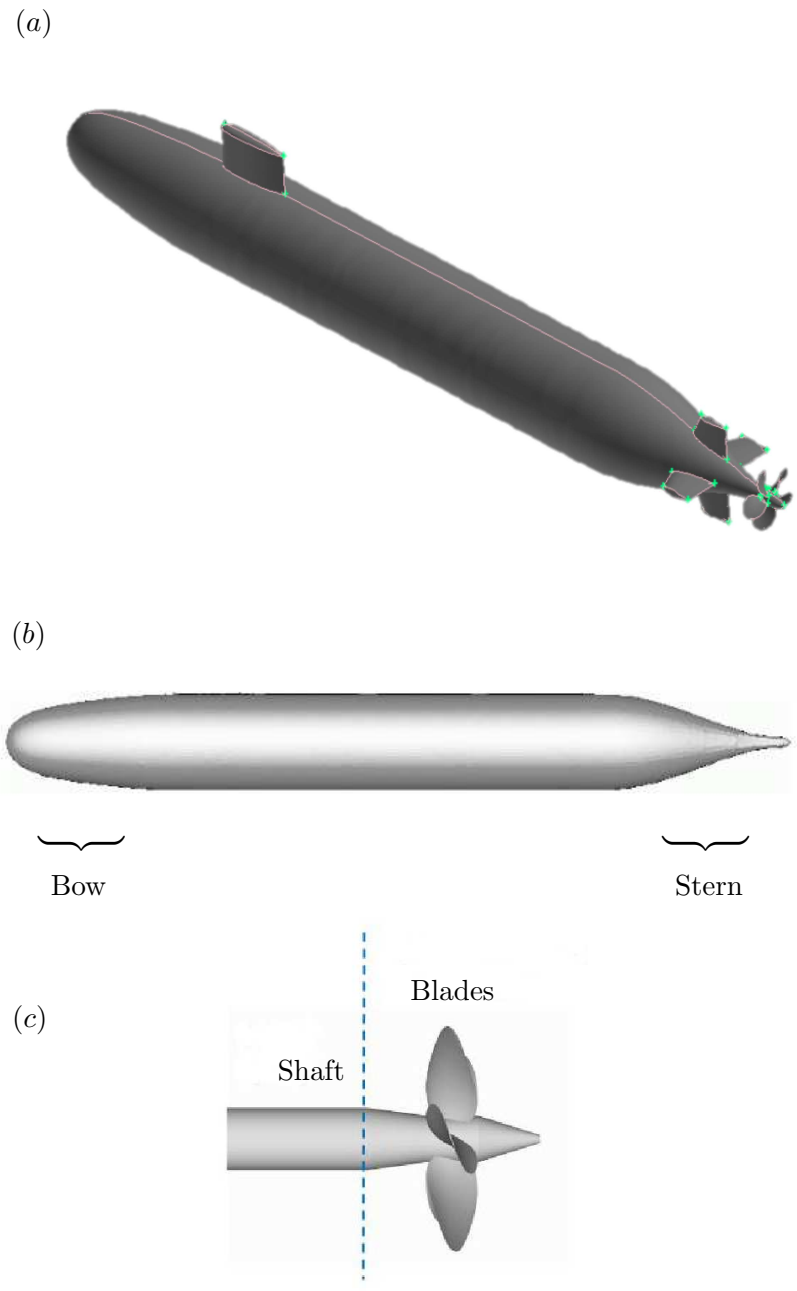

Figure 1.1: (a) DARPA SUBOFF model (AFF8) [5] with propeller DTMB 4381 [6], (b) the axisymmetric hull and (c) the propeller.

parameters to characterize axisymmetric TBL are the ratio of boundary layer thickness to the radius of curvature (δ/a) and the radius of curvature in wall units (a^+). Based on these two parameters, three regimes can be identified [9]: (i) both δ/a and a^+ are large, (ii) large δ/a and small a^+ and (iii) small δ/a and large a^+. The first flow regime is observed for axial flow over a long slender cylinder at high Re, where the effect of curvature is large. The second flow regime is realized for axial flow over slender cylinders at low Re, where the axisymmetric TBL behaves like an axisymmetric wake with an inner layer with strong curvature and low-Re effects. Almost all the experimental studies reported in the literature have focused on the first two regimes [9]. The third flow regime is common in applications where the Reynolds number is high but the boundary layer is thin compared to the radius of curvature. Usually, this flow regime is treated as a planar boundary layer where the curvature effects are assumed to be minimal. Although, there are significant fundamental differences between a planar TBL and a thin axisymmetric TBL at high Re, such as increased skin-friction and rapid radial decay in turbulence away from the wall [10].

One of the earliest analytical investigations of the effect of transverse curvature on skin-friction was conducted by Landweber [11], who used a $1/7^{th}$-power-law for velocity profile and the Blasius skin-friction law [12] to show that for a given momentum thickness (θ) -based Reynolds number (Re_θ), axisymmetric boundary layers have higher skin-friction and lower boundary layer thickness in comparison to planar boundary layers. Seban and Bond [13] analyzed the laminar boundary layer for axial flow over a circular cylinder from the governing boundary layer equations and showed that the skin-friction and heat-transfer coefficients for axisymmetric laminar boundary layers are higher than those obtained from the Blasius solution. Kelly [14] introduced an important correction to their solution, known as the Seban–Bond–Kelly (SBK) solution for zero pressure gradient (ZPG) axisymmetric boundary layers. The SBK solution was extended to the regime of large curvature effect, as encountered in axial flow over long thin cylinders by Glauert and Lighthill [15]. Stewartson [16] provided an asymptotic solution for ZPG laminar axial flow over long thin cylinders.

Axisymmetric TBL have not received the same attention as planar TBL likely due

to the inherent difficulties in keeping the flow perfectly axial and preventing sagging or elastic deformation of the cylinders. The effect of curvature has been the focus of most past studies. Richmond [17] and Yu [18] conducted the first few experimental studies for curvature effects on boundary layers, which were followed by extensive experimental studies [19–28] showing that the transverse curvature indeed has a significant effect on the overall behavior of axisymmetric TBL.

Afzal and Narasimha [29] analyzed thin axisymmetric TBL at high Re (regime 3 described above) using asymptotic expansions and modified the well-known law of the wall for planar TBL to include the effect of curvature. The wall-normal distance in wall units, y^+ was modified as,

$$y^+ \quad = \quad a^+ ln(1 + y^+/a^+) \tag{1.1}$$

where, $a^+ = au_\tau/\nu$ is the radius of curvature in wall-units. Using this modified y^+, it was shown that there exists a log layer in the mean velocity profile similar to that found in planar TBL, with same slope but the intercept (B) is a weak function of curvature ($B = 5 + 236/a^+$). It has been shown that the relation $U^+ = a^+ log(1 + y^+/a^+)$ is valid in the sublayer region, but the use of y^+ from Eq. 1.1 instead of the planar y^+ in the logarithmic region assumes that transverse curvature affects both the viscous sublayer and log layer identically.

One of the earliest numerical simulations of axisymmetric boundary layers was performed by Cebeci [20], who showed higher skin-friction compared to flat plate prediction in both laminar and turbulent regimes. Similar behavior of skin-friction was observed in numerous subsequent simulations of axisymmetric TBL. Axisymmetric TBL over long thin cylinders have been extensively studied by Tutty [30] using RANS and Jordan [31, 32, 33, 34] using DNS and LES. Jordan used his simulation database to propose simple models for the skin-friction [32] and the flow field [34]. None of the studies mentioned so far have considered pressure gradient effects. Experiments by Fernholz and Warnack [35] and Warnack and Fernholz [36] considered axisymmetric TBL under favorable pressure gradient (FPG) in internal flow.

Boundary layers under adverse pressure gradients (APG) have been studied in the past using asymptotic expansions (See Afzal [37, 38] and references therein). Wei and Klewicki [39] performed integral analysis of the governing equations for ZPG planar boundary layers and obtained

$$\frac{U_e V_e}{u_\tau^2} = H, \tag{1.2}$$

where U_e and V_e are the mean streamwise and wall-normal velocity respectively, H is the shape factor and $u_\tau = \sqrt{\tau_w/\rho}$ is the friction velocity. The analysis was later extended for planar boundary layers under pressure gradient by Wei et al. [40], who modified Eq. 1.2 as,

$$\frac{U_e V_e}{u_\tau^2} = H + (1 + \delta/\delta^* + H)\beta_{RC} \tag{1.3}$$

where β_{RC} is the Rotta–Clauser pressure gradient parameter [41, 42], δ^* is the displacement thickness and δ is the boundary layer thickness. β_{RC} is often used to quantify the strength of APG in boundary layer flows.

1.2.2 Hull wakes

Wakes are canonical shear flows, which are the subject of numerous past studies. The wakes generated by streamlined bodies at high Re are particularly important because of their relevance to many engineering applications. Axisymmetric wakes have been studied in the past but a large number of those studies are devoted to the wakes of blunt axisymmetric bluff bodies [43]. The wakes generated by streamlined bodies on the other hand, have not received similar attention. Such wakes are more sensitive to the boundary layer characteristics on the wake generator as compared to blunt bluff bodies. Turbulent wakes are expected to attain self-similarity and become Reynolds number independent away from the wake generator as proposed by Townsend [44]. Streamlined bodies usually have smaller turbulence production within the flow separation region compared to bluff bodies, which assists in achieving self-similarity away from the wake

generator. Scaling laws can be derived for mean centerline deficit and wake width [45].

The SUBOFF geometry has been used in numerous past experiments and simulations. Huang et al. [46] conducted SUBOFF experiments with and without appendages at $Re = 1.2 \times 10^7$ and reported pressure, skin-friction and profiles of velocity statistics on the hull. Jiménez et al. [47] experimentally studied the evolution of the wake of the bare hull at $Re = 1.1 \times 10^6$ to 6.7×10^7. Jiménez et al. [48] studied the effect of fins (appendages) on the intermediate wake of the fully-appended SUBOFF. Yang and Löhner [49] accurately computed pressure and skin-friction coefficients using RANS equations. Kim et al. [50] performed RANS simulations for turning maneuver of the SUBOFF. The capabilities of DES and LES to accurately predict flow over SUBOFF, both appended and unappended are reviewed by Alin et al. [51]. There are numerous other computational studies employing RANS, DES and DDES techniques to study flow over SUBOFF [52–54]. Posa and Balaras [55] performed wall-resolved LES of flow over the fully-appended SUBOFF at $Re = 1.2 \times 10^6$, i.e. conditions similar to the experiments of Jiménez et al. [48]. Their study was focused on the effect of the appendages and the interaction of the junction flows created by the appendages with the wake. The complex wake parameters were evaluated and compared to the measurements of Jiménez et al. [48].

There are two main challenges associated with studying turbulent wakes generated by streamlined bodies: the thin hull boundary layer and long wake development length. Computationally, this requires fine grid resolution for a long domain devoid of confinement effects to capture near-wall structures as well as wake evolution. Additionally, the numerical scheme should avoid unphysical dissipation of the velocity fluctuations, which decrease as the wake evolves away from the wake generator.

1.2.3 Separated shear layers

An important feature of flow over streamlined bodies is the separated shear layer, which is formed when the attached boundary layer on the body separates due to the adverse pressure gradient. The behavior of the separated shear layer depends on the characteristics of the boundary layer on the body. A large number of past studies have been

dedicated to understand the behavior of separated shear layers, usually occurring in simple geometries [56–58], highlighting their multiscale nature and the effect of shear layer entrainment on the behavior of such flows (see Ref. [59] and references therein). Recently, Stella et al. [59] experimentally studied the separated shear layers formed by flow over a ramp with emphasis on mass entrainment effects and their scaling behavior. They showed that the large-scale mass entrainment properties of separated shear layers depend on the incoming boundary layer and its turbulence.

One of the earliest experimental studies of axisymmetric flow over a streamlined body of revolution were conducted by Patel [23], who reported velocity and pressure profiles in the thick axisymmetric TBL near the tail of the body. Since then, there have been many experimental studies on axisymmetric geometries, usually comprising a cylindrical mid body and conical fore and aft portions [60–62]. The influence of boundary layer thickness on the base pressure and near-wake flow features of a blunt-based axisymmetric body was experimentally studied by Mariotti and Buresti [63]. A survey of existing literature reveals scarcity of similar studies for a streamlined body of revolution.

1.2.4 Propeller wakes

Rotors form an integral part of many modern engineering devices such as propellers, helicopters and wind turbines. The wakes generated by these rotor systems contain complex vortical structures which evolve from near field to far field in a complex physical fashion. It is important to understand the physics of rotor wakes in order to predict the performance of rotor systems, and to better design and optimize rotors for their use in engineering applications. The wake of a typical N-bladed rotor consists of a system of single hub vortex or N root vortices and N helical tip vortices, one generated from each blade. For each blade, the tip vortex is connected to the hub vortex by a thin vortex sheet which is shed by the blade trailing edge as a result of spanwise varying circulation. The strength of these vortices depends on the operating condition of the rotor and the blade design. Rotor wakes may be categorized into near and far wake. In the near wake, the signature of the blades such as tip vortices and trailing edge wake can be

observed. These flow structures become unstable and evolve downstream to form the far wake, where the flow field loses the memory of blade geometry and the fluid mass swirls around the hub vortex.

Joukowski [64] was the first to propose a wake model for a two-bladed propeller. It consisted of two rotating helical tip vortices of strength Γ and an axial root vortex of strength -2Γ, where Γ is the circulation on each blade. Since then, there have been numerous theoretical studies conducted to understand the mechanisms of wake instabilities. The earliest work on stability analysis of a single helical vortex filament was performed by Levy and Forsdyke [65] which was later extended by Widnall [66]. Her inviscid linear stability analysis showed that an isolated vortex filament is susceptible to three modes of instabilities, namely short-wave, long-wave and mutual-inductance. Gupta and Loewy [67] simulated the far wake of a rotor as multiple helices and found it to be inherently unstable. Their simulations were performed assuming a fixed value of pitch and vortex core radius. Okulov [68] analytically obtained the solution to this problem as well and reached the conclusion that Joukowski's far wake model is unconditionally unstable for all pitch values. Numerous experimental visualizations have shown that helical vortices can be stable even for small pitch [69]. Okulov and Sørensen [70] extended the analysis of Okulov [68] to include the effect of hub/root vortices by assigning a vortex field formed by the circulation of the hub vortex. They concluded that an assigned vorticity field accounting for the blade trailing edge vortex sheets can indeed stabilize the otherwise unconditionally unstable wake as described by the Joukowski model consisting of N tip helical vortices and a slender hub/root vortex.

There are numerous experimental works for marine propellers [71–77], helicopter rotors [78–80] and wind turbines [81–84], that study rotor wakes; however the complex dynamics of such flows are still not well-understood. In the present paper, we will study the flow over a marine propeller using large-eddy simulation. However, the general theory and wake description of propellers can be applied to other rotors too.

Felli et al. [77] categorized the behavior of rotor wakes into: (i) rotor wake transition to instability, (ii) wake evolution in transition and far field and (iii) tip and hub vortex breakdown. They studied the effect of number of blades and spiral-to-spiral distance on

the destabilization of root and tip vortices in transition and far wake. They observed that the tip vortices get destabilized first causing subsequent destabilization of hub vortex. Also, the energy transfer mechanism in the wake was found to be dependent on the number of blades. Nemes et al. [85] performed experiments for a two-bladed rotor and concluded that the mutual inductance mode drives the transition to an unstable wake as suggested by Felli et al. [77]. The experimental study of mechanisms triggering instabilities in the rotor wake is challenging because of the sensitivity of the wake to perturbations in the incoming flow as well as limitations including tunnel effect and dimensions of the test section. In order to avoid any perturbation in the inflow caused by potential asymmetry due to multiple blades, Quaranta et al. [86] conducted experiments with a one-bladed rotor to study the long-wave instability mechanism as predicted by Widnall [66] and Gupta and Loewy [67].

The computational study of this problem is challenging due to resolution requirements and the size of the computational domain in order to accurately capture the tiny vortex cores of the tip vortices as well as the entire evolution of wake from near field to far field. Traditionally, potential methods have been used to design and predict the flow behind a marine propeller [87]. Di Felice et al. [88] performed wall-modeled LES of the wake of a seven-bladed propeller (INSEAN E1619). Di Mascio et al. [89] used DES to simulate the flow over a four-bladed propeller in pure axial flow and at 20 degrees of drift at two advance ratios and studied the effect of secondary vortices formed in drift. They used the same blade geometry (E779A) as that used by Felli et al. [77]. Baek et al. [90] used RANS simulations to study the effect of advance ratio on the evolution of the propeller wake. Based on their results, they suggested empirical models of the radial trajectory and the pitch of the tip vortices. Chase and Carrica [53] performed computations for a marine propeller (INSEAN E1619) using the overset methodology. Balaras et al. [91] performed LES of the same propeller as that used by Chase and Carrica [53] using the immersed-boundary method and analyzed the flow physics.

The marine propeller DTMB 4381 has been used in the past to perform LES of crashback flows [92–100] because of the availability of extensive experimental data. In the present dissertation, LES of the forward mode of operation of the same propeller is

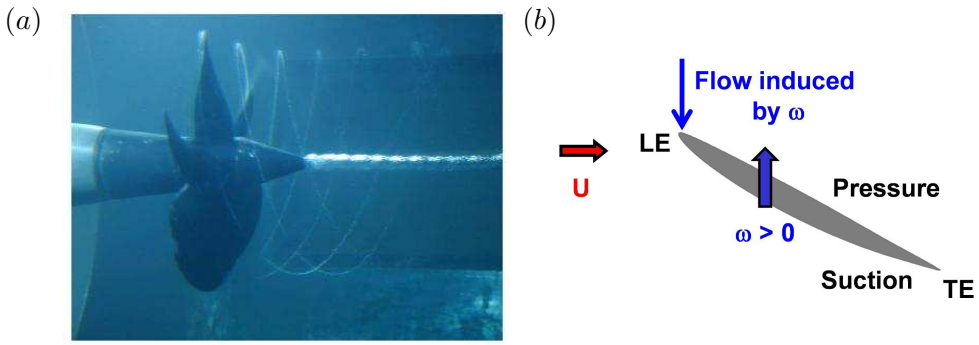

Figure 1.2: (a) Flow visualization of forward mode at $J = 0.3$ [101] and (b) location of leading, trailing edges, and pressure, suction sides on blade section.

conducted due to availability of particle image velocimetry (PIV) data.

Figure 1.2(a) shows a picture taken from a water tunnel experiment where the forward mode of operation is visualized. A system of helical tip vortices and an axial hub vortex can be clearly seen. Note that the cross-section of the tip vortices are very small. A cylindrical cross-section of a propeller blade is an airfoil; a schematic of the flow field around the airfoil is shown in Figure 1.2(b). The flow approaching the airfoil is the vector sum of freestream and the flow induced by propeller rotation. The pressure difference generated between the pressure and suction sides of the blades creates net thrust and torque.

1.3 Overview

This dissertation aims to develop the predictive capability of LES for marine vessels, which involve complex flows due to the geometry and high Re. There are two major challenges associated with simulating flow over an entire hull: (i) the boundary layer on the hull and (ii) the flow due to propeller rotation. The hull boundary layer is challenging because of the small turbulent near-wall motions that determine drag. The flow due to propeller rotation produces complex wakes depending on the direction and the magnitude of rotational speed. A forward rotating propeller generates a wake, comprising hub and tip vortices along with blade trailing edge vortex sheets whereas, a

reverse rotating propeller generates a massive flow separation on the blades and the flow through the propeller disc interacts with the incoming flow to form a ring vortex. Both these propeller flows have their own challenges. The resolution requirements for LES demands high quality large grids, which is challenging for complex geometries. The flow over a reverse rotating propeller (crashback mode) has been predicted accurately using LES in the past [93–99, 102]. So, the propeller flows in this dissertation are restricted to forward mode.

The principal contributions of this work are as follows:

- Axisymmetric boundary layers under pressure gradients are studied using integral analysis of the governing equations. Useful relations are obtained which relate the wall-normal velocity at the edge of the boundary layer and the skin-friction to the pressure gradient and boundary layer parameters. The derived relations are used to obtain skin-friction which shows good agreement with the data reported in the literature for both laminar and turbulent axisymmetric boundary layers.

- Wall-resolved LES is performed for flow over an axisymmetric hull (DARPA SUBOFF without appendages) at $Re = 1.1 \times 10^6$, based on hull length and freestream velocity, showing good agreement with the available experimental data. Care has been taken to eliminate confinement effects and capture essential flow features. The grid resolution and length of the simulated wake are significantly higher than most past work. Results show higher skin-friction compared to the corresponding planer boundary layer. For the first time, the axisymmetric wake of a streamlined body is shown to transition from high-Re to low-Re equilibrium self-similar solutions, as theoretically proposed and observed for axisymmetric wakes of bluff bodies in the past.

- The recycle-rescale method of Lund et al. [4] is implemented for unstructured grids on parallel platforms and extended to spatially developing thin axisymmetric TBL. The algorithm is extensively validated for both planar and axisymmetric TBL for a range of momentum thickness (θ) -based Reynolds number (Re_θ). The algorithm is used to generate desired turbulent inflows used to study stern flows and wakes.

- The dependence of stern flow and the axisymmetric wake on the hull boundary layer characteristics is studied using LES. Results show that the pressure coefficient on the body is largely insensitive to the incoming boundary layer characteristics, except in the vicinity of flow separation, whereas the skin-friction coefficient is very sensitive. The hull boundary layer determines the location of the flow separation and hence, the overall flow field in the stern region and the wake. The wake is more sensitive to Re_θ compared to θ of the hull boundary layer.

- LES is performed for a marine propeller in forward mode of operation at design operating condition i.e. at an advance ratio, $J = 0.889$ and $Re = 894000$, based on freestream velocity and propeller diameter. The level of resolution and the length of the wake captured goes beyond what has been reported in the literature, to the best of our knowledge. The entire evolution of propeller wake from near to far field has been captured and explored in detail. LES results show good agreement with experiments for mean loads and time-averaged flow field. The flow field of complex wake is analyzed to reveal the mechanism of instabilities in the wake. A physical mechanism of mutual inductance mode of instabilities is observed and explained.

1.4 Outline

This dissertation is organized as follows. Chapter 2 describes the governing equations, sub-grid stress model for LES along with dynamic Lagrangian averaging, the algorithm/numerical discretization for unstructured grids and the turbulent inflow generation method used to generate thin axisymmetric boundary layers. The integral analysis of axisymmetric boundary layers under pressure gradients is discussed in Chapter 3. LES of flow over the hull is described in Chapter 4. The dependence of the stern flow and the wake on the hull boundary layer characteristics is studied in Chapter 5. LES of a marine propeller at design operating condition is studied in the forward mode of operation in Chapter 6. The tripping of the boundary layer in the hull simulations (Chapter 4) is discussed in Appendix A.

Chapter 2

Numerical method

The chapter is organized as follows. The governing equations are discussed in Section 2.1. The LES equations are described in Section 2.2, followed by a discussion of the sub-grid stress model employed in this dissertation in Section 2.3. The dynamic averaging is motivated and the employed dynamic Lagrangian averaging is briefly described in Section 2.4. Section 2.5 describes the numerical discretization. Section 2.6 is devoted to the turbulent inflow generation used in Chapter 5 of this dissertation.

2.1 Governing equations

The Navier–Stokes (N–S) equations provide a continuum description of a single phase fluid flow. The three-dimensional, incompressible, constant density N–S equations for a Newtonian fluid in an inertial frame of reference are given by

$$\frac{\partial u_i}{\partial x_i} = 0, \tag{2.1}$$

$$\frac{\partial u_i}{\partial t} + \frac{\partial}{\partial x_j}(u_i u_j) = -\frac{\partial p}{\partial x_i} + \nu \frac{\partial^2 u_i}{\partial x_j \partial x_j}, \tag{2.2}$$

where t is time, $x_i \equiv (x, y, z)$ denotes the coordinate axes, $u_i \equiv (u, v, w)$ denotes the velocity, p is the pressure and ν is the kinematic viscosity. Note that density has been absorbed into the pressure term. Eqs. 2.1 and 2.2 are the conservation laws for mass

and momentum respectively.

For simulations of marine propellers, it is convenient to use a rotating frame of reference which is attached to the propeller. The incompressible N–S equations in the rotating frame of reference can be formulated using either the absolute velocity or the relative velocity. Here, absolute velocity refers to the velocity vector with respect to the fixed frame and the relative velocity denotes the velocity vector defined in the rotating frame. Since, the pressure boundary condition can be more easily treated with the absolute velocity, the governing equations are written in the rotating frame of reference with the absolute velocity in this study. The incompressible N–S equations in the rotating frame can be formulated in a strongly conservative form [103] or in a form where system rotation produces a source term [104]. The governing equations used for propeller simulations in this study are as follow:

$$\frac{\partial u_i}{\partial x_i} = 0, \tag{2.3}$$

$$\frac{\partial u_i}{\partial t} + \frac{\partial}{\partial x_j}(u_i u_j - u_i \epsilon_{jkl} \omega_k x_l) = -\frac{\partial p}{\partial x_i} - \epsilon_{ijk} \omega_j u_k + \nu \frac{\partial^2 u_i}{\partial x_j \partial x_j} \tag{2.4}$$

where u_i is the inertial velocity in the inertial frame, p is the pressure, x_i are coordinates in the rotating non-inertial reference frame, ω_j is the angular velocity of the rotating frame of reference, ϵ_{ijk} denotes the permutation tensor. The terms containing ω_j in the Eq. 2.4 account for the effect of rotating reference frame. $\frac{\partial}{\partial x_j}(-u_i \epsilon_{jkl} \omega_k x_l)$ represents Coriolis acceleration whereas $-\epsilon_{ijk} \omega_j u_k$ is representative of centrifugal acceleration. Note that, only the momentum equation (Eq. 2.2) is modified by rotation, and substituting $\omega = 0$ in Eq. 2.4 recovers Eq. 2.2. In DNS, these equations are solved to fully resolve all the scales of turbulence down to the Kolmogorov scale.

2.2 Large eddy simulation

In LES, the large energy carrying scales of turbulence are directly resolved on the computational grid and the effect of the smaller scales is modeled. The flow variables

are decomposed into large scales (denoted by $\overline{(\cdot)}$) and small scales (denoted by $(\cdot)'$):

$$f(\mathbf{x},t) = \overline{f}(\mathbf{x},t) + f'(\mathbf{x},t). \tag{2.5}$$

This decomposition or scale separation is achieved by applying a low–pass spatial filter G to the flow variable f:

$$\overline{f}(\mathbf{x},\Delta,t) = G * f(\mathbf{x},t) = \int_D G(\mathbf{x},\mathbf{x}-\mathbf{r},\Delta) f(\mathbf{r},t) dr, \tag{2.6}$$

where Δ is the filter width and the integration is over the domain of computation.

Applying the filtering operation to the N–S equations yields the filtered N–S equations:

$$\begin{aligned} \frac{\partial \overline{u}_i}{\partial x_i} &= 0, \\ \frac{\partial \overline{u}_i}{\partial t} + \frac{\partial}{\partial x_j}(\overline{u}_i \overline{u}_j) &= -\frac{\partial \overline{p}}{\partial x_i} + \nu \frac{\partial^2 \overline{u}_i}{\partial x_j \partial x_j} - \frac{\partial \tau_{ij}}{\partial x_j}, \end{aligned} \tag{2.7}$$

where $\tau_{ij} = \overline{u_i u_j} - \overline{u}_i \overline{u}_j$ is the sub–filter scale (SFS) stress.

Similarly, the filtered N–S equations in the rotating frame of reference with the absolute velocity vector in the inertial frame are:

$$\begin{aligned} \frac{\partial \overline{u}_i}{\partial x_i} &= 0, \\ \frac{\partial \overline{u}_i}{\partial t} + \frac{\partial}{\partial x_j}(\overline{u}_i \overline{u}_j - \overline{u}_i \epsilon_{jkl} \omega_k x_l) &= -\frac{\partial \overline{p}}{\partial x_i} - \epsilon_{ijk} \omega_j \overline{u}_k + \nu \frac{\partial^2 \overline{u}_i}{\partial x_j \partial x_j} - \frac{\partial \tau_{ij}}{\partial x_j} \end{aligned} \tag{2.8}$$

where the approximation $\overline{u_i \epsilon_{jkl} \omega_k x_l} \approx \overline{u}_i \epsilon_{jkl} \omega_k x_l$ is used.

In general, the filtering and differentiation operators do not commute and there is a commutation error [105]. Note that in the absence of explicit filtering [106], the computational grid followed by the discretization operator constitutes the "filter" which is used to obtain the filtered N–S equations (Eqs. 2.7 and 2.8). Hence for grid–filtered LES, the SFS stress is equivalent to sub–grid scale (SGS) stress. This SGS stress τ_{ij} needs to be modeled to close these equations.

2.3 SGS stress model

It is generally accepted that small scales tend to be more universal and isotropic than large scales. Therefore, simple eddy viscosity SGS models are widely used in LES to model the resolved scale energy that would be transferred to the sub–grid scales if they were resolved. The Smagorinsky model [107] relates the anisotropic residual SGS stress to the filtered strain rate $\overline{S}_{ij}$ by an eddy viscosity ν_t

$$\tau_{ij} - \frac{1}{3}\tau_{kk}\delta_{ij} = -2\nu_t\overline{S}_{ij}. \tag{2.9}$$

The trace $\frac{1}{3}\tau_{kk}\delta_{ij}$ is absorbed in the pressure term. Analogous to the mixing–length hypothesis, the eddy viscosity is modeled as

$$\nu_t = l_s^2|\overline{S}| = -2(C_s\Delta)^2|\overline{S}|, \tag{2.10}$$

leading to the SGS stress model

$$\tau_{ij} - \frac{1}{3}\tau_{kk}\delta_{ij} = -2\nu_t\overline{S}_{ij} = -2(C_s\Delta)^2|\overline{S}|\overline{S}_{ij} \tag{2.11}$$

where C_s is a model coefficient and $|\overline{S}| = (2\overline{S}_{ij}\overline{S}_{ij})^{1/2}$.

In the standard Smagorinsky model, C_s is assumed to be a global adjustable parameter whose value is typically around 0.16. However, problems were encountered in applying a universal C_s to different flow regimes and in obtaining the appropriate behavior near walls.

The Dynamic Smagorinsky model (DSM) due to Germano et al. [1] removes this limitation by dynamically computing the model coefficient C_s from the resolved scales and allowing it to vary in space and time. DSM is based on the Germano identity

$$L_{ij} = T_{ij} - \widehat{\tau}_{ij} \tag{2.12}$$

where

$$L_{ij} = \widehat{\overline{u}_i\overline{u}_j} - \widehat{\overline{u}}_i\widehat{\overline{u}}_j, \qquad T_{ij} = \widehat{\overline{u_iu_j}} - \widehat{\overline{u}}_i\widehat{\overline{u}}_j \quad \text{and} \quad \widehat{\tau}_{ij} = \widehat{\overline{u_iu_j}} - \widehat{\overline{u}_i\overline{u}_j}. \tag{2.13}$$

Here, $\widehat{(\cdot)}$ denotes test filtering at scale $\widehat{\Delta}$ and is usually taken to be $\widehat{\Delta} = 2\Delta$. T_{ij} is analogous to τ_{ij} and is the corresponding SGS stress at the test filter scale. L_{ij} is the stress due to scales intermediate between Δ and 2Δ and can be computed directly from the resolved field. Similar to τ_{ij}, the deviatoric part (denoted by $()^d$) of T_{ij} is modeled using the Smagorinsky model at scale and $\widehat{\Delta}$ as

$$T_{ij} - \frac{1}{3}T_{kk}\delta_{ij} = -2(C_s\widehat{\Delta})^2|\widehat{\overline{S}}|\widehat{\overline{S}}_{ij}. \tag{2.14}$$

The dynamic procedure to obtain the SGS model coefficient C_s attempts to minimize the Germano-identity error (GIE),

$$\begin{aligned}\epsilon_{ij} &= T^d_{ij} - \widehat{\tau}^d_{ij} - L^d_{ij} \\ &= 2(C_s\Delta)^2\left[\widehat{|\overline{S}|\overline{S}}_{ij} - \left(\frac{\widehat{\Delta}}{\Delta}\right)^2|\widehat{\overline{S}}|\widehat{\overline{S}}_{ij}\right] - L^d_{ij} \\ &= (C_s\Delta)^2M_{ij} - L^d_{ij},\end{aligned} \tag{2.15}$$

where $M_{ij} = 2\left[\widehat{|\overline{S}|\overline{S}}_{ij} - \left(\frac{\widehat{\Delta}}{\Delta}\right)^2|\widehat{\overline{S}}|\widehat{\overline{S}}_{ij}\right]$.

Since $\epsilon_{ij}(C_s) = 0$ is a tensor equation, C_s is overdetermined. The standard DSM due to Germano et al. [1] satisfies $\epsilon_{ij}S_{ij} = 0$ to obtain C_s. Lilly [2] obtained C_s by minimizing ϵ_{ij} in a least-square sense. The cost function to be minimized can be expressed in the form

$$\mathcal{J} = \int_\Omega \epsilon_{ij}(\mathbf{x})\epsilon_{ij}(\mathbf{x})d\mathbf{x}, \tag{2.16}$$

where Ω is the averaging domain. This yields

$$(C_s\Delta)^2 = \frac{(L_{ij}M_{ij})_\Omega}{(M_{ij}M_{ij})_\Omega}, \tag{2.17}$$

where $(\cdot)_\Omega$ denotes averaging over Ω.

2.4 Lagrangian SGS model with dynamic Lagrangian time scale

In the absence of averaging, the local dynamic model (Eq. 2.17) is known to predict a highly variable eddy viscosity field. Also, the eddy viscosity can be negative, which can cause solutions to become unstable. C_s has a large auto-correlation time which causes negative eddy viscosity to persist for a long time, thereby causing a divergence of the total energy [108]. Hence averaging and/or clipping C_s (setting negative values of C_s to 0) was found to be necessary to stabilize the model. Positive C_s from Eq. 2.17 provides dissipation thereby ensuring the transfer of energy from the resolved to the subgrid scales. Germano et al. [1] suggested averaging over homogeneous directions for stability. Also, clipping is almost never required when averaging over homogeneous directions. Ghosal et al. [109] showed this averaging and/or clipping operation to be essentially a constrained minimization of Eq. 2.15.

However the requirement of averaging over at least one homogeneous direction is impractical for complex inhomogeneous flows. To enable averaging in inhomogeneous flows, Meneveau et al. [110] developed a Lagrangian version of DSM (LDSM) where C_s is averaged along fluid trajectories. Lagrangian averaging is physically appealing considering the Lagrangian nature of the turbulence energy cascade [111, 112]. Meneveau et al. [110] provide further justifications about the validity of averaging and the motivation for Lagrangian averaging.

In essence, the Lagrangian DSM attempts to minimize the pathline average of the local GIE squared [113, 114]. The objective function to be minimized is given by

$$E = \int_{pathline} \epsilon_{ij}(\mathbf{z})\epsilon_{ij}(\mathbf{z})d\mathbf{z} = \int_{-\infty}^{t} \epsilon_{ij}(\mathbf{z}(t'),t')\epsilon_{ij}(\mathbf{z}(t'),t')W(t-t')dt' \qquad (2.18)$$

where $\mathbf{z}$ is the trajectory of a fluid particle for earlier times $t' < t$ and W is a weighting function to control the relative importance of events near time t, with those at earlier times.

Choosing the time weighting function of the form $W(t-t') = T^{-1}e^{-(t-t')/T}$ yields

two transport equations for the Lagrangian average of the tensor products $L_{ij}M_{ij}$ and $M_{ij}M_{ij}$ as $\mathcal{I}_{LM}$ and $\mathcal{I}_{MM}$ respectively:

$$\begin{aligned} \frac{D\mathcal{I}_{LM}}{Dt} &\equiv \frac{\partial \mathcal{I}_{LM}}{\partial t} + \overline{u}_i \frac{\partial \mathcal{I}_{LM}}{\partial x_i} = \frac{1}{T}\big(L_{ij}M_{ij} - \mathcal{I}_{LM}\big) \quad \text{and} \\ \frac{D\mathcal{I}_{MM}}{Dt} &\equiv \frac{\partial \mathcal{I}_{MM}}{\partial t} + \overline{u}_i \frac{\partial \mathcal{I}_{MM}}{\partial x_i} = \frac{1}{T}\big(M_{ij}M_{ij} - \mathcal{I}_{MM}\big). \end{aligned} \tag{2.19}$$

whose solutions yield

$$(C_s\Delta)^2 = \frac{\mathcal{I}_{LM}}{\mathcal{I}_{MM}}. \tag{2.20}$$

Here T is a time scale which represents the 'memory' of the Lagrangian averaging. Meneveau et al. [110] proposed the following time scale:

$$T = \theta\Delta(\mathcal{I}_{LM}\mathcal{I}_{MM})^{(-1/8)}; \qquad \theta = 1.5. \tag{2.21}$$

This procedure for Lagrangian averaging has also been extended to the scale-similar model by Anderson and Meneveau [115] and Sarghini et al. [116] and the scale-dependent dynamic model by Stoll and Porté-Agel [117].

Verma and Mahesh [114] extended the dynamic Lagrangian averaging approach for the Dynamic Smagorinsky Model (DSM) for LES proposed by Park and Mahesh [113] to an unstructured grid framework and applied to inhomogeneous complex flows. Note that the time scale for Lagrangian averaging in Eq. 2.21 contains an adjustable parameter which is typically chosen to be $\theta = 1.5$. The Lagrangian time scale is dynamically computed from the solution and does not need any adjustable parameter. The dynamic time scale is computed based on a "surrogate-correlation" of GIE. Also, a simple material derivative relation is used to approximate GIE at different events along a pathline instead of Lagrangian tracking or multi-linear interpolation. The proposed model shows noticeable improvement when compared to other averaging procedures for DSM, especially at coarse resolutions. The model has been applied to LES of a variety of problems: channel flow, flow over a circular cylinder and propeller crashback, showing good agreement with past work [118].

2.5 Numerical discretization

Eq. 2.7 or 2.8 is solved by a numerical method developed by Mahesh et al. [3] for incompressible flows on unstructured grids. The algorithm discretely conserves not only a first order quantity - momentum, but also a second order quantity - kinetic energy, simultaneously. Discrete energy conservation ensures that the convective flux of kinetic energy, $\sum_{\text{cvs}} u_i \delta(u_i u_j)/\delta x_j$ has contributions only from the boundary faces. As a result, the algorithm is derived to be robust without numerical dissipation. The algorithm has been validated for a variety of problems over a range of Reynolds numbers [3]. The algorithm was used in the past to simulate a variety of complex flow problems, including jets [119–126], flow over hulls [7, 127, 128] and propellers in the crashback mode [93–99, 102].

The Harlow–Welch algorithm [129] is discretely kinetic energy conserving on staggered, structured grids. The numerical method developed by Mahesh et al. [3] is a finite volume method where the Cartesian velocities u_i and pressure p are stored at the centroids of the cells and the face–normal velocities v_n are stored independently at the centroids of the faces. Henceforth, all resolved flow variables will be denoted simply, without the overbar $\overline{()}$.

A predictor–corrector type, fractional–step method is used to solve Eq. 2.7. The non–linear convective term is denoted by NL and the viscous term incorporating the SGS stress term is denoted by $VISC$. Explicit time advancement is performed using the Adams–Bashforth scheme which is $O(\Delta t^2)$. The predicted velocities u_i^* at the control volume centroids are first obtained from the previous time steps k and $k-1$:

$$\frac{u_i^* - u_i^k}{\Delta t} = \frac{1}{2}\left[3(NL + VISC)^k - (NL + VISC)^{k-1}\right], \tag{2.22}$$

and then interpolated using symmetric averaging ($O(\Delta x^2)$) to obtain the predicted face–normal velocities:

$$v_n^* = \left(\frac{u_{i,icv1}^* + u_{i,icv2}^*}{2}\right) n_i, \tag{2.23}$$

where the face–normal $\vec{n}$ and hence v_n points from control volume $icv1$ to $icv2$.

The corrector step

$$\frac{u_i^{k+1} - u_i^*}{\Delta t} = -\frac{\partial p^{k+1}}{\partial x_i} \tag{2.24}$$

is projected onto the face–normal as:

$$\frac{v_n^{k+1} - v_n^*}{\Delta t} = -\frac{\partial p^{k+1}}{\partial n}. \tag{2.25}$$

The continuity equation imposes the constraint

$$\sum_{\text{faces of cv}} v_n^{k+1} A_f = 0, \tag{2.26}$$

where A_f is the face area. Substituting in eq. 2.25 yields a Poisson equation for p^{k+1}:

$$\begin{aligned} \sum_{\text{faces of cv}} v_n^{k+1} A_f - \sum_{\text{faces of cv}} v_n^* A_f &= -\Delta t \sum_{\text{faces of cv}} \frac{\partial p^{k+1}}{\partial n} A_f \\ \Rightarrow \Delta t \sum_{\text{faces of cv}} \frac{\partial p^{k+1}}{\partial n} A_f &= \sum_{\text{faces of cv}} v_n^* A_f, \end{aligned} \tag{2.27}$$

which is solved using the Algebraic Multi-Grid (AMG) method of *hypre* [130].
Once p^{k+1} is known, the pressure gradient $\frac{\partial p}{\partial x_i}$ is computed in a novel least squares formulation which minimizes the conservation error:

$$\sum_{\text{faces of cv}} \left(\frac{\partial p}{\partial x_i} n_i A_f - \frac{\partial p}{\partial n} A_f \right)^2. \tag{2.28}$$

Finally, corrected u_i and v_n are computed from Eqs. 2.24 and 2.25 using p^{k+1}.

Most of the simulations in this dissertation are performed with implicit time advancement using the Crank–Nicolson scheme which is $O(\Delta t^2)$:

$$\frac{u_i^* - u_i^k}{\Delta t} = \frac{1}{2} \left[(NL + VISC)^k + (NL + VISC)^{k+1} \right]. \tag{2.29}$$

$(NL + VISC)^{k+1}$ contains u_i^{k+1} which is expressed in terms of u_i^k as

$$u_i^{k+1} = u_i^* - \Delta t \frac{\partial p^{k+1}}{\partial x_i}, \tag{2.30}$$

where p^{k+1} is linearized as $p^{k+1} = p^k + O(\Delta t)$. Eq. 2.29 reduces to a system of linear equations which is solved for u_i^* using SOR.

Note that typically, the face–normal derivatives at a face are computed using

$$\frac{\partial(\cdot)}{\partial n}\Big|_f = \frac{(\cdot)_{nbr} - (\cdot)_{icv}}{d_f}, \tag{2.31}$$

where nbr denotes the neighboring control volume of icv and $d_f = (x_{i,nbr} - x_{i,icv})n_{i,f}$ is the face–normal distance.

2.6 Turbulent inflow generation

Unlike channel or pipe flow, in spatially evolving boundary layers the boundary layer thickness and the wall shear stress is a function of streamwise distance which makes the flow inhomogeneous in the streamwise direction. The methodology for DNS of a spatially developing turbulent boundary layer was pioneered by Spalart [131]. He used a set of coordinate transformations to minimize the streamwise inhomogeneity so that the periodic boundary conditions in that direction can still be used. However, this method introduces additional terms in the N–S equations. Lund et al. [4] modified the Spalart method to make it simpler and easy to implement. Instead of using growth terms, they proposed the so-called recycle-rescale method where the flow field at a streamwise location downstream is rescaled and re-introduced at the inflow. Thus, the simulation generates its own inflow. The algorithm has been shown to avoid the long development region needed to generate a developed boundary layer, from a parallel flow with random fluctuations. The basic idea behind the recycle-rescale method is that the mean velocity profile in zero-pressure-gradient turbulent boundary layer becomes self-similar. The details of the inflow generation are briefly described as follows.

The velocities at the inflow plane, $x = x_{in}$ are written as:

$$\begin{aligned} u(y,z,t) &= \beta[\gamma\bar{U}(x_r,y_r^o,t) + (1-\gamma)U_\infty + \gamma u'(x_r,y_r^o,z_r,t)] \\ &+ (1-\beta)[\gamma\bar{U}(x_r,y_r^i,t) + \gamma u'(x_r,y_r^i,z_r,t)], \qquad (2.32) \\ v(y,z,t) &= \beta[\bar{V}(x_r,y_r^o,t) + \gamma v'(x_r,y_r^o,z,t)] \\ &+ (1-\beta)[\bar{V}(x_r,y_r^i,t) + \gamma v'(x_r,y_r^i,z,t)] \qquad (2.33) \\ w(y,z,t) &= \beta\gamma w'(x_r,y_r^o,z,t) + (1-\beta)\gamma w'(x_r,y_r^i,z,t) \qquad (2.34) \end{aligned}$$

where the $\bar{(\cdot)}$ is the spanwise average through time, 'r' denotes the recycle plane, 'i' denotes the inner scale, 'o' denotes the outer scale. The inner and outer scales are based on $y^+ = yu_\tau/\nu$ and $\eta = y/\delta$ respectively.

$$\beta(\eta) = \frac{1}{2}\left\{1 + \frac{tanh\left(\frac{a(\eta-b)}{(1-2b)\eta+b}\right)}{tanh(a)}\right\} \qquad (2.35)$$

is a weighting function which is used to blend the inner and outer scales. Here, $a = 4$ and $b = 0.2$.

The mean velocity profile is obtained by spanwise averaging at every time step and then averaging over a sliding time window (T). The averaging time window is initially set to $T = A\delta_{99,i}/U_\infty$ where $A = 10$ to discard the transients and then switched to 100 once the transients die out. The running average,

$$\mathcal{F}(t) = \left(1 - \frac{\Delta t}{T}\right)\mathcal{F}(t-\Delta t) + \frac{\Delta t}{T}f(t) \qquad (2.36)$$

where f is the instantaneous spanwise average. Finally, the averaging is switched to a simple running average with $T = T_0 + t - t_0$ where, t is the time in the simulation, t_0 is the time at which the running averaging was initiated and T_0 is the value of the averaging interval used prior to t_0. This mean boundary layer velocity profile is used to evaluate the scaling parameters $(\theta, \delta_{99}, u_\tau)$ as a function of streamwise location.

In order to generate the desired turbulent inflow, the inflow parameters $u_{\tau,i}$, θ_i and

$\delta_{99,i}$ are specified. The value of θ_i is kept fixed whereas $u_{\tau,i}$ is computed at every time step using Eq. 2.37, knowing the values of flow parameters at the rescale plane.

$$u_{\tau,i} = u_{\tau,r}\left(\frac{\theta_r}{\theta_i}\right)^{(1/8)}, \tag{2.37}$$

The rescale parameter γ is defined as:

$$\gamma = \frac{u_{\tau,i}}{u_{\tau,r}} = \left(\frac{\theta_r}{\theta_i}\right)^{(1/8)} \tag{2.38}$$

which is used to construct velocities at the inflow plane. The constructed inflow plane velocity profiles are adjusted through a Newton–Raphson scheme to obtain $\delta_{99,i}$.

First, the recycle-rescale method is implemented for unstructured grids and massively parallel platforms and extensively validated for a range of Re_θ. Recall that axisymmetric boundary layers have an additional length parameter (δ/a) to take into account the curvature effects. Our problem of interest (hull boundary layer) has thin axisymmetric TBL at high Re i.e. small δ/a and large a^+. In this flow regime, the recycle-rescale method of Lund et al. [4] can be extended to spatially developing axisymmetric TBL with some modifications [100]. The validation cases for both planar and axisymmetric TBL are described in rest of this chapter.

2.6.1 Planar turbulent boundary layers

Simulations are performed for spatially developing planar boundary layers for two inflow Reynolds number, $Re_{\theta,in} = 1410$ and 2200. The computational domain used for the simulations is a box of length L_x, width L_z and height L_y as shown in Figure 2.1. The subscripts x, y and z refer to streamwise, wall-normal and spanwise directions respectively. Flow is from left to right and the wall is located at $y = 0$. No-slip boundary conditions are applied on the wall and convective boundary conditions are prescribed at the outflow. The boundary conditions on the top surface ($y = L_y$) are:

$$\frac{\partial u}{\partial y} = 0, \quad v = U_e\frac{\partial \delta^*}{\partial x}, \quad \frac{\partial w}{\partial y} = 0 \tag{2.39}$$

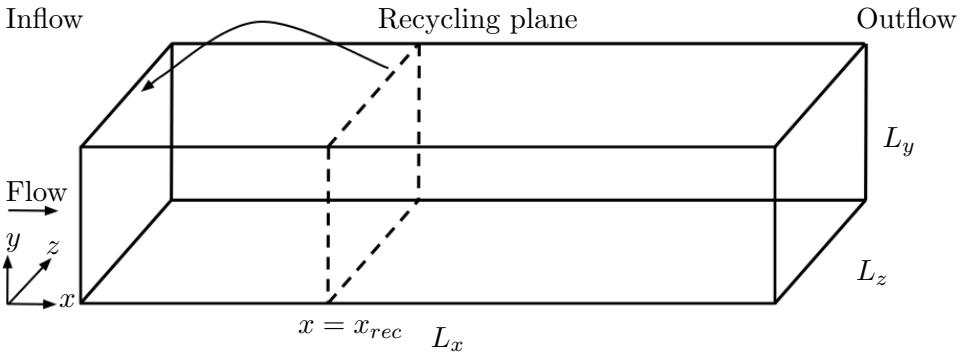

Figure 2.1: A schematic of the computational domain used for simulations of planar TBL. The velocities at recycling plane ($x = x_{rec}$) are rescaled and prescribed at the inflow plane at each time step to generate turbulent inflow.

Case	$Re_{\theta,in}$	L_x/θ_{in}	L_y/θ_{in}	L_z/θ_{in}	N_x	N_y	N_z	x_{rec}/θ_{in}
S1410	1410	300	30	20	1000	200	200	82.5
S2200	2200	300	30	20	1000	200	200	247.5

Table 2.1: Details of domain size and grid distribution for planar TBL simulations.

where δ^* is the boundary layer displacement thickness, $\frac{\partial \delta^*}{\partial x}$ is the boundary layer growth parameter, and U_e is the edge velocity. Note that at every time step, δ^* is obtained from the mean (spanwise and temporally averaged) velocity field as a function of x and then $\frac{\partial \delta^*}{\partial x}$ is computed as an average slope, whose value is usually small.

The details of planar TBL simulations are listed in Table 2.1. The θ_{in} is fixed at 0.1 and the computational grid is identical for both cases. The location of the recycling plane has to be sufficiently far away from the inflow and outflow to avoid any unphysical behavior. The computational grid is uniform in x and z direction with clustering near the wall in y direction to resolve fine near-wall flow structures. Once the simulations reach statistical stationary state, mean and second-order statistics are computed using snapshots of the instantaneous flow field collected over non-dimensional time $T^+ = tu_\tau^2/\nu = 20000$ with a sampling resolution of $\Delta t^+ = 10$ for both cases.

The mean and second-order velocity statistics for Case S1410 are compared to past

Case	x	Re_θ	Δx^+	Δy^+_{min}	Δz^+
S1410	0.255	1420	18.6	0.31	6.2
S1410	5.085	1551	18.5	0.31	6.17
S1410	20.985	1968	17.8	0.3	5.95
S2200	8.925	2540	18.8	0.45	8.93
S2200	21.765	3032	26.4	0.44	8.8

Table 2.2: Details of grid resolution at different streamwise locations for planar TBL simulations.

DNS results [132, 133] in Figure 2.2 at three streamwise locations, details of which are listed in Table 2.2. The profiles are in excellent agreement with the DNS results at $Re_\theta = 1420$, $Re_\theta = 1551$ and $Re_\theta = 1968$. The streamwise evolution of boundary layer thicknesses and Re_θ are shown for Case S1410 in Figure 2.3. The streamwise growth is nearly linear throughout the domain. The shape factor, H and edge velocity in wall units, U_0^+ are plotted against Re_θ and compared to the correlations of Monkewitz et al. [134] in Figure 2.4. The edge velocity in wall units is related to skin-friction, C_f as $U_0^+ = \sqrt{2/C_f}$. The results show very good agreement with the asymptotic correlations for both H and U_0^+.

The mean second-order velocity statistics for Case S2200 are compared to past DNS results [132, 133] in Figure 2.5 at two streamwise locations (Table 2.2). The profiles are in excellent agreement with the DNS results at at $Re_\theta = 2540$ and $Re_\theta = 3032$ [132]. The streamwise evolution of boundary layer thicknesses and Re_θ (Figure 2.6) show trends similar to Case S1410. The evolution of H and U_0^+ (Figure 2.7) are in very good agreement with the asymptotic correlations of Monkewitz et al. [134].

Note that a small region near the inflow shows a slight mismatch between the present results and the correlations in the plots of H and U_0^+ (Figures 2.4 and 2.7). Such behavior is inherent in the recycle-rescale methodology and not due to flow solver or the grid resolution [135].

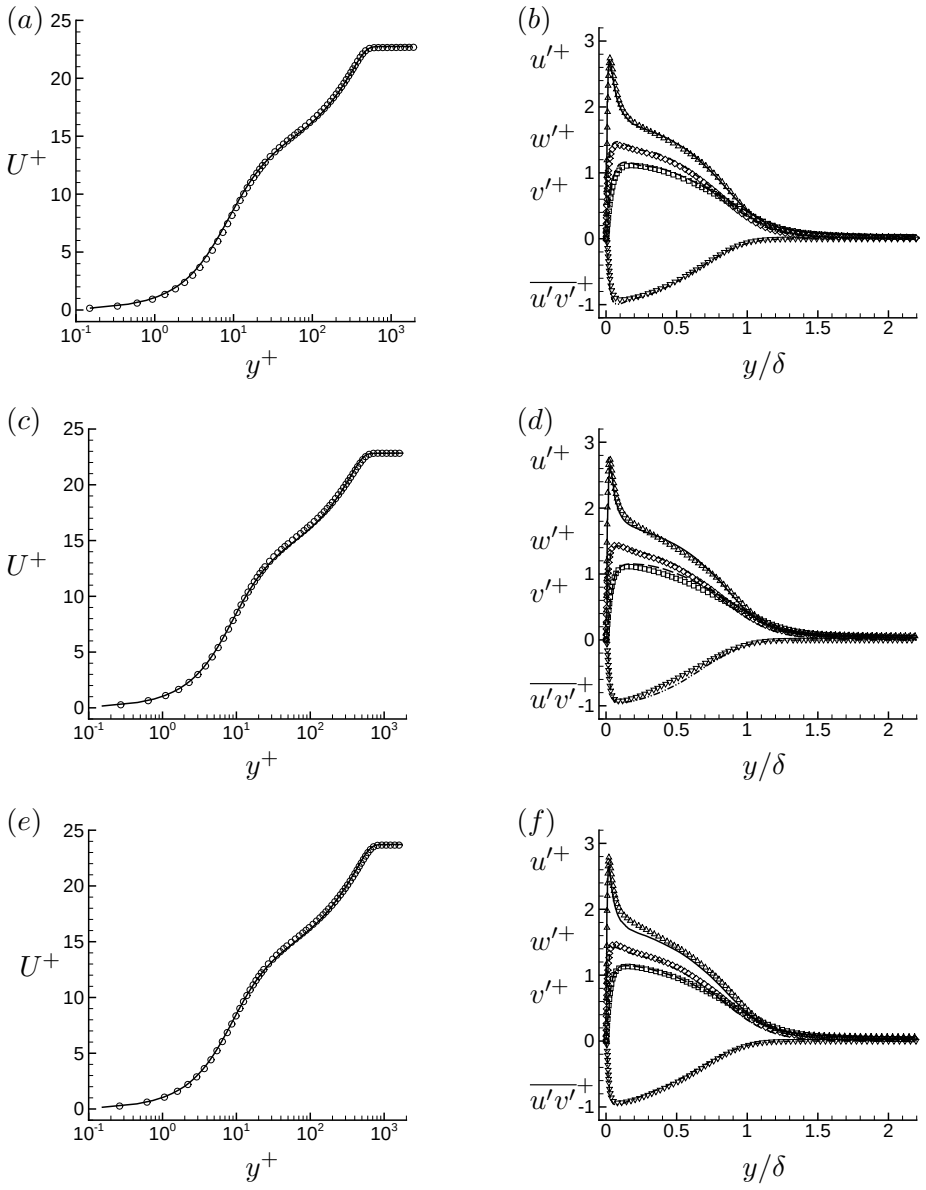

Figure 2.2: Case S1410: mean and second-order velocity statistics at $Re_\theta = 1420$ (a,b), 1551 (c,d) and 1968 (e,f) compared to the DNS of Schlatter and Örlü [132] (a,b) and Jiménez et al. [133] (c-f).

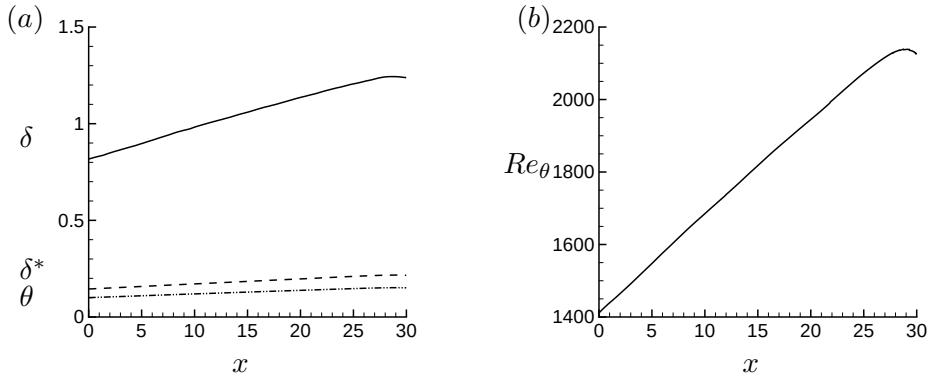

Figure 2.3: Case S1410: spatial evolution of boundary layer thicknesses (a) and Re_θ (b).

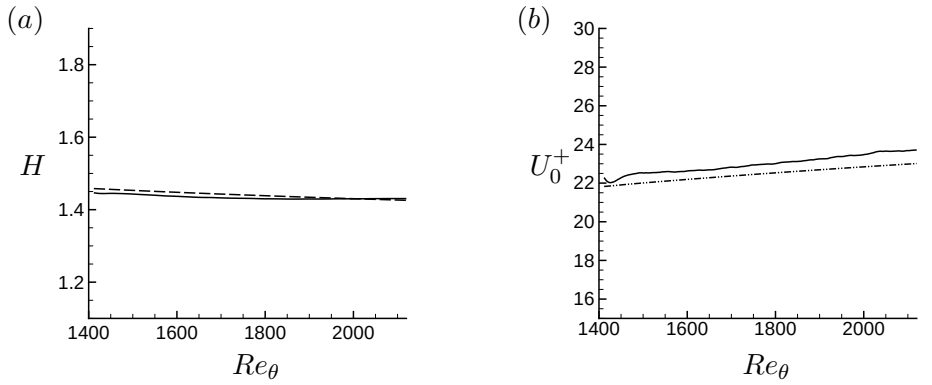

Figure 2.4: Case S1410: spatial evolution of boundary layer H (a) and U_0^+ (b) compared to the correlations of Monkewitz et al. [134].

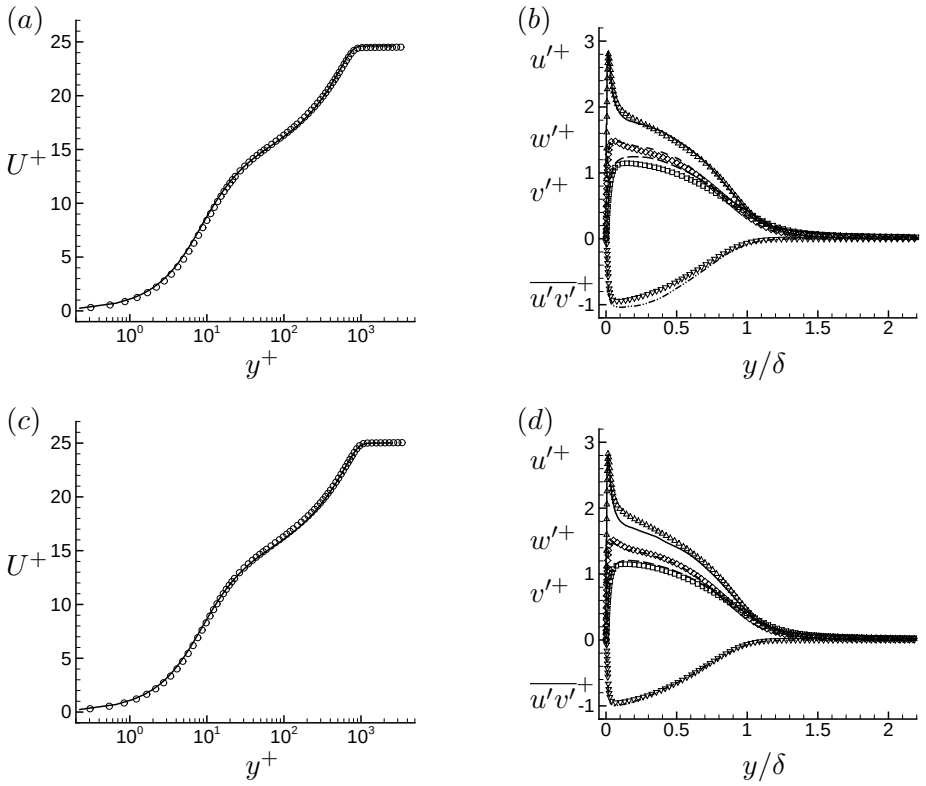

Figure 2.5: Case S2200: mean and second-order velocity statistics at $Re_\theta = 2540$ (a,b) and 3032 (c,d) compared to the DNS of Schlatter and Örlü [132].

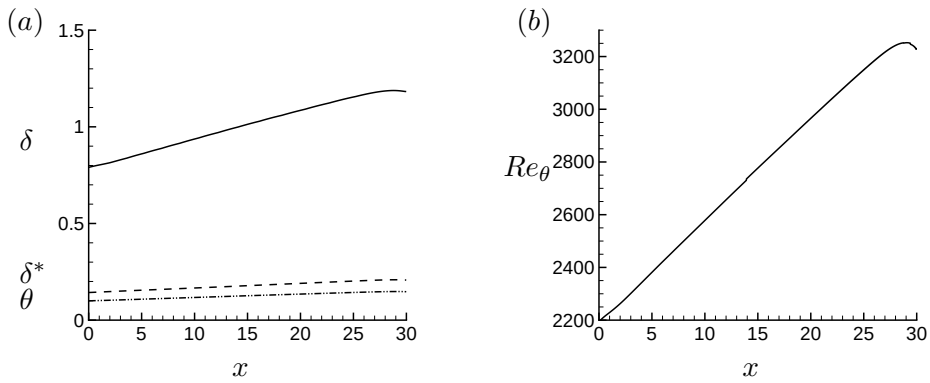

Figure 2.6: Case S2200: spatial evolution of boundary layer thicknesses (a) and Re_θ (b).

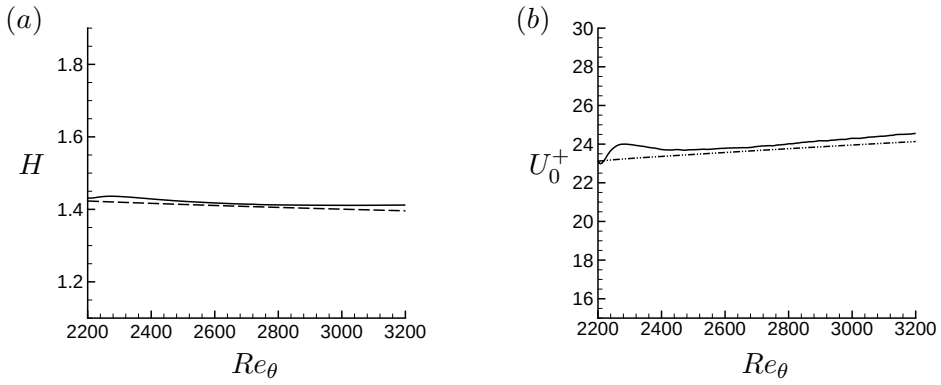

Figure 2.7: Case S2200: spatial evolution of boundary layer H (a) and U_0^+ (b) compared to the correlations of Monkewitz et al. [134].

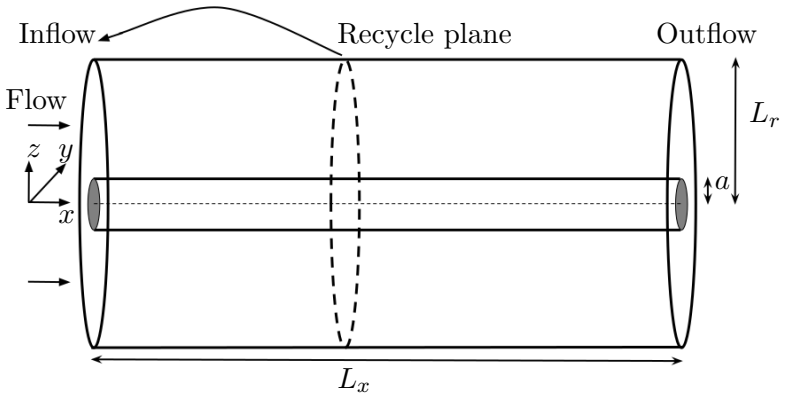

Figure 2.8: A schematic of the computational domain used for simulations of axisymmetric TBL. The velocities at recycling plane ($x = x_{rec}$) are rescaled and prescribed at the inflow plane at each time step to generate turbulent inflow.

Case	$Re_{\theta,in}$	θ_{in}/a	Re_a	L_x/a	L_r/a	N_x	N_r	N_ϕ	x_{rec}/θ_{in}
S356	356	0.017	20800	10	2	300	100	200	485.3
S1500	1500	0.07	20825	10	4.8	1000	200	200	137.5

Table 2.3: Details of domain size and grid distribution for axisymmetric TBL simulations.

2.6.2 Axisymmetric turbulent boundary layers

Simulations are performed for spatially developing axisymmetric TBL for two inflow Reynolds number, $Re_{\theta,in} = 356$ and 1500. The computational domain is an annular region between two cylinders of length L_x. The outer cylinder has a radius L_r whereas the inner cylinder has a radius a, as shown in Figure 2.8. The details of axisymmetric TBL simulations are listed in Table 2.3. The parameters for Case S356 are chosen to match a DNS by Woods [136] and that of Case S1500 are chosen to be representative of flow conditions on hull at $Re = 1.1 \times 10^6$, based on freestream velocity and hull length. The range of Re_θ and grid resolutions for these two simulations are listed in Table 2.4. The subscripts x, r and ϕ refer to streamwise, wall-normal and azimuthal directions respectively. The grid is uniform in x and (ϕ) with a gentle growth in r away from the wall. Flow is from left to right and the wall is located at $r = a$. The boundary conditions on the outer cylindrical surface are :

$$\frac{\partial u}{\partial r} = 0, \quad u_r = U_e \frac{\partial \delta^*}{\partial x}, \quad \frac{\partial u_\phi}{\partial r} = 0 \tag{2.40}$$

where u, u_r and u_ϕ are axial, radial and azimuthal velocity respectively and δ^* is obtained from mean (azimuthal and time averaged) velocity field in cylindrical components. The boundary layer growth parameter is obtained from δ^* similar to planar TBL simulations.

The instantaneous axial velocity in xy plane for Case S356 is shown in Figure 2.9. The instantaneous axial velocity and azimuthal vorticity in the yz plane at $x = 5a$ are shown in Figure 2.10. The mean axial velocity profile is compared to the DNS of Woods [136], showing good agreement. A small mismatch in the buffer layer can be due to the

Case	Re_θ	Δx^+	Δr^+_{min}	$a^+\Delta\phi$
S356	356-700	37.5	0.14	35.3
S1500	1500-2300	33.7	0.1	29.4

Table 2.4: Details of grid resolution for axisymmetric TBL simulations, computed using u_τ at the mid of the computational domain.

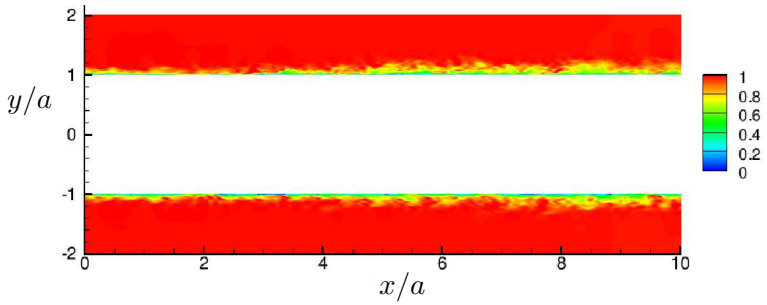

Figure 2.9: Case S356: instantaneous axial velocity in xy plane.

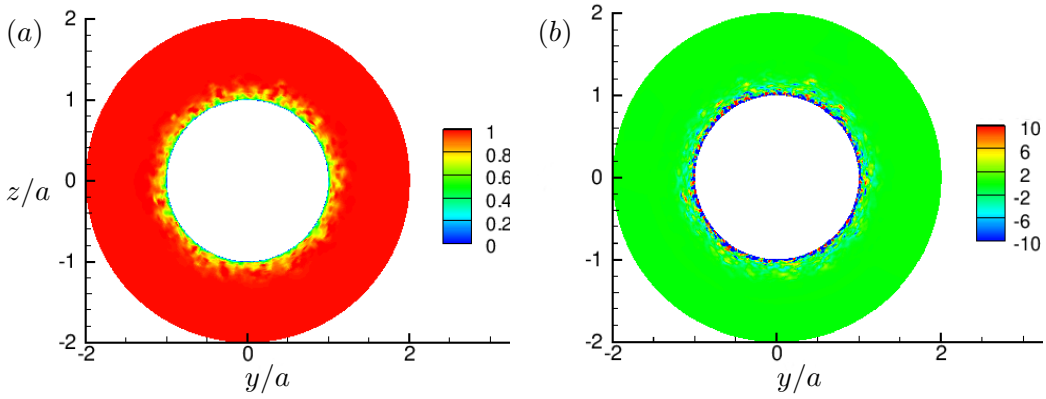

Figure 2.10: Case S356: Instantaneous axial velocity (a) and azimuthal vorticity (b) in the yz plane at $x = 5a$.

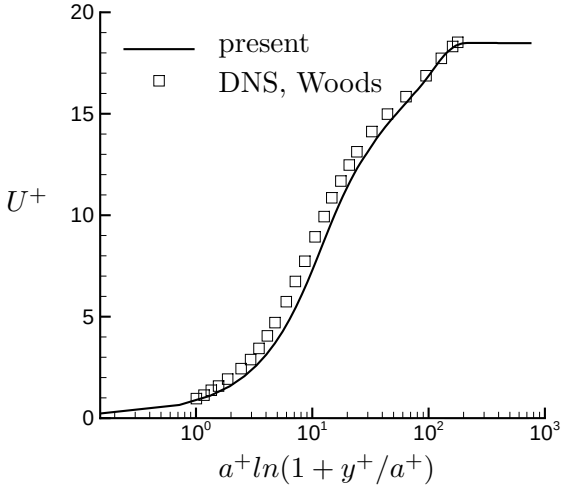

Figure 2.11: Case S356: mean axial velocity compared to the DNS data of Woods [136].

fact that the comparison is made very close to the inflow. The streamwise evolution of Re_θ is shown for Case S356 in Figure 2.12(a). The evolution of H and U_0^+ are compared to the planar [134] and axisymmetric [33, 136, 137] TBL correlations available in the literature in Figures 2.12(b,c). Away from the inflow, the axial evolution of H and U_0^+ show similar slope as compared to the correlations. The computed H is higher than the predicted value for axisymmetric TBL [33] but lower than that of planar TBL [134]. Note that the correlation given by Jordan [33] is based on a simulation database for thick axisymmetric TBL ($\delta/a > 1$) at high Re. The computed value of U_0^+ is lower than the predicted values for planar TBL [134], similar to the trend shown by H. However, the computed values are higher than the predictions of Woods [136] but lower than that of Monte et al. [137]. Note that Monte et al. [137] improved the correlation given by [136] with their simulation database, which showed better match with the experimental data and both [136] and [137] used simulations of thick axisymmetric TBL ($\delta/a > 1$) for curve-fitting to obtain these correlations. Recall that the recycle-rescale method assumes self-similarity of TBL, which is valid at high Re_θ. The Re_θ of Case S356 is small. The C_f values for axisymmetric boundary layers are known to be higher than

planar boundary layers at comparable Re_θ [10]. This explains the trend shown by U_0^+.

Figure 2.13 shows instantaneous axial velocity in xy plane for Case S1500. The instantaneous axial velocity and azimuthal vorticity in the yz plane at $x = 18a$ are shown in Figure 2.14. The mean axial velocity profile is compared to the DNS for planar TBL at same Re_θ [133] in Figure 2.15. The results show that axisymmetric TBL has higher skin-friction than its planar counterpart at similar conditions, consistent with past observations [10]. The evolution of boundary layer quantities (Re_θ, H and U_0^+) are shown in Figure 2.16. H and U_0^+ show trends similar to Case S356 when compared to the correlations available in the literature. However, the transient region close to the inflow is smaller compared to Case S356, clearly seen in the plot of H. This supports the argument that the larger transient region near inflow in Case S356 is due to lower Re_θ.

The recycle-rescale method presented in this section will be used to study the flow over the stern of a hull and the resulting wake in Chapter 5.

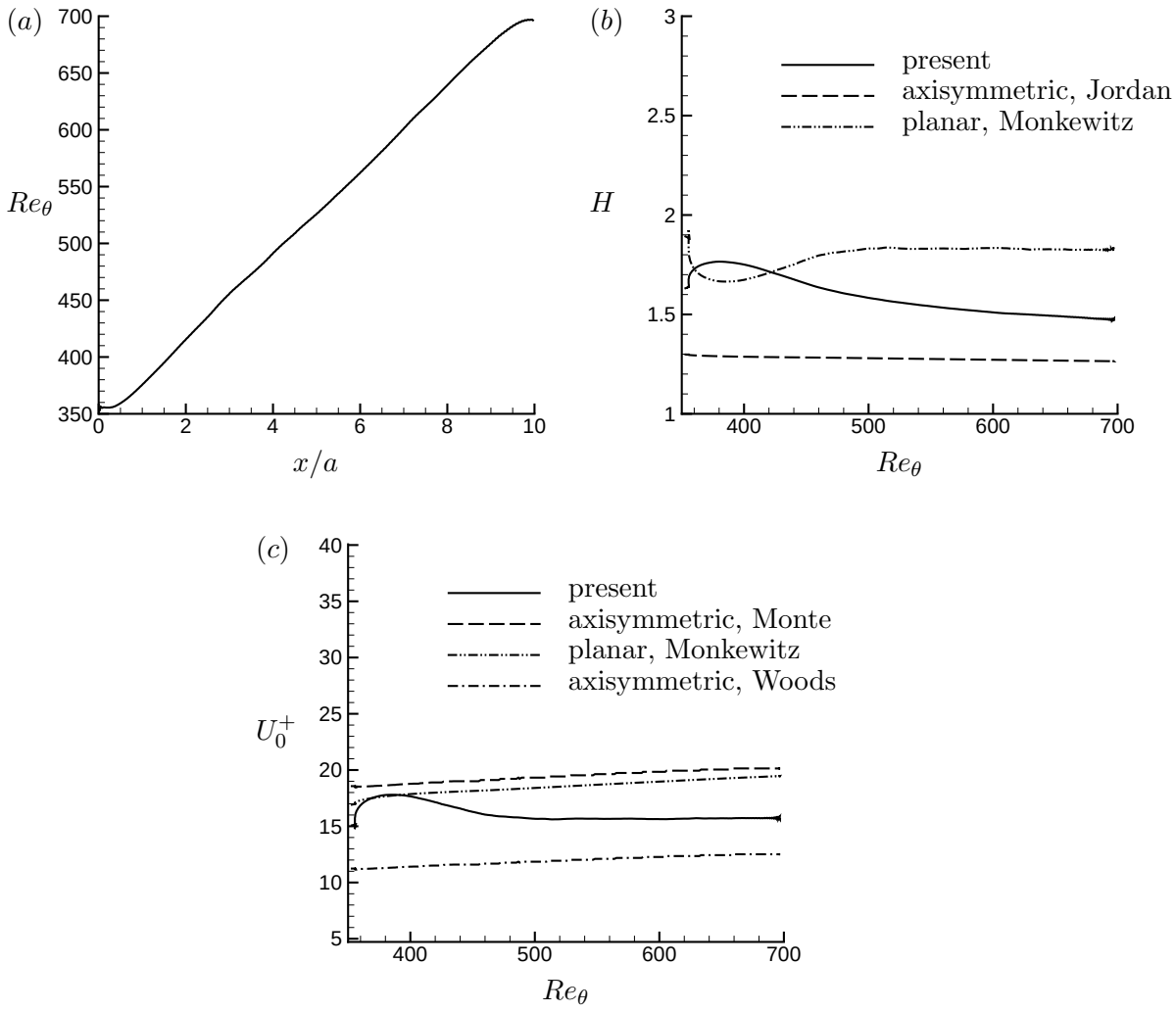

Figure 2.12: Case S356: spatial evolution of axisymmetric TBL Re_θ (a), H (b) and U_0^+ (c). The correlations for planar [134] and axisymmetric [136, 137] TBL are also shown for H (b) and U_0^+ (c) for comparison.

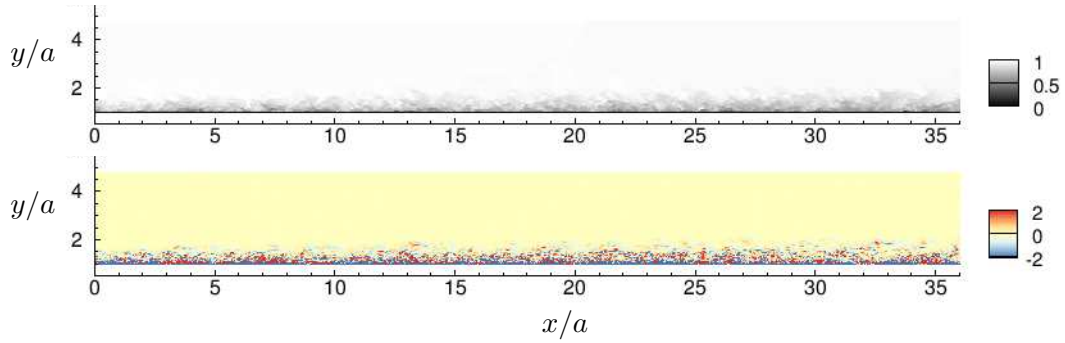

Figure 2.13: Case S1500: instantaneous axial velocity (a) and azimuthal vorticity (b) in xy plane.

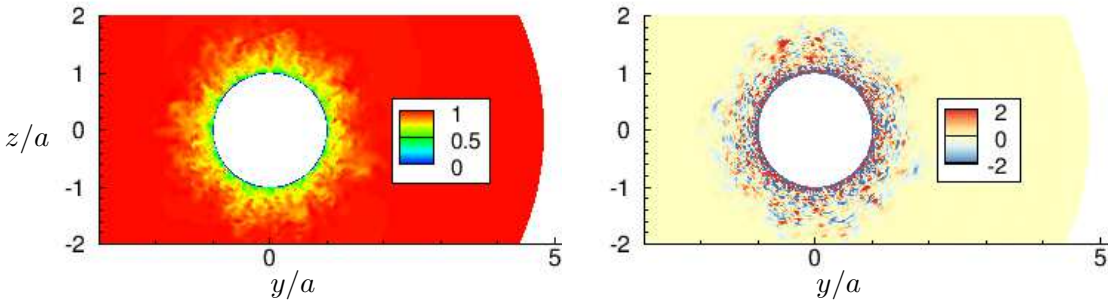

Figure 2.14: Case S1500: instantaneous axial velocity (a) and azimuthal vorticity (b) in the yz plane at $x/a = 18$.

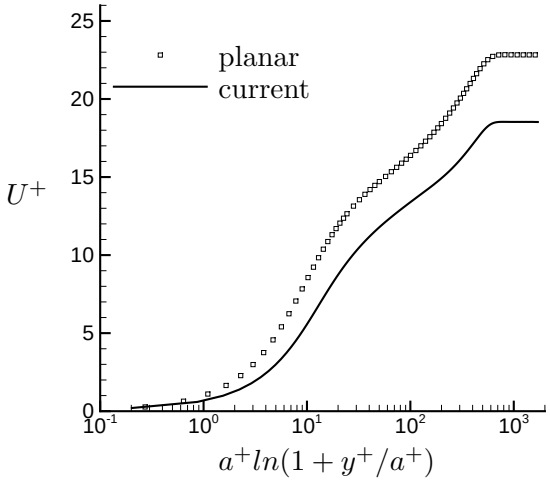

Figure 2.15: Case S1500: mean axial velocity compared to planar TBL at identical $Re_\theta = 1551$ [133].

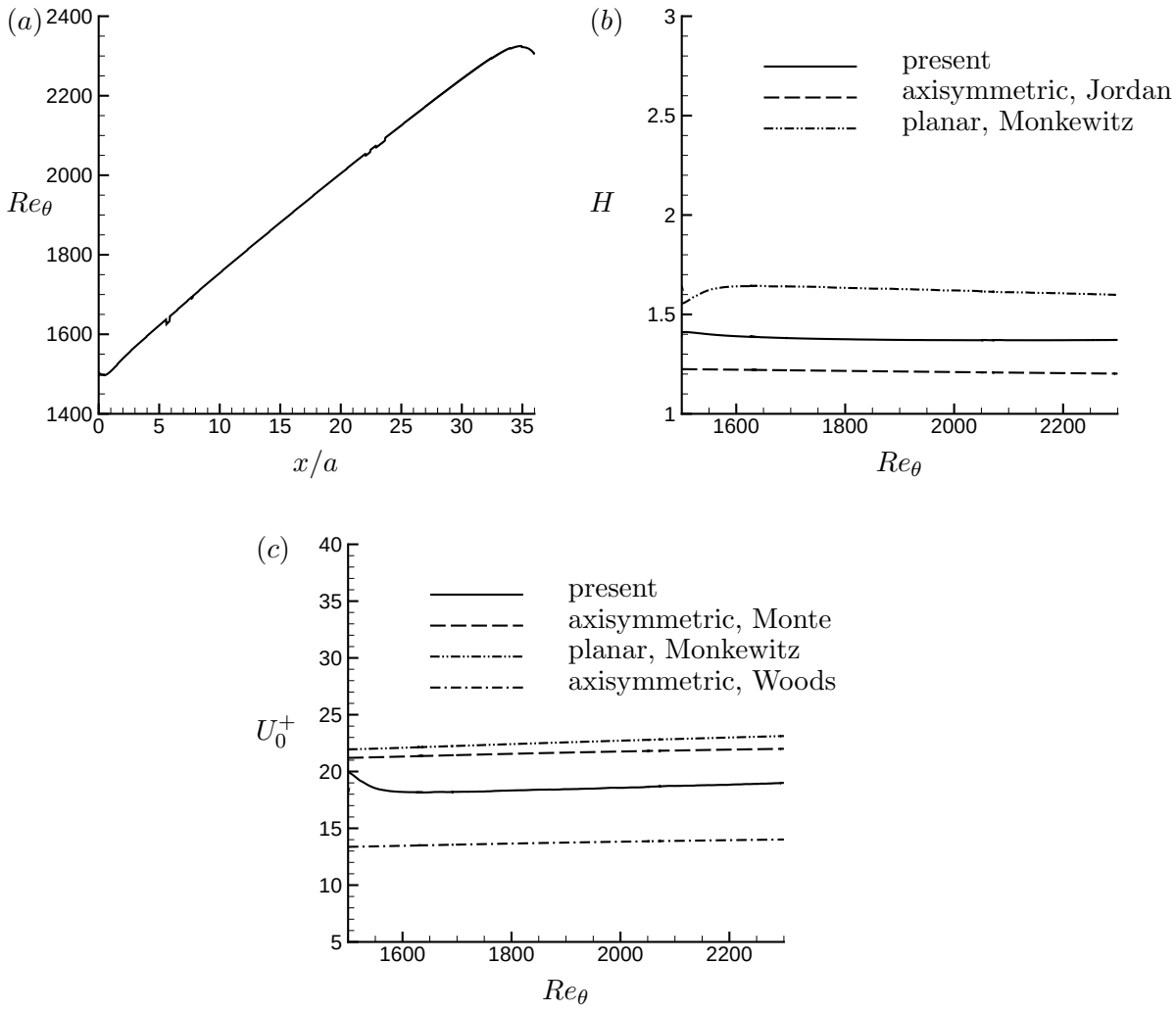

Figure 2.16: Case S1500: spatial evolution of Re_θ (a), H (b) and U_0^+ (c). The correlations for planar [134] and axisymmetric [136, 137] TBL are also shown for H (b) and U_0^+ (b) for comparison.

Chapter 3

Analysis of axisymmetric boundary layers

In this chapter, the governing equations of axisymmetric boundary layers evolving under the influence of pressure gradients are analyzed to understand the effect of transverse curvature on the flow. Integral analysis of the governing equations is performed in Section 3.1 and the obtained relations are compared to the existing data in Section 3.2. Implications of the analytical relations are discussed in Section 3.3. Section 3.4 summarizes the chapter.

3.1 Integral analysis of axisymmetric boundary layer

The boundary layer approximations for the N–S equations in cylindrical coordinates give,

$$r\frac{\partial U}{\partial x} + \frac{\partial (rV)}{\partial r} = 0, \tag{3.1}$$

$$rU\frac{\partial U}{\partial x} + rV\frac{\partial U}{\partial r} = -\frac{r}{\rho}\frac{dp}{dx} + \frac{\partial (r\nu\frac{\partial U}{\partial r})}{\partial r} + \frac{\partial (-r\overline{u'v'})}{\partial r} \tag{3.2}$$

where u' and v' are fluctuations in axial and radial velocities. Note that the stress term involving $\partial(\overline{u'u'} - \overline{v'v'})/\partial x$ has been ignored on the right hand side of Eq. 3.2 for

the present analysis. This term however, can not be neglected for large magnitude of pressure gradients and boundary layers on the verge of separation. We have not made any assumption on the nature of boundary layer i.e. it can be laminar, transitional or turbulent. This implies that the present analysis holds as long as the governing equations (Eqs. 3.1, 3.2) are valid.

For boundary layers under pressure gradient, the mean wall-normal velocity (V_a) is not constant outside the boundary layer. Hence, the boundary layer equations are integrated in the wall-normal direction from the surface, $r = a$ to a location outside the boundary layer, $r = a + k\delta$ where a is the radius of curvature (cylinder), $k \geq 1$ is a parameter and δ is the boundary layer thickness. Note that setting $k = 1$ makes $V_a = V_e$, which is the mean wall-normal velocity at the edge of the boundary layer. Integration of Eqs. 3.1 and 3.2 with the aforementioned limits yield,

$$\begin{aligned} \int_a^{a+k\delta} r\frac{\partial U}{\partial x}dr &= -\int_a^{a+k\delta}\frac{\partial(rV)}{\partial r}dr = -\Big(rV\Big)\Big|_a^{a+k\delta} \\ &= -(a+k\delta)V_a, \end{aligned} \tag{3.3}$$

$$\begin{aligned} \int_a^{a+k\delta} rU\frac{\partial U}{\partial x}dr + \int_a^{a+k\delta} rV\frac{\partial U}{\partial r}dr &= -\int_a^{a+k\delta}\frac{r}{\rho}\frac{dp}{dx} + \int_a^{a+k\delta}\frac{\partial(r\nu\frac{\partial U}{\partial r})}{\partial r}dr + \int_a^{a+k\delta}\frac{\partial(-r\overline{u'v'})}{\partial r}dr \\ &= -\beta_{RC}\frac{u_\tau^2}{2\delta^*}r^2\Big|_a^{a+k\delta} + (r\nu\frac{\partial U}{\partial r})\Big|_a^{a+k\delta} - (r\overline{u'v'})\Big|_a^{a+k\delta} \end{aligned} \tag{3.4}$$

where, β_{RC} is defined as,

$$\beta_{RC} = \frac{\delta^*}{u_\tau^2}\frac{1}{\rho}\frac{dp}{dx} = -\frac{\delta^*}{u_\tau^2}U_e\frac{dU_e}{dx} \tag{3.5}$$

and $f\Big|_a^b = f(b) - f(a)$.

Using the boundary conditions,

$$U\Big|_a = 0, \quad U\Big|_{a+k\delta} = U_e, \tag{3.6}$$

$$V\Big|_a = 0, \quad V\Big|_{a+k\delta} = V_a, \tag{3.7}$$

$$\frac{\partial U}{\partial r}\Big|_a = u_\tau^2/\nu, \quad \frac{\partial U}{\partial r}\Big|_{a+k\delta} = 0, \tag{3.8}$$

$$(-\overline{u'v'})\Big|_a = (-\overline{u'v'})\Big|_{a+k\delta} = 0, \tag{3.9}$$

the right hand side of Eq. 3.4 can be evaluated. This gives,

$$\begin{aligned}
&\int_a^{a+k\delta} rU\frac{\partial U}{\partial x}dr + \int_a^{a+k\delta} rV\frac{\partial U}{\partial r}dr = -\beta_{RC}\frac{u_\tau^2}{2\delta^*}r^2\Big|_a^{a+k\delta} - au_\tau^2 \\
\implies &\int_a^{a+k\delta} rU\frac{\partial U}{\partial x}dr + (rVU)\Big|_a^{a+k\delta} - \int_a^{a+k\delta} U\frac{\partial (rV)}{\partial r}dr = -\beta_{RC}\frac{u_\tau^2}{2\delta^*}r^2\Big|_a^{a+k\delta} - au_\tau^2 \\
\implies &\int_a^{a+k\delta} rU\frac{\partial U}{\partial x}dr + (a+k\delta)V_aU_e + \int_a^{a+k\delta} rU\frac{\partial U}{\partial x}dr = -\beta_{RC}\frac{u_\tau^2}{2\delta^*}r^2\Big|_a^{a+k\delta} - au_\tau^2 \\
\implies &\int_a^{a+k\delta} r\frac{\partial U^2}{\partial x}dr = -(a+k\delta)V_aU_e - \beta_{RC}\frac{u_\tau^2}{2\delta^*}r^2\Big|_a^{a+k\delta} - au_\tau^2.
\end{aligned} \tag{3.10}$$

The shape factor, H is defined as,

$$H = \frac{\delta^*}{\theta}. \tag{3.11}$$

Differentiating both sides with respect to x,

$$\frac{dH}{dx} = \frac{1}{\theta}\frac{d\delta^*}{dx} - \frac{\delta^*}{\theta^2}\frac{d\theta}{dx} \tag{3.12}$$

$$\implies \theta\frac{dH}{dx} = \frac{d\delta^*}{dx} - H\frac{d\theta}{dx} \tag{3.13}$$

$$\implies H = \frac{\frac{d\delta^*}{dx}}{\frac{d\theta}{dx}} - \theta\frac{\frac{dH}{dx}}{\frac{d\theta}{dx}}. \tag{3.14}$$

Note that no assumption has been made regarding the self-similarity of the boundary

layer as yet. The second term in the right hand side of Eq. 3.14 is small as H varies very slowly with x as compared to δ^* and hence, can be neglected. Self-similarity implies $\frac{dH}{dx} = 0$, which makes the second term identically zero. Therefore,

$$H = \left(\frac{d\delta^*}{dx}\right) \Big/ \left(\frac{d\theta}{dx}\right) \tag{3.15}$$

δ^* and θ for axisymmetric boundary layers are defined [26] such that,

$$(\delta^* + a)^2 - a^2 = 2\int_a^{a+\delta} \left(1 - \frac{U}{U_e}\right) r dr, \tag{3.16}$$

$$(\theta + a)^2 - a^2 = 2\int_a^{a+\delta} \frac{U}{U_e}\left(1 - \frac{U}{U_e}\right) r dr. \tag{3.17}$$

Note that $U = U_e$ for $r \geq \delta$, hence Eqs. 3.16 and 3.17 can be written as,

$$(\delta^* + a)^2 - a^2 = 2\int_a^{a+k\delta} \left(1 - \frac{U}{U_e}\right) r dr, \tag{3.18}$$

$$(\theta + a)^2 - a^2 = 2\int_a^{a+k\delta} \frac{U}{U_e}\left(1 - \frac{U}{U_e}\right) r dr, \tag{3.19}$$

since $k \geq 1$. Differentiating both sides with respect to x gives,

$$2(\delta^* + a)\frac{d\delta^*}{dx} = -\frac{2}{U_e}\int_a^{a+k\delta} \frac{\partial(rU)}{\partial x} dr + \frac{2}{U_e^2}\frac{\partial U_e}{\partial x}\int_a^{a+k\delta} U r dr \tag{3.20}$$

$$\begin{aligned} 2(\theta + a)\frac{d\theta}{dx} = {} & \frac{2}{U_e}\int_a^{a+k\delta} \frac{\partial(rU)}{\partial x} dr - \frac{2}{U_e^2}\frac{\partial U_e}{\partial x}\int_a^{a+k\delta} U r dr \\ & - \frac{2}{U_\infty^2}\int_a^{a+k\delta} \frac{\partial(rU^2)}{\partial x} dr + \frac{4}{U_\infty^3}\frac{\partial U_e}{\partial x}\int_a^{a+k\delta} U^2 r dr. \end{aligned} \tag{3.21}$$

Using Eqs. 3.3 and 3.10 in the right hand side of Eqs. 3.20 and 3.21 give,

$$2(\delta^* + a)\frac{d\delta^*}{dx} = 2\frac{V_a}{U_e}(a + k\delta) - 2\frac{\beta_{RC}}{\delta^*}\frac{u_\tau^2}{U_e^2}\int_a^{a+k\delta}\frac{U}{U_e}rdr, \tag{3.22}$$

$$\begin{aligned} 2(\theta + a)\frac{d\theta}{dx} &= -2\frac{V_a}{U_e}(a + k\delta) + 2\frac{\beta_{RC}}{\delta^*}\frac{u_\tau^2}{U_e^2}\int_a^{a+k\delta}\frac{U}{U_e}rdr \\ &+2\frac{V_a}{U_e}(a + k\delta) + \frac{\beta_{RC}}{\delta^*}\frac{u_\tau^2}{U_e^2}r^2\Big|_a^{a+k\delta} + 2a\frac{u_\tau^2}{U_e^2} - 4\frac{\beta_{RC}}{\delta^*}\frac{u_\tau^2}{U_e^2}\int_a^{a+k\delta}\frac{U^2}{U_e^2}rdr \\ \implies 2(\theta + a)\frac{d\theta}{dx} &= 2a\frac{u_\tau^2}{U_e^2} + 2\frac{\beta_{RC}}{\delta^*}\frac{u_\tau^2}{U_e^2}\int_a^{a+k\delta}\frac{U}{U_e}rdr + \frac{\beta_{RC}}{\delta^*}\frac{u_\tau^2}{U_e^2}r^2\Big|_a^{a+k\delta} \\ &\quad -4\frac{\beta_{RC}}{\delta^*}\frac{u_\tau^2}{U_e^2}\int_a^{a+k\delta}\frac{U^2}{U_e^2}rdr. \end{aligned} \tag{3.23}$$

Dividing Eq. 3.22 by Eq. 3.23 and using Eq. 3.15 followed by rearranging the terms, we get,

$$\left(\frac{\delta^* + a}{\theta + a}\right)H = \left[\frac{2\frac{V_a}{U_e}(a + k\delta) - 2\frac{\beta_{RC}}{\delta^*}\frac{u_\tau^2}{U_e^2}I}{2a\frac{u_\tau^2}{U_e^2} + 2\frac{\beta_{RC}}{\delta^*}\frac{u_\tau^2}{U_e^2}I + \frac{\beta_{RC}}{\delta^*}\frac{u_\tau^2}{U_e^2}r^2\Big|_a^{a+k\delta} - 4\frac{\beta_{RC}}{\delta^*}\frac{u_\tau^2}{U_e^2}J}\right] \tag{3.24}$$

where,

$$I = \int_a^{a+k\delta}\frac{U}{U_e}rdr, \tag{3.25}$$

$$J = \int_a^{a+k\delta}\frac{U^2}{U_e^2}rdr. \tag{3.26}$$

Using the definitions of δ^* (Eq. 3.18) and θ (Eq. 3.19), it can be shown that,

$$I = \frac{r^2}{2}\Big|_a^{a+k\delta} - \frac{r^2}{2}\Big|_a^{a+\delta^*}, \tag{3.27}$$

$$J = \frac{r^2}{2}\Big|_a^{a+k\delta} - \frac{r^2}{2}\Big|_a^{a+\delta^*} - \frac{r^2}{2}\Big|_a^{a+\theta}. \tag{3.28}$$

Also, Eq. 3.22 gives,

$$\begin{aligned}(\delta^* + a)\frac{d\delta^*}{dx} &= \frac{V_a}{U_e}(a + k\delta) - \frac{\beta_{RC}}{\delta^*}\frac{u_\tau^2}{U_e^2}I \\ \implies \frac{V_a}{U_e}(a + k\delta) &= (\delta^* + a)\frac{d\delta^*}{dx} + \frac{\beta_{RC}}{2\delta^*}\frac{u_\tau^2}{U_e^2}\left(r^2\Big|_a^{a+k\delta} - r^2\Big|_a^{a+\delta^*}\right). \qquad (3.29)\end{aligned}$$

Hence, Eq. 3.24 can be rearranged to show that,

$$\begin{aligned}\left(\frac{\delta^* + a}{\theta + a}\right)H\Bigg[2a\frac{u_\tau^2}{U_e^2} + \frac{\beta_{RC}}{\delta^*}\frac{u_\tau^2}{U_e^2}\left(r^2\Big|_a^{a+k\delta} - r^2\Big|_a^{a+\delta^*}\right) + \frac{\beta_{RC}}{\delta^*}\frac{u_\tau^2}{U_e^2}r^2\Big|_a^{a+k\delta} \\ -2\frac{\beta_{RC}}{\delta^*}\frac{u_\tau^2}{U_e^2}\left(r^2\Big|_a^{a+k\delta} - r^2\Big|_a^{a+\delta^*} - r^2\Big|_a^{a+\theta}\right)\Bigg] &= \qquad (3.30) \\ 2\frac{V_a}{U_e}(a + k\delta) - \frac{\beta_{RC}}{\delta^*}\frac{u_\tau^2}{U_e^2}\left(r^2\Big|_a^{a+k\delta} - r^2\Big|_a^{a+\delta^*}\right) \\ \implies 2\frac{V_a U_e}{u_\tau^2}(a + k\delta)\left(\frac{\theta + a}{\delta^* + a}\right) = H\left[2a + \frac{\beta_{RC}}{\delta^*}\left(r^2\Big|_a^{a+\delta^*} + 2r^2\Big|_a^{a+\theta}\right)\right] \\ + \left(\frac{\theta + a}{\delta^* + a}\right)\frac{\beta_{RC}}{\delta^*}\left(r^2\Big|_a^{a+k\delta} - r^2\Big|_a^{a+\delta^*}\right) \qquad (3.31)\end{aligned}$$

Substituting for V_a from Eq. 3.29 and rearranging,

$$\begin{aligned}(\theta + a)\frac{d\delta^*}{dx} &= H\frac{u_\tau^2}{U_e^2}\left[a + \frac{\beta_{RC}}{2\delta^*}\left(r^2\Big|_a^{a+\delta^*} + 2r^2\Big|_a^{a+\theta}\right)\right] \\ \implies \frac{u_\tau^2}{U_e^2} &= \frac{(\theta + a)\frac{d\delta^*}{dx}}{H\left[a + \frac{\beta_{RC}}{2\delta^*}\left(r^2\Big|_a^{a+\delta^*} + 2r^2\Big|_a^{a+\theta}\right)\right]} \\ \implies C_f &= \frac{2(1 + \frac{\theta}{a})\frac{d\delta^*}{dx}}{H + \beta_{RC}\left[2 + H\left(1 + \frac{\delta^*}{2a} + \frac{\theta^2}{a\delta^*}\right)\right]} \qquad (3.32)\end{aligned}$$

Self-similarity of boundary layers implies that δ^*/δ is constant. So C_f can be written

as,

$$C_f = \frac{2(1+\frac{\theta}{a})\frac{\delta^*}{\delta}\frac{d\delta}{dx}}{H+\beta_{RC}\left[2+H\left(1+\frac{\delta^*}{2a}+\frac{\theta^2}{a\delta^*}\right)\right]}. \tag{3.33}$$

Note that $C_f = 2u_\tau^2/U_e^2$ is related to β_{RC} by definition (see Eq. 3.5). But that definition contains external flow parameters. On the other hand, Eq. 3.33 relates C_f to the boundary layer parameters directly. Also, Eq. 3.31 can be rearranged to show that,

$$\frac{U_e V_a}{u_\tau^2}\left(\frac{1+\theta/a}{1+\delta^*/a}\right)\left(1+k\frac{\delta}{a}\right) = H+\beta_{RC}\left[2+H\left(1+\frac{\delta^*}{2a}+\frac{\theta^2}{a\delta^*}\right)+\left(\frac{1+\theta/a}{1+\delta^*/a}\right)\left(k\frac{\delta}{\delta^*}-1+\frac{k^2\delta^2-\delta^{*2}}{2a\delta^*}\right)\right] \tag{3.34}$$

At the edge of the boundary layer, $k = 1$ and $V_a = V_e$. Therefore,

$$\frac{U_e V_e}{u_\tau^2}\left(\frac{1+\theta/a}{1+\delta^*/a}\right)\left(1+\frac{\delta}{a}\right) = H+\beta\left[2+H\left(1+\frac{\delta^*}{2a}+\frac{\theta^2}{a\delta^*}\right)+\left(\frac{1+\theta/a}{1+\delta^*/a}\right)\left(\frac{\delta}{\delta^*}-1+\frac{\delta^2-\delta^{*2}}{2a\delta^*}\right)\right] \tag{3.35}$$

At the verge of separation, u_τ goes to zero. Using Eq. 3.5, this gives,

$$V_e = -\delta^*\frac{dU_e}{dx}\left(\frac{1+\theta/a}{1+\delta^*/a}\right)^{-1}\left(1+\frac{\delta}{a}\right)^{-1}\left[2+H\left(1+\frac{\delta^*}{2a}+\frac{\theta^2}{a\delta^*}\right)+\left(\frac{1+\theta/a}{1+\delta^*/a}\right)\left(\frac{\delta}{\delta^*}-1+\frac{\delta^2-\delta^{*2}}{2a\delta^*}\right)\right] \tag{3.36}$$

3.2 Comparison to previous work

3.2.1 Consistency with planar boundary layer relations

For a planar boundary layer, $1/a$ approaches 0 as a approaches ∞. Setting $1/a = 0$ in Eqs. 3.33 and 3.34 gives,

$$C_f = \frac{2\frac{\delta^*}{\delta}\frac{d\delta}{dx}}{H + \beta_{RC}\left(2 + H\right)}, \quad \text{and} \tag{3.37}$$

$$\frac{U_e V_a}{u_\tau^2} = H + \beta_{RC}\left(1 + H + k\frac{\delta}{\delta^*}\right). \tag{3.38}$$

At the verge of separation, $u_\tau = 0$; setting $k = 1$ gives,

$$V_e = -\delta^* \frac{dU_e}{dx}\left(1 + H + \frac{\delta}{\delta^*}\right). \tag{3.39}$$

These relations are identical to those derived by Wei et al. [40] (Eqs. 13 and 14 of their paper) for planar boundary layer with pressure gradient. They compared their analytical relations to the data available in literature for APG TBL and found good agreement (see Figure 2-5 of their paper).

Setting $\beta_{RC} = 0$ in Eq. 3.37 gives,

$$\frac{U_e V_a}{u_\tau^2} = H. \tag{3.40}$$

Note that for $\beta_{RC} = 0$, regardless of the value of k, V_a is same i.e. $V_a = V_e$ is constant outside the boundary layer. Eq. 3.40 was derived by Wei and Klewicki [39] (Eq. 11 of their paper) and shown to be valid for laminar, transitional and turbulent boundary layers.

3.2.2 Axisymmetric ZPG laminar boundary layer

The SBK solution [13, 14] for axisymmetric laminar boundary layer is valid up to $\frac{\nu x}{U a^2} < 0.04$, and was subsequently extended by Glauert and Lighthill [15] (GL) to the interval

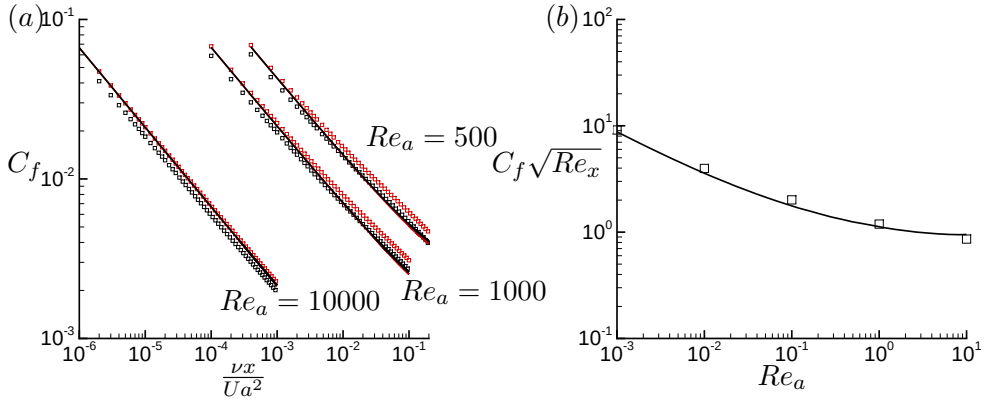

Figure 3.1: Skin-friction coefficient (C_f) as a function of non-dimensional parameter $\frac{\nu x}{Ua^2}$ (a), where results for radius based Reynolds number $Re_a = 500$, 1000 and 10000 are shown along with solutions of Seban–Bond–Kelly [13, 14](□) and Glauert–Lighthill [15](□). The present result using δ^* from SBK (−) and GL (−), show identical C_f. C_f as a function of Re_a is compared to the result of Cebeci [20] (□) for long thin cylinder (large x/a), where boundary layer thickness reaches asymptotic value [16](b).

$0.04 < \frac{\nu x}{Ua^2} < 100$. For ZPG laminar axisymmetric boundary layer, Eq. 3.33 becomes,

$$C_{f,axisymmetric} = 2\frac{d\theta}{dx}\left(1 + \frac{\theta}{a}\right) = C_{f,planar}\left(1 + \frac{\delta^*}{aH}\right). \tag{3.41}$$

δ^* can be obtained from either SBK or GL solutions and $H = 2.59$ for a laminar boundary layer. Thus, C_f can be obtained. Figure 3.1(a) shows C_f as a function of $\frac{\nu x}{Ua^2}$ for three different $Re_a = 10000$, 1000 and 500, compared with both SBK and GL solutions. Note that the difference in C_f using δ^* from either solution (SBK or GL) is negligible. Our results smoothly transition from SBK to GL solution as $\frac{\nu x}{Ua^2}$ increases, as evident in the lower Re_a cases. Figure 3.1(b) compares our result to the numerical solution of Cebeci [20], where Re_a is varied. δ^* and H for this case are estimated from the asymptotic results of Stewartson [16]. Overall, our results show good agreement for the entire range from thin to thick axisymmetric laminar boundary layer.

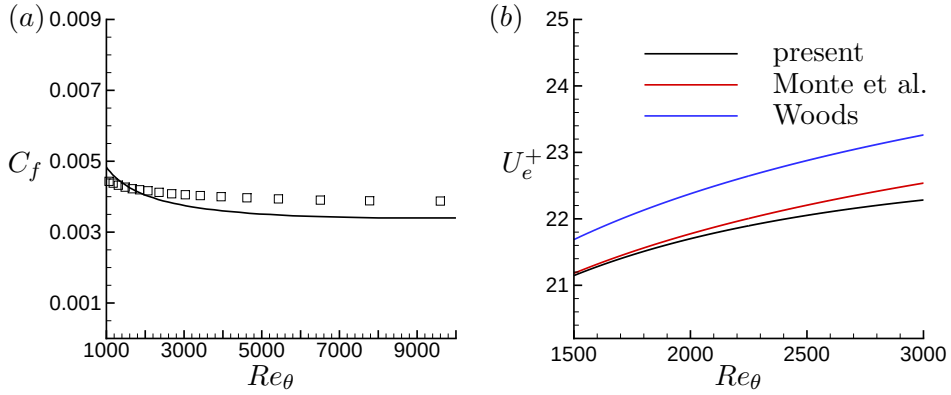

Figure 3.2: (a) Skin-friction coefficient (C_f) as a function of Re_θ is compared to the result of Cebeci [20](□) for slender cylinder for radius based Reynolds number $Re_a = 40200$ and radius $a = 1''$. The shape factor of $H = 1.4$ and $C_{f,planar}$ correlation of Monkewitz et al. [134] is used in our relation to predict C_f. The boundary layer growth is assumed identical to that of flat plate, which need not be true for slender cylinders at high Re_θ. (b) U_e^+ as a function of Re_θ is compared with the correlations of Monte et al. [137] and Woods [136]. U_e^+ is related to C_f as $U_e^+ = \sqrt{2/C_f}$.

3.2.3 Axisymmetric ZPG turbulent boundary layer

Cebeci [20] numerically solved incompressible turbulent ZPG axial flow over a circular slender cylinder of radius, $a = 1''$ and $Re_a = 40200$. The same relation Eq. 3.41 is used to estimate C_f but the $C_{f,planar}$ correlation of Monkewitz et al. [134] is used. The shape factor H is assumed to be 1.4 and the boundary layer growth $d\theta/dx$ is assumed identical in both planar and axisymmetric case. Figure 3.2(a) shows our results compared to that of Cebeci [20]. Note that the range of Re_θ on the cylinder is large ($1000 < Re_\theta < 10000$). Hence, the assumption of identical growth and $H = 1.4$ may not hold, which is the reason for difference between our result and that of Cebeci [20].

Kumar and Mahesh [100] simulated thin axisymmetric TBL in the range $1400 < Re_\theta < 1620$. Using their boundary layer δ^* and θ variation with streamwise distance x, which is almost linear, their slope $d\delta^*/dx$ and $d\theta/dx$ can be estimated. This estimated slope can be used to compute C_f for $1500 < Re_\theta < 3000$ as shown in Figure 3.2(b). Our results show good agreement with the correlation of Monte et al. [137], who corrected

the correlation of Woods [136] using their simulation database. Note that for a large range of Re_θ, the assumption of linear growth of boundary layer breaks down, hence the differences at large Re_θ.

3.3 Discussion

3.3.1 Effect of curvature on C_f

If both planar and axisymmetric boundary layers have the same boundary layer parameters, Eqs. 3.33 and 3.37 yield:

$$\begin{aligned}
\frac{C_{f,axisymmetric}}{C_{f,planar}} &= \frac{\left(1+\frac{\theta}{a}\right)\left[H+\beta_{RC}\left(2+H\right)\right]}{H+\beta_{RC}\left[2+H\left(1+\frac{\delta^*}{2a}+\frac{\theta^2}{a\delta^*}\right)\right]} \\
\implies \frac{C_{f,axisymmetric}}{C_{f,planar}} - 1 &= \frac{\frac{\theta}{a}\left[H+\beta_{RC}\left(2+H\right)\right] - \beta_{RC}H\left(\frac{\delta^*}{2a}+\frac{\theta^2}{a\delta^*}\right)}{H+\beta_{RC}\left[2+H\left(1+\frac{\delta^*}{2a}+\frac{\theta^2}{a\delta^*}\right)\right]} \\
&= \frac{\frac{\theta}{a}H+\beta_{RC}\left[\frac{\theta}{a}+\frac{\delta^*}{a}\left(1-\frac{H}{2}\right)\right]}{H+\beta_{RC}\left[2+H\left(1+\frac{\delta^*}{2a}+\frac{\theta^2}{a\delta^*}\right)\right]}
\end{aligned} \tag{3.42}$$

Thus, if the right hand side of Eq. 3.42 is positive, the presence of curvature increases C_f and vice-versa.

It is easy to see that for ZPG ($\beta_{RC} = 0$) boundary layers,

$$\frac{C_{f,axisymmetric}}{C_{f,planar}} = 1 + \frac{\theta}{a}. \tag{3.43}$$

For boundary layer with APG ($\beta_{RC} > 0$), the denominator of the right hand side of Eq. 3.42 is always positive. Hence, the effect of curvature will depend on the sign of

the numerator,

$$\eta = \frac{\theta}{a}H + \beta_{RC}\left[\frac{\theta}{a} + \frac{\delta^*}{a}\left(1 - \frac{H}{2}\right)\right]. \tag{3.44}$$

It can be shown that $\eta \geq 0$ if $\beta_{RC} \geq 0$ as follows. It is known that, $H \geq 1$ which gives,

$$\frac{H}{2} \geq \frac{1}{2} \implies \frac{H}{2} - 1 \geq -\frac{1}{2}, \tag{3.45}$$

$$\frac{1}{H} \leq 1 \implies -\frac{1}{H} \geq -1. \tag{3.46}$$

Adding Eqs. 3.45 and 3.46 we get,

$$\frac{H}{2} - 1 - \frac{1}{H} \geq -\frac{3}{2}, \implies \frac{1}{\frac{H}{2} - 1 - \frac{1}{H}} \leq -\frac{2}{3}. \tag{3.47}$$

But,

$$\frac{1}{\frac{H}{2} - 1 - \frac{1}{H}} = \frac{H}{H(\frac{H}{2} - 1) - 1} = \frac{-\frac{\theta}{a}H}{\frac{\theta}{a} + H\frac{\theta}{a}\left(1 - \frac{H}{2}\right)} = \frac{-\frac{\theta}{a}H}{\frac{\theta}{a} + \frac{\delta^*}{a}\left(1 - \frac{H}{2}\right)}. \tag{3.48}$$

From Eqs. 3.47 and 3.48, it follows that,

$$\frac{-\frac{\theta}{a}H}{\frac{\theta}{a} + \frac{\delta^*}{a}\left(1 - \frac{H}{2}\right)} \leq -\frac{2}{3}. \tag{3.49}$$

Now,

$$\begin{aligned} \eta = \frac{\theta}{a}H + \beta_{RC}\left[\frac{\theta}{a} + \frac{\delta^*}{a}\left(1 - \frac{H}{2}\right)\right] > 0 \\ \iff \beta_{RC} > \frac{-\frac{\theta}{a}H}{\frac{\theta}{a} + \frac{\delta^*}{a}\left(1 - \frac{H}{2}\right)}. \end{aligned} \tag{3.50}$$

Using Eq. 3.49, it is easy to see that Eq. 3.50 always holds for $\beta_{RC} > 0$.

Therefore, the presence of curvature increases C_f if $\beta_{RC} \geq 0$. Note that, this is true regardless of the value of a. It has been assumed that $d\delta/dx$ is identical for both planar and axisymmetric TBL. This is not be always true. In fact, for thick axisymmetric TBL at zero-pressure-gradient ($\delta/a \gg 1$ and $\beta_{RC} = 0$), $d\delta/dx$ is smaller than that of planar TBL value [30]. However, C_f is still higher than planar values because $\theta/a \gg 1$, which compensates for the decrease in $d\delta/dx$.

The presence of curvature may or may not increase C_f in FPG axisymmetric TBL depending on the sign of the right hand side of Eq. 3.42.

3.3.2 Thick axisymmetric ZPG turbulent boundary layer

For $\beta_{RC} = 0$, the expression for C_f reduces to,

$$C_f = 2\left(1 + \frac{\theta}{a}\right)\frac{\theta}{\delta}\frac{d\delta}{dx} \tag{3.51}$$

Thus, knowing local boundary layer parameters, C_f can be estimated. For example, Jordan [33] compiled numerous experimental results along with his simulation database for thick axisymmetric TBL in ZPG and showed that $\delta/\theta \approx 7.2$. The estimated value of $d\delta/dx \approx 2.5 \times 10^{-3}$ for a range of thick axisymmetric TBL ($2.1 \leq \delta/a \leq 11$, $37 \leq a^+ \leq 388$, $586 \leq Re_a \leq 7475$). This makes,

$$C_f = 6.94 \times 10^{-4}\left(1 + \frac{\theta}{a}\right) = 6.94 \times 10^{-4}\left(1 + \frac{Re_\theta}{Re_a}\right). \tag{3.52}$$

3.3.3 Axisymmetric turbulent boundary layer under large APG

For large APG, $\beta_{RC} \gg 1$. Thus Eq. 3.33 gives,

$$C_f \approx \left[\frac{2(1+\frac{\theta}{a})\frac{\delta^*}{\delta}\frac{d\delta}{dx}}{2 + H\left(1 + \frac{\delta^*}{2a} + \frac{\theta^2}{a\delta^*}\right)}\right]\frac{1}{\beta_{RC}}. \tag{3.53}$$

For self-similar TBL in APG, δ^*/δ, H and $d\delta/dx$ become constant [138]. Similar behavior is expected for axisymmetric TBL as well. When $\delta/a < 1$, θ/a and δ^*/a are small as compared to 1. This makes, the term inside brackets ([ ]) nearly constant. Thus for thin axisymmetric TBL at large APG, $C_f \sim 1/\beta_{RC}$. A similar result was obtained by Wei et al. [40] for planar TBL.

3.3.4 Axisymmetric turbulent boundary layer under FPG

For FPG TBL, there are two important flow parameters: pressure gradient parameter (Λ) [139] and acceleration parameter (K) [140] defined as,

$$\Lambda = -\frac{\delta}{u_\tau^2}\frac{1}{\rho}\frac{dp}{dx}, \tag{3.54}$$

$$K = \frac{\nu}{U_e^2}\frac{dU_e}{dx}. \tag{3.55}$$

All the relations derived in §3.1 hold for FPG axisymmetric TBL as well, by replacing β_{RC} with $-\Lambda$. It can be shown that,

$$\frac{dC_f}{d\Lambda} = C_f\left[\frac{2 + H\left(1 + \frac{\delta^*}{a} + \frac{\theta^2}{a\delta^*}\right)}{H - \Lambda\left[2 + H\left(1 + \frac{\delta^*}{a} + \frac{\theta^2}{a\delta^*}\right)\right]}\right] < 0. \tag{3.56}$$

Thus, increasing FPG decreases C_f and this effect is expected to be enhanced by the presence of transverse curvature as the presence of terms with $1/a$ enhance the magnitude of $dC_f/d\Lambda$.

3.4 Summary

The integral analysis of equations governing axisymmetric boundary layer flow is presented, including the effect of pressure gradient. Analytical relations are derived relating C_f to the boundary layer parameters. The relations for planar TBL with and without pressure gradient presented by Wei et al. [40] and Wei and Klewicki [39] respectively can be recovered by setting $1/a = 0$ and further setting $\beta_{RC} = 0$. It has been shown

that the presence of transverse curvature increases C_f regardless of the nature of boundary layer, consistent with the observations reported in the literature for both ZPG and APG axisymmetric boundary layers. The derived relations are compared to the existing results in the literature showing good agreement. The results presented in this chapter apply on both laminar and turbulent regimes as long as the boundary layer approximation is valid. The derived expressions can help understand and predict the behavior of axisymmetric boundary layer flows under pressure gradients and can be used to devise engineering models for skin-friction for such flows.

Chapter 4

LES of flow over hull

In this chapter, wall-resolved LES of flow over the axisymmetric hull is performed at $Re = 1.1 \times 10^6$, based on length of the hull and freestream velocity. The objectives of this chapter are to evaluate the ability of LES to predict the flow over axisymmetric hull and characterize the evolution of the axisymmetric wake of the hull. The set-up of the simulation including the computational grid and the boundary conditions, as well as grid convergence are discussed in Section 4.1. Results along with comparison to available data are described in Section 4.2. The chapter is summarized in Section 4.3.

4.1 Simulation details

4.1.1 Computational domain and boundary conditions

LES of flow over a bare hull is performed using a cylindrical computational domain of length $28.8D$ and diameter $12D$, where D is the maximum diameter of the hull. The origin of the reference coordinate system is located at the nose of the hull. The inflow plane is located $3D$ upstream of the hull while the outflow is located $17.2D$ downstream of the stern. Note that the length of the hull is $L = 8.6D$. Preliminary simulations were used to estimate the size of the required computational domain and are discussed in Section 4.1.2. The current computational domain is bigger than that used by Posa and Balaras [55] to simulate flow over fully-appended SUBOFF at $Re = 1.2 \times 10^6$.

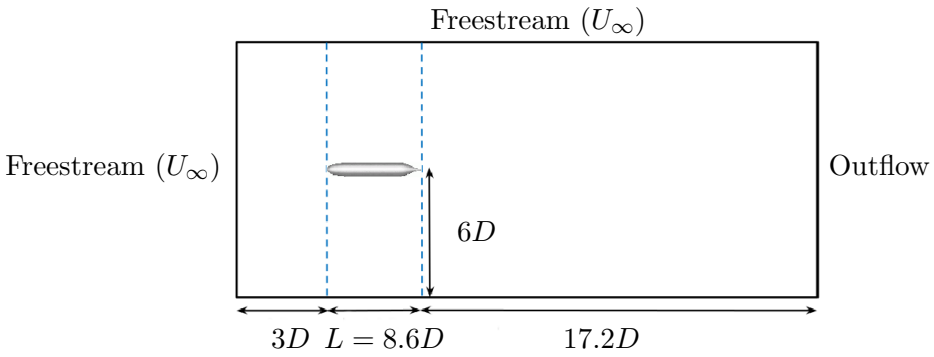

Figure 4.1: The computational domain used for simulations of flow over hull.

The physical conditions of the present simulations are identical to that of the experiments conducted by Jiménez et al. [47], with the difference that a semi-infinite sail was used as support in the experiments. The hull boundary layer in the simulations stays laminar if untripped. The hull boundary layer therefore is tripped at the same location ($x/D = 0.75$) as that of the experiment, by applying a steady wall-normal velocity perturbation. This lifts the boundary layer and mimics the presence of a trip wire. This method of tripping was tested in preliminary simulations (see Appendix A), where a small steady wall-normal velocity over few cells quickly transitioned an axisymmetric laminar boundary layer to turbulence.

The computations reported in this chapter are performed on an unstructured grid consisting of approximately 608 million hexahedral control volumes partitioned over 8192 processors. The computational time step $tU/D = 0.0006$ is used. The simulations are performed for over two flow-through times to discard transients and the results are sampled for another two flow-through times to compute converged statistics. Freestream velocity boundary conditions are specified at the inflow and the lateral boundaries. Convective boundary conditions are prescribed at the outflow. No-slip boundary conditions are prescribed on the hull surface. A schematic of the computational domain and the boundary conditions is shown in Figure 4.1.

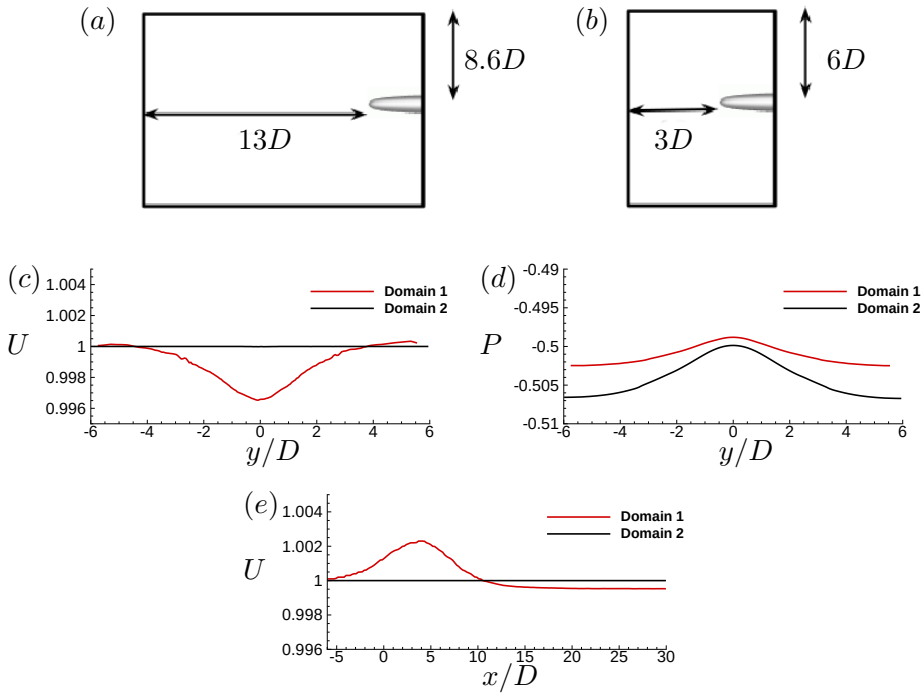

Figure 4.2: Inflow confinement: instantaneous axial velocity, U and pressure difference from the stagnation (nose of hull), P are compared at $x/D = -3$ for the two domains as shown. Domain 2 has negligible confinement.

4.1.2 Grid convergence and sensitivity

The size of the computational domain was chosen based on the results of preliminary simulations on a coarse grid. The preliminary simulations were performed on two domains (Figure 4.2a,b), Domain 1 and 2 to assess confinement effects. Profiles of axial velocity and pressure are extracted and compared at $x/D = -3$ for both the domains in Figure 4.2(c) and (d) respectively. The pressure at the stagnation point on the nose of the hull is used as reference pressure. Figure 4.2(e) shows the axial velocity profile at a radial distance of $6D$ for both the domains. It can be concluded that choosing the inflow plane at $3D$ upstream of the hull and lateral boundary at a radial distance of $6D$ from the axis in the computational domain will have negligible confinement effects.

The thin boundary layer on the hull and the turbulent axisymmetric wake need to be captured, which requires fine resolution. The computational grid used in the

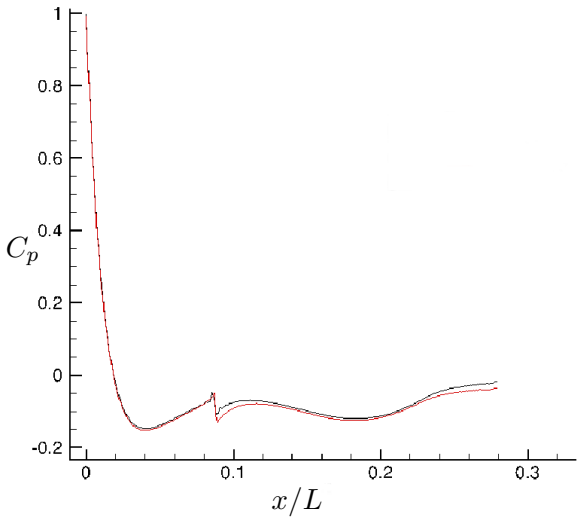

Figure 4.3: Grid convergence for C_p on the bow region: grid with four times streamwise resolution (−) does not change the pressure drop appreciably as compared to the grid used in the present simulations (−) for the bow region.

present simulations is clustered near the surface of the hull with a wall-normal spacing of $0.0003D$ and a growth ratio of 1.01 away from the wall. The near-wall streaks are responsible for the skin-friction, and require fine azimuthal resolution. There are 1600 uniformly spaced cells in the azimuthal direction, yielding azimuthal resolution in wall-units, $a^+\Delta\theta = 11$. The streamwise and first wall-normal grid resolutions are less than 33 and 1 wall units respectively, over most of the hull where the flow is attached. Note that these grid spacings were estimated from a coarse LES simulation at the same Re. This ensures adequate resolution on the mid region of the hull.

Next, the bow and stern regions were assessed for grid convergence as they are crucial for ensuring proper boundary layer and wake. The entire domain was split into different parts – bow, mid and stern regions and simulated individually, to ensure correct solution, before merging them together for the final simulation.

The pressure and skin-friction coefficients are defined as:

$$C_p = \frac{p - p_\infty}{0.5\rho U_\infty^2} \quad \text{and} \quad C_f = \frac{\tau_w}{0.5\rho U_\infty^2}. \tag{4.1}$$

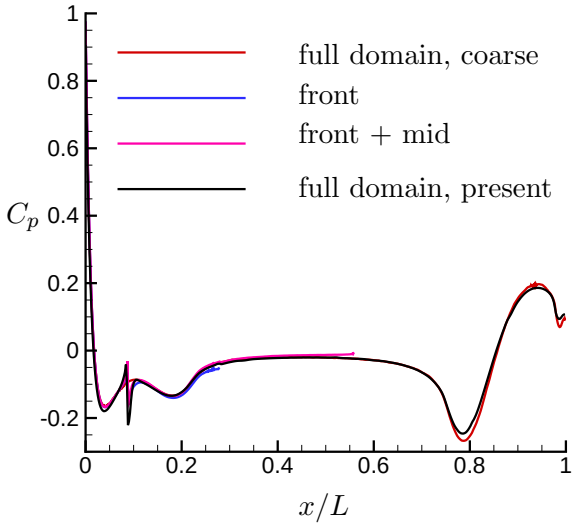

Figure 4.4: Grid convergence for C_p: results from all the preliminary simulations are shown.

The reference pressure (p_∞) is taken at the inflow near the radial boundary, and τ_w is the shear-stress at the wall. Different streamwise resolutions were used to ensure grid convergence in pressure drop on the bow. Refining the grid further in the streamwise direction did not change the pressure drop on the bow appreciably, as shown in Figure 4.3. Profiles of C_p for all the preliminary simulations along with that from the grid used in the present simulations are shown in Figure 4.4.

The wake of the hull is sensitive to properties of the stern boundary layer. The location of flow separation on the stern determines the wake width. Hence, it is important to ensure grid convergence and insensitivity to the flow field in the stern region. Simulations were performed for flow over the entire hull using three different streamwise resolutions on the stern region. All these grids (Grid 1-3) have identical front and mid portion. Figures 4.5(a,b) show evolution of C_f on the hull along with zoomed-in view of the stern region. The change in C_f is insignificant going from Grid 2 to Grid 3. The drag force contribution from both viscous and pressure forces are listed in Table 4.1. There is no difference in the viscous force between Grid 2 and Grid 3. On the other

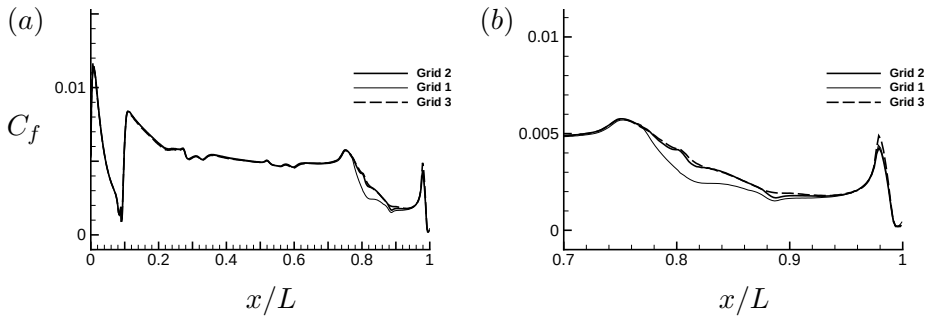

Figure 4.5: Grid convergence for C_f on the hull: Grids 1-3 only differ in stern resolution with Grid 1 being the coarsest and Grid 3 being the finest. The results from Grid 2 are presented in here.

Grid	Stern resolution	F_v	F_p	$F_v + F_p$
1	coarse	0.185	0.035	0.22
2	fine	0.189	0.034	0.223
3	finer	0.189	0.033	0.222

Table 4.1: Grid convergence for drag forces.

hand, the pressure force shows a small ($\sim 3\%$) difference between Grid 2 and Grid 3. Since, the viscous force contributes most of the overall drag force, the difference in the overall drag force between Grid 2 and Grid 3 is negligible ($\sim 0.5\%$). The momentum deficit in the wake of the hull depends on the overall drag. Hence, the results reported here are from Grid 2, which can be considered grid converged.

4.2 Results

4.2.1 Overview of the flow field

The instantaneous near-wall flow structures are visualized in Figure 4.6 using isocontours of Q-criterion [141] colored with axial velocity. The rapid transition following tripping is evident, and the near-wall flow structures appear to be adequately captured. Contours of instantaneous axial velocity, pressure and vorticity magnitude are shown in Figure 4.7. Note that the flow is attached over the entire hull except the stern, as expected for a streamlined geometry. The flow accelerates on the bow due to favorable pressure

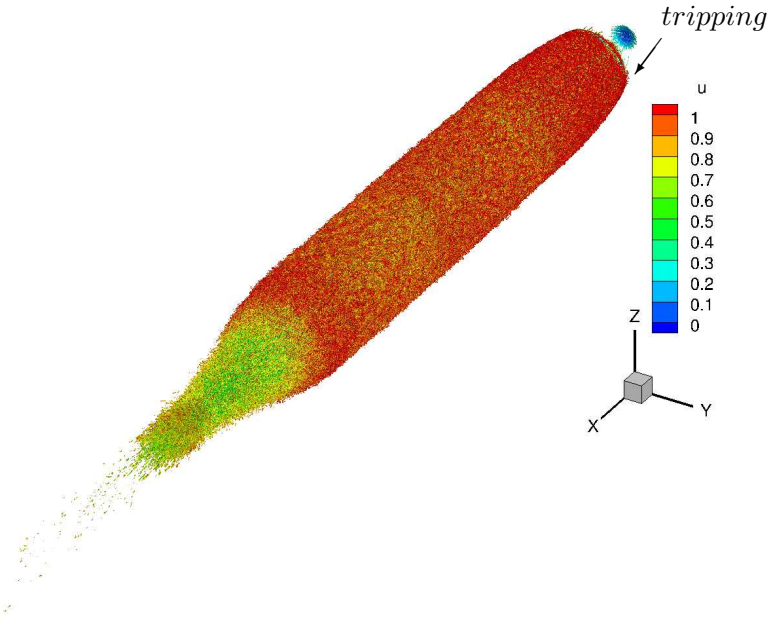

Figure 4.6: The near-wall flow structures on the hull are visualized using isocontour of instantaneous Q-criterion [141] colored with axial velocity. The boundary layer is tripped at the same location as the experiments of Jiménez et al. [47].

gradient, quickly turns turbulent and evolves downstream on the mid portion on the hull, which is a zero-pressure-gradient region. The axisymmetric TBL eventually separates on the stern to form the wake. The pressure gradient is negligible in the wake region away from the stern. The slow radial spreading of the wake with streamwise distance downstream of the hull is also noticeable. The contour plot of vorticity magnitude shows the regions of intense turbulent activity, which are mainly the hull boundary layer and the wake. The magnitude of the vorticity decreases, moving downstream in the wake.

A closer view of the hull boundary layer is shown in Figure 4.8. The effect of tripping and subsequent growth of the hull boundary layer is evident. The thickening of the hull boundary layer due to adverse pressure gradient on the stern can be observed, which eventually leads to flow separation and wake formation. Contours of axial velocity and vorticity magnitudes at transverse planes are shown in Figure 4.8(c,d) at streamwise

location, $x/L = 0.42$. The azimuthal resolution appears to capture the hull boundary layer adequately close to the wall. At this location, the profiles of first and second order velocity statistics are shown in Figure 4.9. The DNS results of a planar TBL at $Re_\theta = 1551$ from Jiménez et al. [133] are also shown for comparison. Although the boundary layer thickness is similar ($\delta^+ \sim 900$), the friction-velocity (u_τ) for the hull boundary layer is higher, which makes U^+ smaller compared to the planar TBL value at similar Re_θ. This is due to the effect of transverse curvature of the hull on the axisymmetric TBL, as observed in past experiments and reviewed by Lueptow [10].

The governing equations can be used to obtain a relation between C_f and the boundary layer quantities for a generic axisymmetric boundary layer evolving under pressure gradients [142] as discussed in Chapter 3. It can be shown that for identical boundary layer parameters (δ, δ^*, θ, $\frac{d\delta}{dx}$), the presence of transverse curvature always increases C_f if $\beta_{RC} \geq 0$.

Radial (u_r) and azimuthal (u_θ) velocity fluctuations are plotted for the hull boundary layer and compared to wall-normal (v) and spanwise (w) velocity fluctuations for planar TBL. All the quantities are normalized using u_τ. A closer view of the velocity fluctuations near the wall is shown in Figure 4.9(c). In general, the axisymmetric TBL shows similar trend as planar TBL. However, the rapid decay in fluctuations away from the wall as compared to planar TBL can be clearly observed. Closer to the wall (see Figure 4.9c), the second-order velocity statistics show good agreement with the planar TBL. The turbulent kinetic energy (TKE) profile of the axisymmetric TBL on the hull is compared to that of the planar TBL in Figure 4.9(d). The TKE profile of the axisymmetric TBL decays faster than that of the planar TBL. Note that the curvature parameter, $\delta/a \approx 0.3$ at this location. It appears that curvature significantly affects the TKE in the log layer. Note the smaller value of Reynolds stress in the log region as well.

Cylindrical slices parallel to the hull surface are extracted at two radial locations, $r = 0.836$ and 0.862, which correspond to $y^+ = 10$ and 110 from the surface respectively, as shown in Figure 4.10. The streaky flow structures in the buffer layer which are source of skin-friction [143], can be observed in Figure 4.10(a) as marked by lower axial velocity.

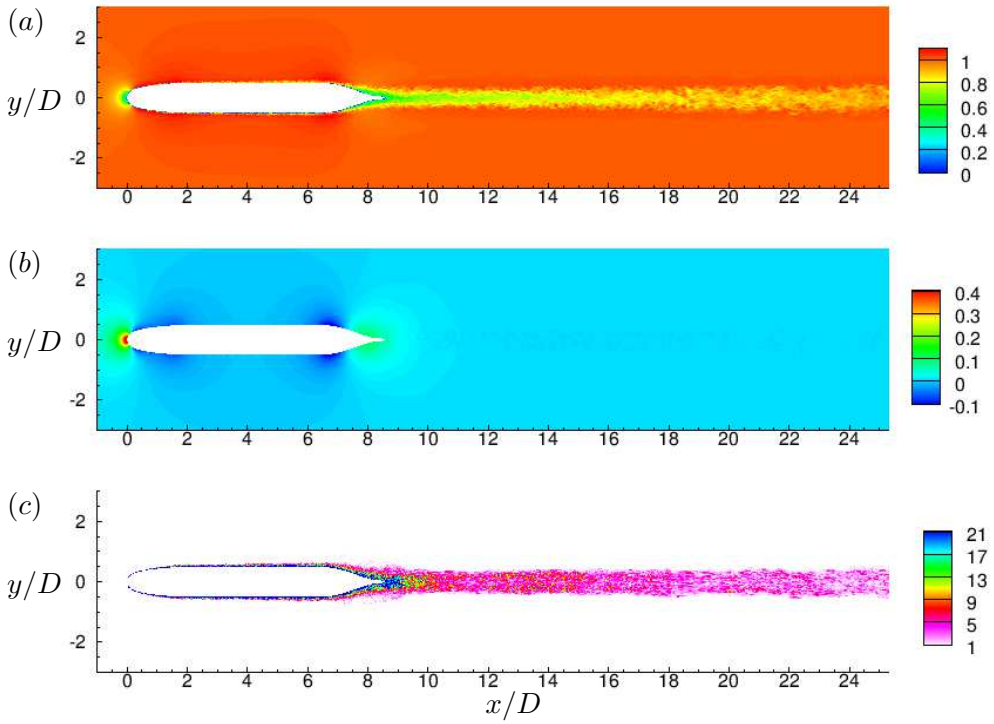

Figure 4.7: The instantaneous flow field: axial velocity (a), pressure (b) and vorticity magnitude (c) in xy plane.

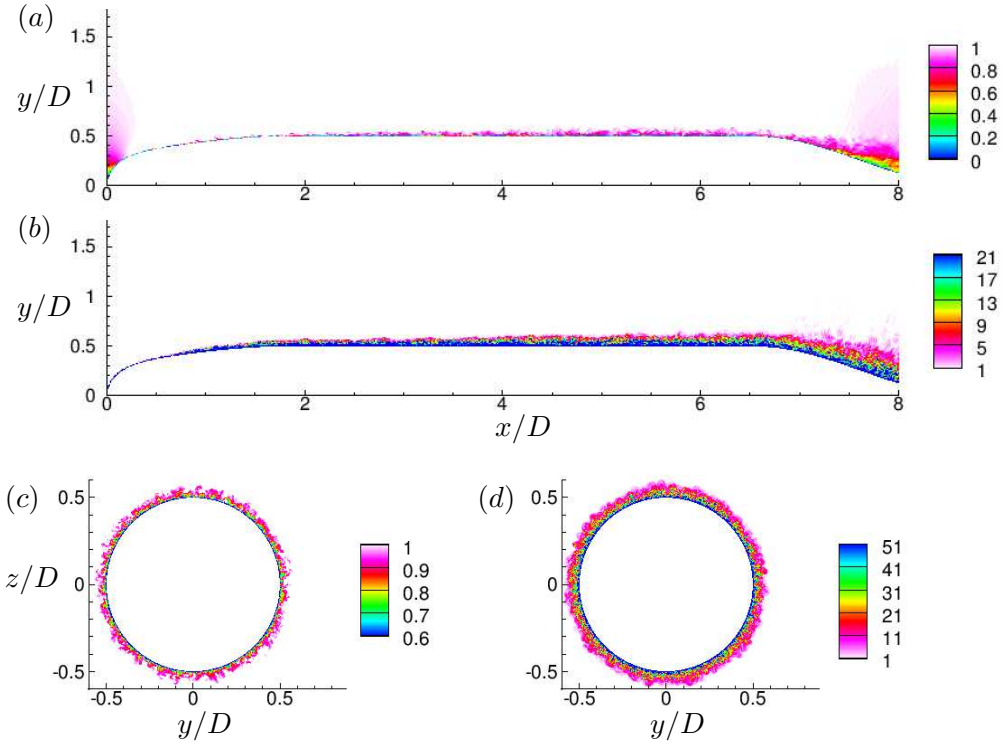

Figure 4.8: Instantaneous axial velocity (a,c) and vorticity magnitude (b,d) in xy (a,b) and yz (c,d) planes in the hull boundary layer. The yz plane is extracted at $x/L = 0.42$ (i.e. $x/D = 3.6$).

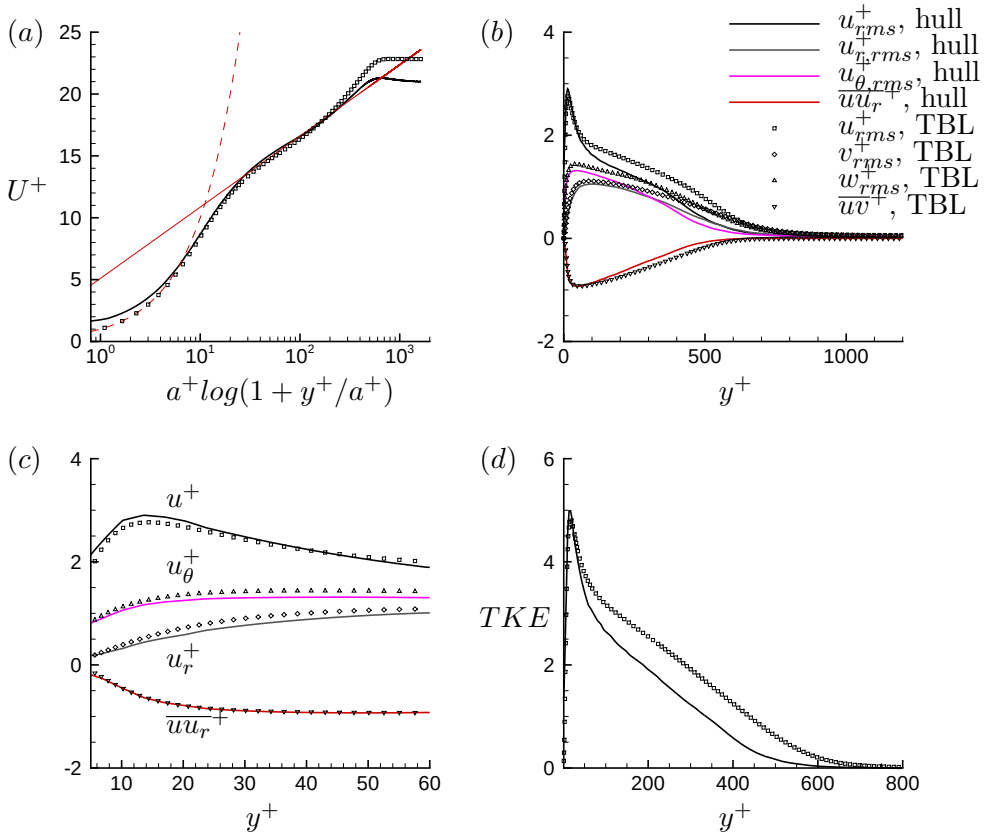

Figure 4.9: Statistics in wall units for hull boundary layer at $x/L = 0.42$ on the hull: mean axial velocity (a) and rms of velocity fluctuations (u^+_{rms}, $u^+_{r,rms}$, $u^+_{\theta,rms}$) and Reynolds stress ($\overline{uv_r}^+$). Symbols show DNS of a planar TBL at $Re_\theta = 1551$ [133]. Zoomed-in view of the profiles of velocity fluctuations near peaks (c) and turbulent kinetic energy profile (d) are also shown.

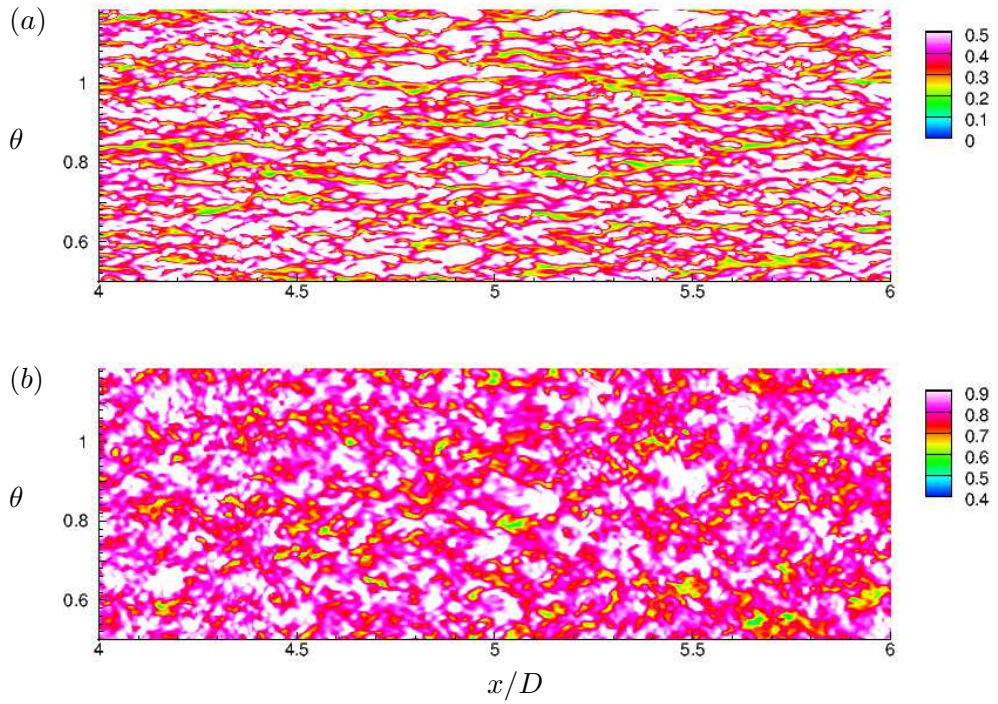

Figure 4.10: Wall-parallel cylindrical surfaces in the hull boundary layer at a radial distance $r = 0.836$ (a) and $r = 0.862$ (b) from the axis. This corresponds to approximate $y^+ = 10$ and 110 respectively away from the hull surface. Instantaneous axial velocity is shown on the mid hull in the buffer and log region of the hull boundary layer.

No such structures are observed in the logarithmic layer.

The streamwise growth of the hull boundary layer is examined using profiles of mean velocities, turbulent intensities and Reynolds stress at multiple locations on the hull ($0.35 \leq x/L \leq 0.63$) in Figure 4.11. Figure 4.11(a) focuses on the flow outside the boundary layer. U_r varies very slowly outside the boundary layer. The first ($x/L = 0.35$) and last ($x/L = 0.63$) location show relatively large variation in U_r outside the boundary layer. In particular, the first location has increasing U_r whereas, the opposite is observed at the last location. This behavior of U_r is due to a small FPG at the first and a small APG at the last location respectively. The spatial growth of the boundary layer thickness is clearly evident (Figure 4.11b-c).

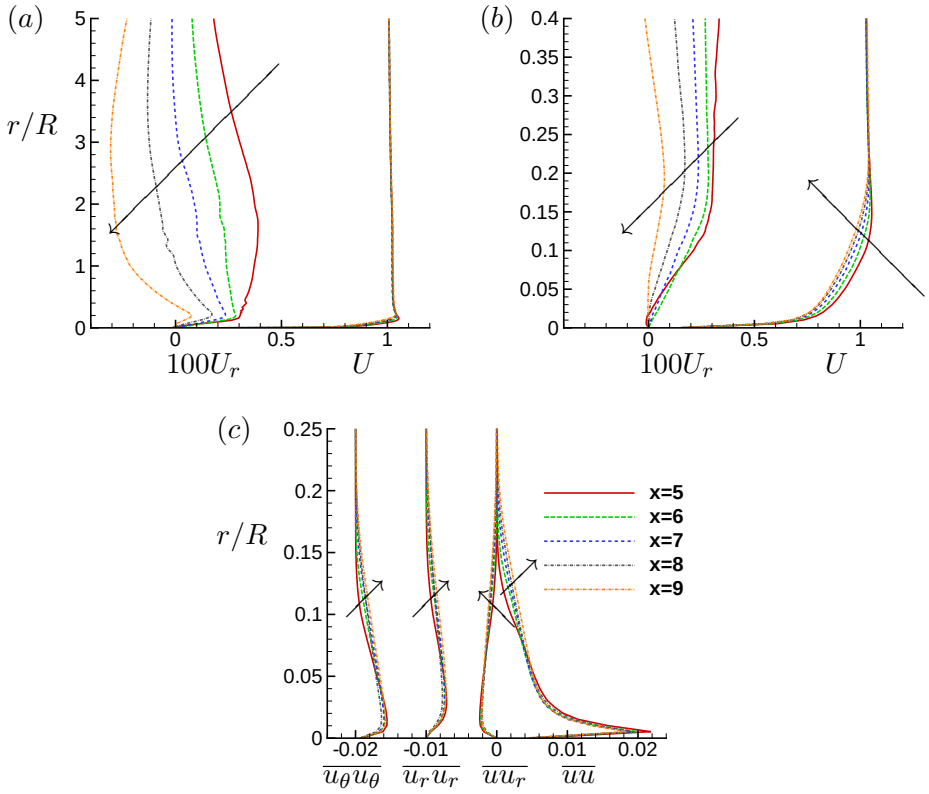

Figure 4.11: Radial profiles of U and U_r (a) along with their close-up near the hull (b) are shown along with $\overline{uu}$, $\overline{u_r u_r}$, $\overline{u_\theta u_\theta}$ and $\overline{u_r u_r}$ at various locations on the hull from $x/L = 0.35$ to 0.63. Note that the profiles of $\overline{u_r u_r}$ and $\overline{u_\theta u_\theta}$ are shifted to left by 0.01 and 0.02 units respectively for clarity. Arrows show the direction of increasing x.

4.2.2 Comparison to experiments

The LES results of the present simulations are compared to the experiments of Huang et al. [46] and Jiménez et al. [47]. Huang et al. [46] conducted experiments of flow over bare hull and reported C_p and C_f on the hull at $Re = 1.2 \times 10^7$. These measurements were made on the bare hull model identical to the present hull and the model was supported by two thin NACA0015 struts (see Huang et al. [46] for details), which had minimal effects on the flow field. Huang et al. [46] reported measurement uncertainty of ± 0.015 and ± 0.0002 for C_p and C_f respectively and the measured C_p was corrected for error due to confinement effects.

Jiménez et al. [47] conducted experiments on the bare hull at $Re = 1.1 \times 10^6$ to 6.7×10^7. The focus of their study was the evolution of intermediate wake, and wake profiles for the first and second order statistics at various streamwise locations downstream from the stern were reported. They did not report the evolution of C_f, or the velocity profiles on the hull. The bare hull in their experiments had a semi-infinite sail, which acted as support. They report an overall blockage of 5.7% in their wind tunnel due to the hull and the semi-infinite sail. The reported C_p was not corrected for confinement and blockage effects.

The C_p measured by Jiménez et al. [47] on the hull did not match with the earlier experiments of Huang et al. [46], which they attributed to the difference in reference pressure. The C_p obtained from the simulations is compared to the experiments of Huang et al. [46] in Figure 4.12(a) showing good agreement, consistent with the results of Posa and Balaras [55]. In rest of this section, LES results are compared to the available experiments. C_p and C_f on the hull, and the profiles of velocity and pressure statistics on the stern are compared to Huang et al. [46]. The wake profiles for mean and variance of axial velocity are compared to the data reported by Jiménez et al. [47].

Note that the experiments of Huang et al. [46] were conducted at $Re = 1.2 \times 10^7$, whereas the simulations reported here is at $Re = 1.1 \times 10^6$. C_p is insensitive to Re for high Re attached flows but C_f depends on Re. Hence, C_f values of the experiments are

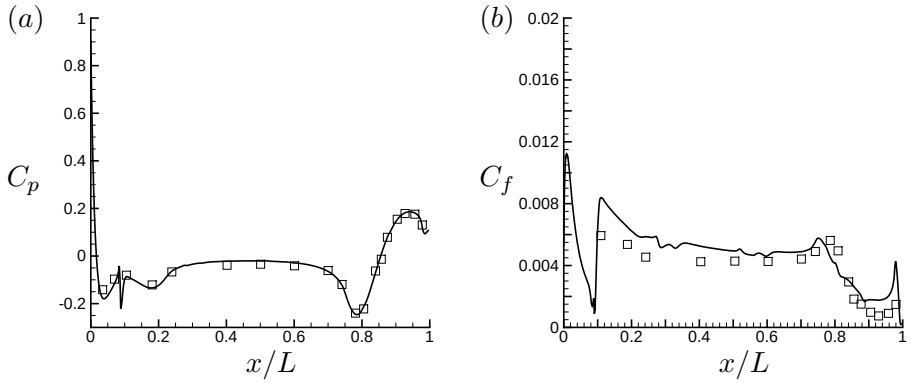

Figure 4.12: Pressure (C_p) (a) and skin-friction (C_f) (b) coefficients on the hull. Symbols are show measurements from the experiments of Huang et al. [46] at $Re = 1.2 \times 10^7$. C_f from the experiments are scaled to the Re of the simulations using scaling law, $C_f \sim Re^{-0.2}$.

scaled to the Re of the simulations using $C_f \sim Re^{-0.2}$ which applies to zero-pressure-gradient boundary layers. Note that the spike visible in the plots at $x/D = 0.75$ is due to tripping. The difference between the C_f from LES and the experiments on the bow and stern region is due to inapplicability of the scaling law in regions of pressure gradient. Overall, LES results show good agreement with the experiments (Figure 4.12b).

Figure 4.13 compares profiles of pressure and velocity to the experiments of Huang et al. [46]. The radial variation of C_p as well as the mean axial (U) and radial (U_r) velocities, rms of velocity fluctuations and Reynolds stress are shown at two streamwise locations on the stern: $x/L = 0.904$ and 0.978. The C_p values obtained from LES show good agreement with that of experiments. The mean velocities (U, U_r) on the other hand show small difference as compared to the experiments, which can be attributed to the difference in Re between the simulations and the experiments. The thickening of the hull boundary layer leading to flow separation due to geometrically induced adverse pressure gradient is evident as we move downstream on the stern. At the same locations, profiles of $\overline{uu_r}$ are compared to the experiments in Figure 4.14. The simulated values at $Re = 1.1 \times 10^6$ are closer to the experiments ($Re = 1.2 \times 10^7$) at the streamwise location $x/L = 0.978$ as compared to $x/L = 0.904$. All these trends (Figures 4.13, 4.14)

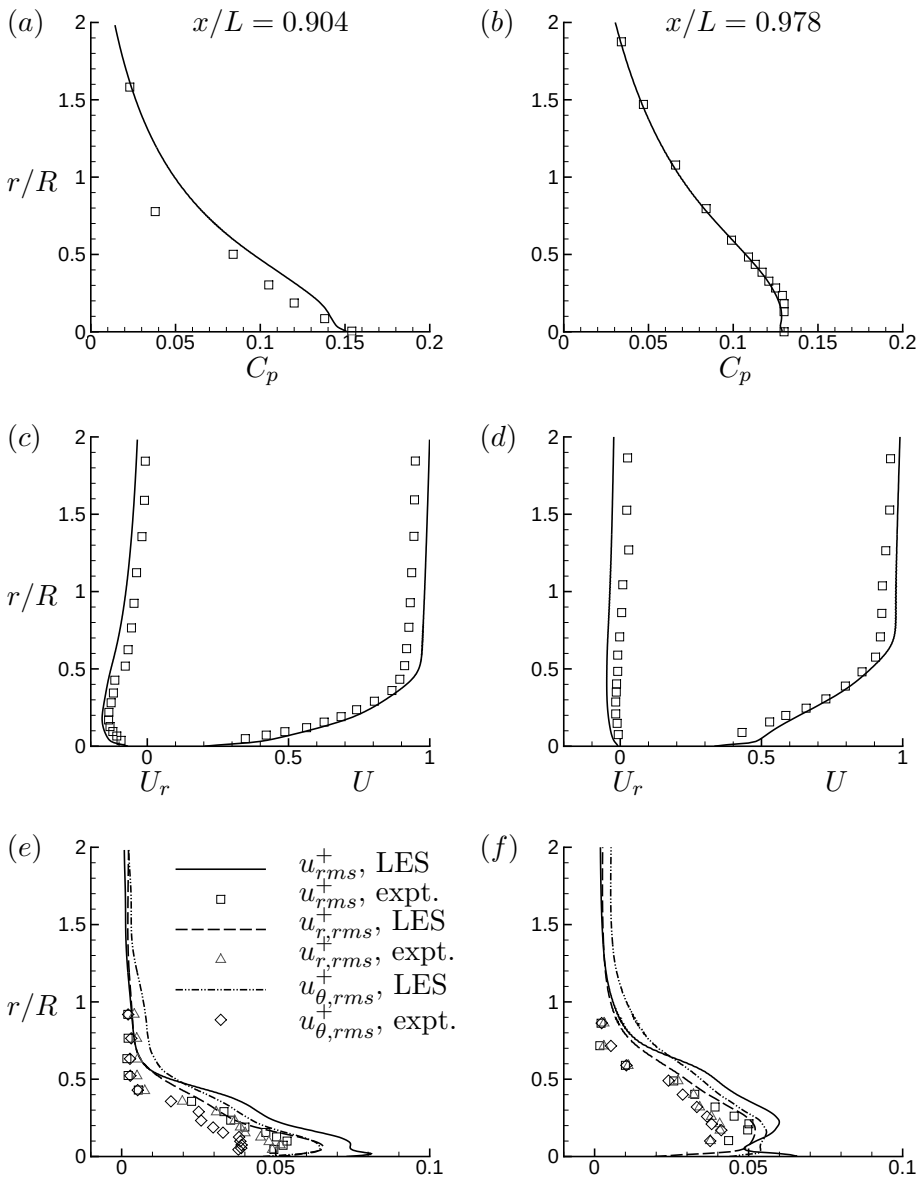

Figure 4.13: Profiles of pressure coefficient (C_p) (a,b), mean axial (U) and radial (U_r) velocity (c,d) and rms of velocity fluctuations (u_{rms},$u_{r,rms}$ and $u_{\theta,rms}$) at $x/L = 0.904$ (a,c,e) and 0.978 (b,d,f). Symbols are show measurements from the experiments of Huang et al. [46] at $Re = 1.2 \times 10^7$.

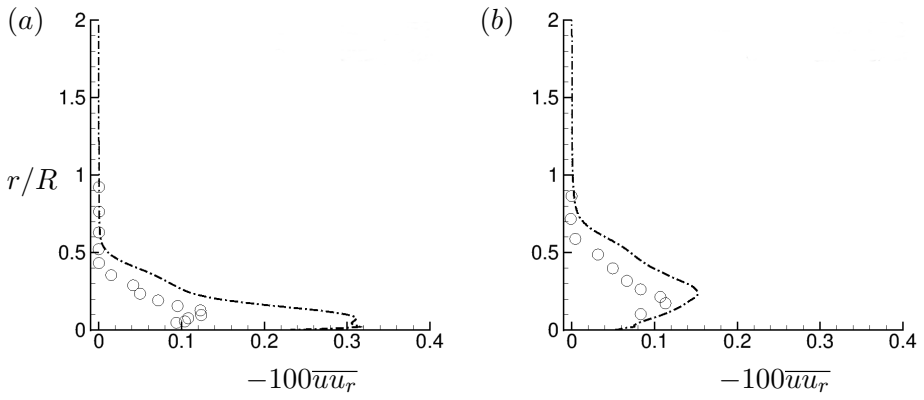

Figure 4.14: The axisymmetric wake: Reynolds stress ($\overline{uu_r}$) at $x/L = 0.904$ (a) and 0.978 (b). Symbols are show measurements from the experiments of Huang et al. [46] at $Re = 1.2 \times 10^7$.

suggest that the flow field in the stern region is largely insensitive to Re at $x/L = 0.978$, possibly because of flow separation.

The profiles of mean (U) and axial turbulence intensity ($\overline{u^2}$) at $3D$ downstream of the stern are compared to the experiments of Jiménez et al. [47] in Figure 4.15. The wake width matches well with the experiment, whereas the centerline values are underpredicted for both U and $\overline{u^2}$. The centerline U is higher (lower centerline velocity deficit, $U_\infty - U$) and the centerline $\overline{u^2}$ is smaller than that of the experiments. The location of the peak of $\overline{u^2}$ however, agrees with the experiments. Recall that grid convergence of drag force and C_f was discussed and confirmed in §4.1.2.

Possible reasons for the mismatch are the confinement and blockage effects in the experiment as discussed earlier. The junction flows due to the semi-infinite sail distorts the axisymmetry and the confinement increases the edge velocity of the wake. Recently, Posa and Balaras [55] simulated fully-appended SUBOFF at flow conditions identical to that of Jiménez et al. [48], who reported another set of experiments conducted in the same tunnel and setup. Posa and Balaras [55] also observed similar differences between their LES results and that from the experiments. Note that the present simulations attempt to match the physical conditions (Re and the tripping location) of Jiménez et al. [47], unlike Posa and Balaras [55]. Another reason for the mismatch can be the

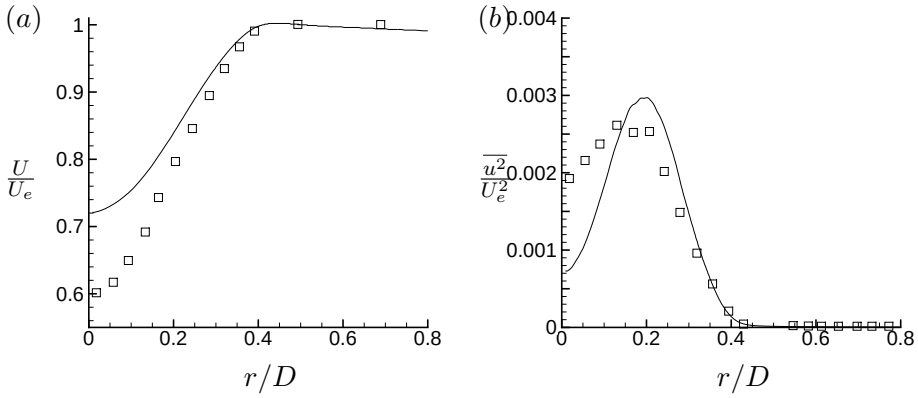

Figure 4.15: The axisymmetric wake: axial mean velocity and axial turbulent intensity normalized with edge velocity (U_e) are compared to Jiménez et al. [47] at $3D$ downstream of the hull.

difference in hull boundary layer between the experiments and the simulations. The present hull boundary layer is purely axisymmetric unlike the experiments, where the semi-infinite sail is present. In the absence of the characteristics of hull boundary layer or C_f on the hull from the experiments, it is impossible to determine whether the present hull boundary layer is identical to that in the experiments. The presence of confinement, junction flows due to the support, and the blockage due to instrumentation in the experiments (see Jiménez et al. [47] for details) can also affect the evolution and subsequent separation of the hull boundary layer to form wake.

Turbulent wakes are characterized by centerline deficit (u_0) and half-wake width (l_0).

$$u_0 = \frac{U_e - U_{r=0}}{U_e} \tag{4.2}$$

where U_e is the mean axial velocity at the edge of the wake. l_0 is defined as the radial distance from the centerline where the deficit is $u_0/2$. The evolution of u_0 and l_0 are compared to the correlations reported by Jiménez et al. [47] in Figure 4.16. The centerline deficit from LES is smaller than that of the experiment, whereas the wake width show good agreement. The wake is also shown in similarity coordinates and compared to the correlation given by Jiménez et al. [47] in Figure 4.17, showing good

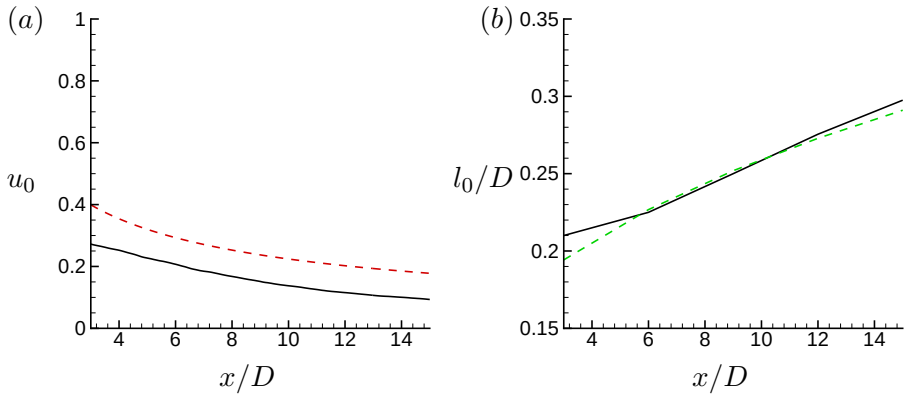

Figure 4.16: The axisymmetric wake: centerline deficit (u_0) and half wake-width (l_0). x is the distance measured from the stern. Correlations from Jiménez et al. [47] are shown for comparison.

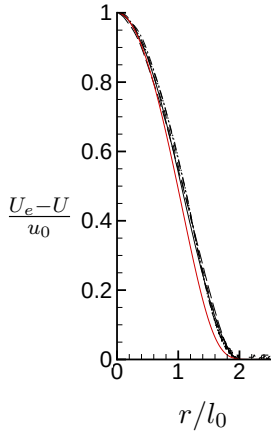

Figure 4.17: The axisymmetric wake: self-similar mean axial velocity profile compared to correlation of Jiménez et al. [47]. U_e is the velocity at the edge of the wake. Correlation from Jiménez et al. [47] is shown for comparison.

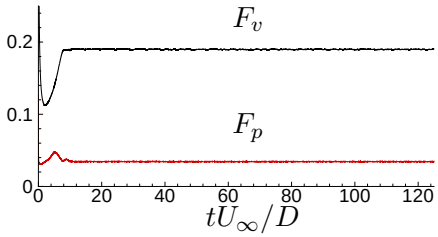

Figure 4.18: The time evolution of the drag-force contribution from pressure (F_p) and viscous forces (F_v) on the hull. Note that one flow-through time is $tU_\infty/D = 28.8$.

agreement.

4.2.3 Forces on the body

Figure 4.18 shows the time evolution of the overall pressure and viscous forces on the hull in the axial direction. These forces together yield the drag. As expected, most of the drag comes from viscous forces as the flow is largely attached. Note that the initial transients last for a small fraction of flow-through time. In the simulation domain, one flow-through time $tU_\infty/D = 28.8$. The overall drag coefficient

$$C_D = \frac{F}{0.5\rho U_\infty^2 S}, \tag{4.3}$$

where F is the drag force and $S = 0.25\pi D^2$ is the projected area. The value of C_D from LES is 0.204.

4.2.4 The mean flow field

The time-averaged flow field is further averaged in the azimuthal direction to obtain mean flow field in xr plane. Figure 4.19 shows mean axial (U) and radial (U_r) velocities in the bow region. The bow region has a strong favorable pressure gradient which is geometrically induced. The boundary layer is tripped at $x/D = 0.75$ similar to the reference experiment as mentioned earlier. The thickening of the hull boundary layer can be observed. U_r is negligible away from the bow region due to high curvature in both longitudinal and transverse directions. $\overline{uu_r}$ and TKE in the bow region are shown

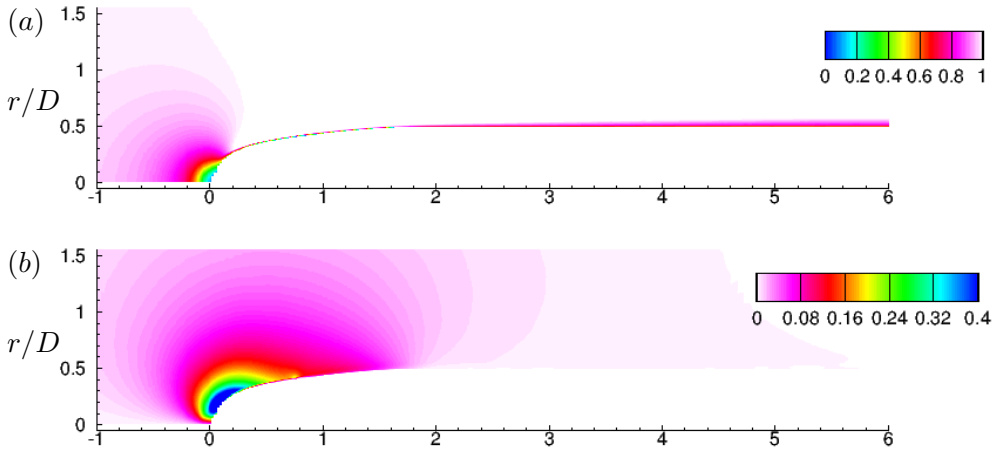

Figure 4.19: The mean flow field in bow region: axial velocity (a) and radial velocity (b) in xr plane. The boundary layer is tripped at $x/D = 0.75$.

in Figure 4.20. Due to the no-slip boundary condition, there is always a mean shear near wall. But in order to have production of turbulence, $\overline{uu_r} < 0$ is required in addition to mean shear. Tripping seems to generate that as shown in Figure 4.20(a). The boundary layer quickly transitions to turbulence, as evident from the contours of TKE (Figure 4.20b).

Figure 4.21 shows U and U_r in the stern region of the hull. The flow separates on the stern due to the adverse pressure gradient. High longitudinal and transverse curvature leads to high U_r in this region, similar to bow. Turbulent intensities and $\overline{uu_r}$ in the stern region are shown in Figure 4.22. The near-wake of the hull is dominated by the axial turbulent intensity. All the contours show local minimum and local maximum on the centerline and slightly away from the axis respectively at any given streamwise location in the wake. This behavior of turbulent quantities is referred to as bimodal nature of turbulent wake because the shape of the profiles appears to have two symmetric peaks away from the centerline in xy plane. It is consistent with the past work on SUBOFF [47, 48, 55]. The origin of this shape lies in the formation of the wake itself. The thin hull boundary layer in the ZPG region of the hull thickens rapidly in the stern region due to the adverse pressure gradient. APG is known to suppress turbulence near wall

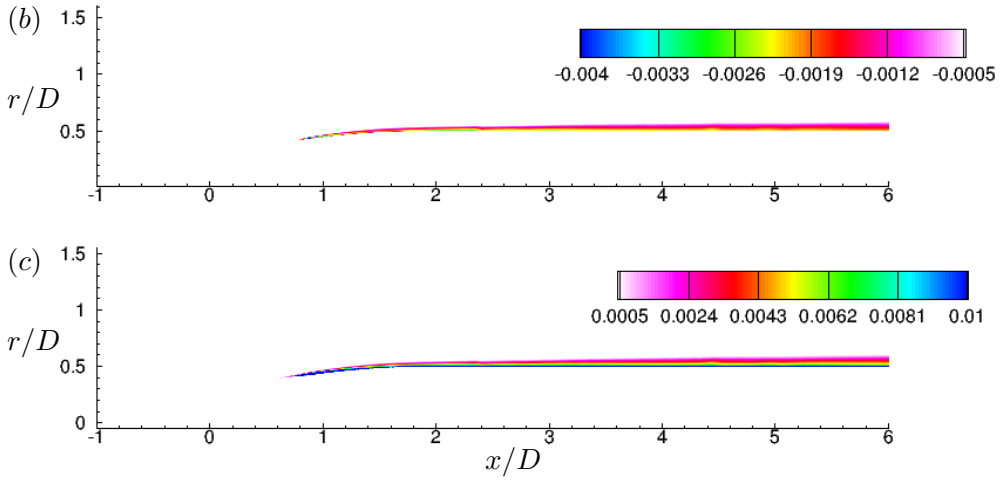

Figure 4.20: The mean flow field in bow region: Reynolds stress (a) and TKE (b) in xr plane.

as observed by Patel [23] in their experiments on turbulent boundary layer over an axisymmetric body of revolution. The thickened hull boundary layer with suppressed near-wall turbulence separates to form wake, which shows peaks at radial offset from the axis.

4.2.5 The evolution of axisymmetric wake

For a self-similar axisymmetric wake, the conservation of axial momentum yields,

$$\frac{d}{dx}\int_0^\infty U(U_\infty - U)rdr = 0$$

$$\implies \int_0^\infty U(U_\infty - U)rdr = constant = U_\infty^2\theta^2 \tag{4.4}$$

where, θ is the momentum thickness defined such that,

$$\theta^2 = \frac{1}{U_\infty^2}\int_0^\infty U(U_\infty - U)rdr. \tag{4.5}$$

As the wake evolves, θ is conserved but the centerline deficit decays and the wake-width increases. An important parameter for self-similar axisymmetric wakes is local

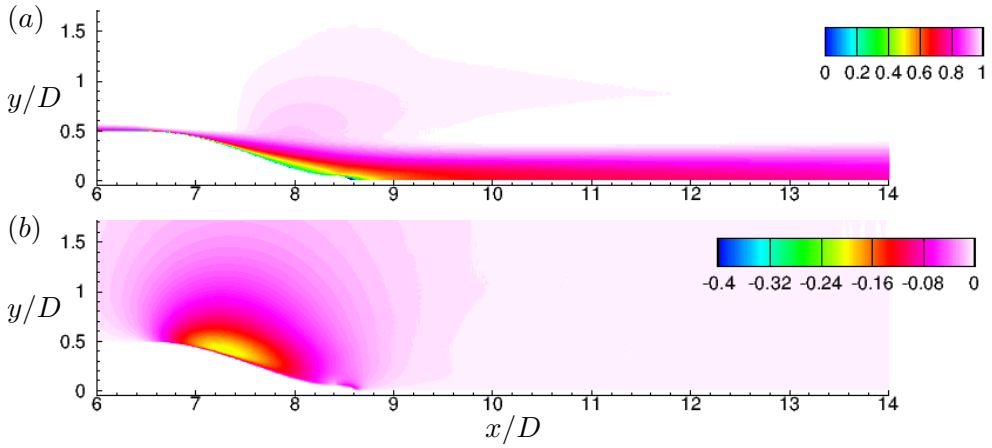

Figure 4.21: The mean flow field in stern region: axial velocity (a) and radial velocity (b) in xr plane.

Reynolds number which can be defined using u_0 as the velocity scale and an appropriate local length scale. It is convenient to choose δ_* as the local length scale, which is defined such that,

$$\delta_*^2 = \frac{1}{u_0}\int_0^\infty (U_\infty - U) r dr. \tag{4.6}$$

Note that l_0 and δ_* are related. For an axisymmetric wake, self-similarity implies,

$$\frac{U_\infty - U}{U_\infty} = u_0(x) f(r/l) \tag{4.7}$$

where, f is the shape function and l is a length scale related to wake width, which is chosen to be δ_*. Note that by definition,

$$f(r = l_0) = 1/2. \tag{4.8}$$

Numerous past studies of axisymmetric wakes [144] have shown that f is approximately Gaussian, i.e.

$$f = e^{-r^2/2\delta_*^2} \tag{4.9}$$

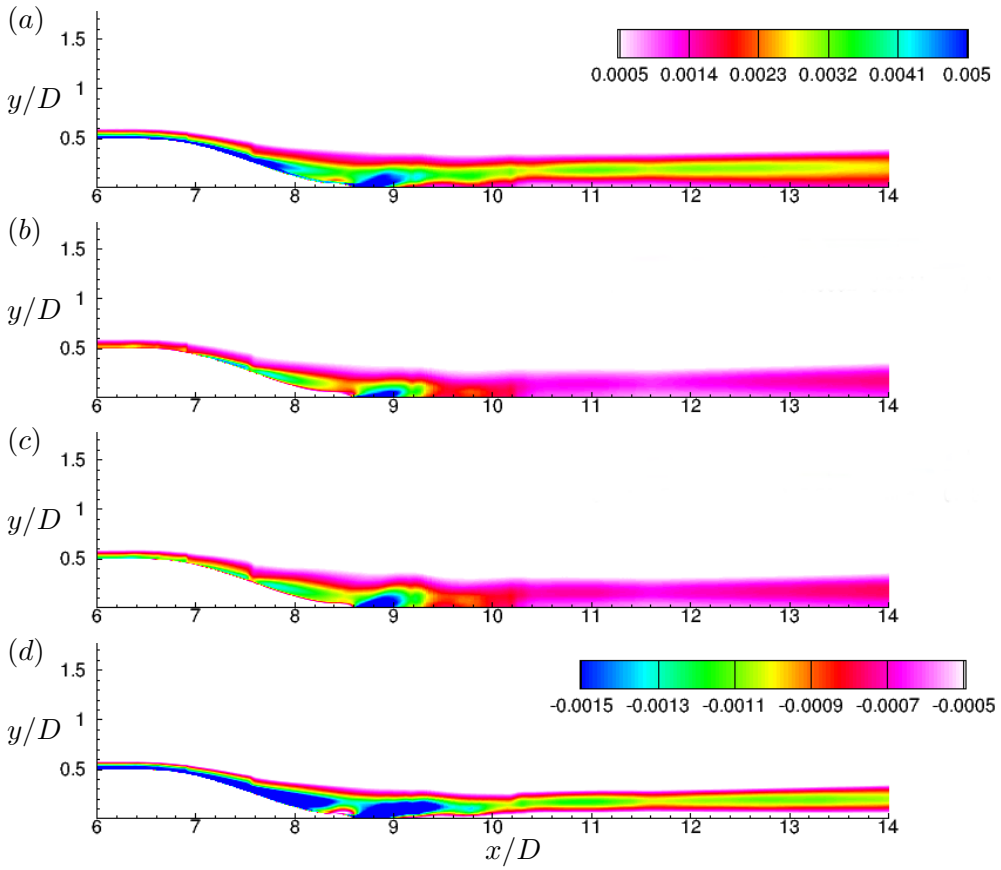

Figure 4.22: The second order velocity statistics in stern region: axial (a), radial (b) and azimuthal (c) turbulent intensities and Reynolds stress (d) in xr plane.

which yields,

$$\frac{l_0^2}{2\delta_*^2} = log2 \implies l_0 = \sqrt{2log2}\delta_*. \tag{4.10}$$

Figure 4.23 shows the axial evolution of local Reynolds number using δ_* as well as l_0. Re_{l_0} is evaluated using the correlations of Jiménez et al. [47] for u_0 and l_0. As expected, the local Reynolds number shows streamwise decay but the LES result is lower than that from the experiments. A possible reason for this is the presence of the semi-infinite sail in the experiments, which can create an additional velocity defect.

Eq. 4.6 along with Eq. 4.4 yield,

$$\begin{aligned} u_0\delta_*^2 &= U_\infty\theta^2 \\ \implies \frac{\delta_*}{\theta} &= \sqrt{\frac{U_\infty}{u_0}} \end{aligned} \tag{4.11}$$

Johansson et al. [145] proposed and validated two different self-similar solutions for axisymmetric wakes, namely the high-Re ($\delta_* \sim x^{1/3}$) and low-Re ($\delta_* \sim x^{1/2}$) solutions. Figure 4.24 shows the streamwise evolution of δ_*/θ, which is related to u_0 from Eq. 4.11. The present result is compared to the two self-similar solutions. The curves,

$$\frac{\delta_*}{\theta} = \begin{cases} 1.17\left(\frac{x+x_0}{D}\right)^{1/3}; & x/D \leq 2 \\ 0.78\left(\frac{x+x_0}{D}\right)^{1/2}; & x/D \geq 5 \end{cases} \tag{4.12}$$

show good fit for the present simulated result. Interestingly, the present solution transitions from high-Re to low-Re similarity solutions between $2 < x/D < 5$. To the best of our knowledge, this is the first study showing both high-Re and low-Re similarity solutions for a streamlined body. Note that the virtual origin, $x_0/D = 2.08$ is same as that of Jiménez et al. [47]. This difference in the wake behavior between the present simulations and the experiments can be attributed to the higher local Reynolds number in the presence of semi-infinite sail.

It is interesting to note that past studies on a variety of bluff bodies have reported

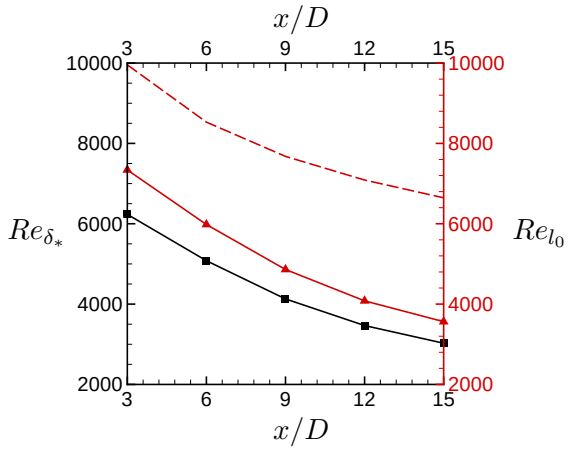

Figure 4.23: Evolution of local Reynolds number in the wake. Both $Re_{\delta_*} = \frac{u_0 \delta_*}{\nu}$ and $Re_{l_0} = \frac{u_0 l_0}{\nu}$ are shown and compared to Re_{l_0} evaluated using the correlations of Jiménez et al. [47] for u_0 and l_0 (dashed lines).

various location for transition from high-Re to low-Re self-similarity solution for turbulent axisymmetric wakes depending on the wake generators (see Johansson and George [146] and the references therein). For the present streamlined wake generator, this transition seems to be complete at $x/D = 5$, which corresponds to $Re_{\delta_*} \approx 5465$ (Figure 4.23).

Profiles of U and C_p are extracted at various streamwise locations from $3D$ to $15D$ downstream of the hull as shown in Figure 4.25. Slow expansion of the axisymmetric wake and the diffusion of the shear layer at the edge of the wake is evident in the profiles of U as we go downstream in the wake. C_p is small at all locations, however there is a small radial gradient, which decreases moving downstream.

Profiles of turbulent intensities and Reynolds stress are shown in Figure 4.26 in both physical (a-d) and similarity (e-h) coordinates at the same streamwise locations as those of Figure 4.25. The peak of the axial turbulent intensity decreases monotonically going downstream whereas, there is a slight increase in radial and azimuthal turbulent intensities from $3D$ to $6D$, followed by decrease till last location. The peaks of all the profiles drift radially outward due to slow radial spreading of the turbulent wake. The same quantities in similarity coordinates do not show any such drift i.e. the peaks at all

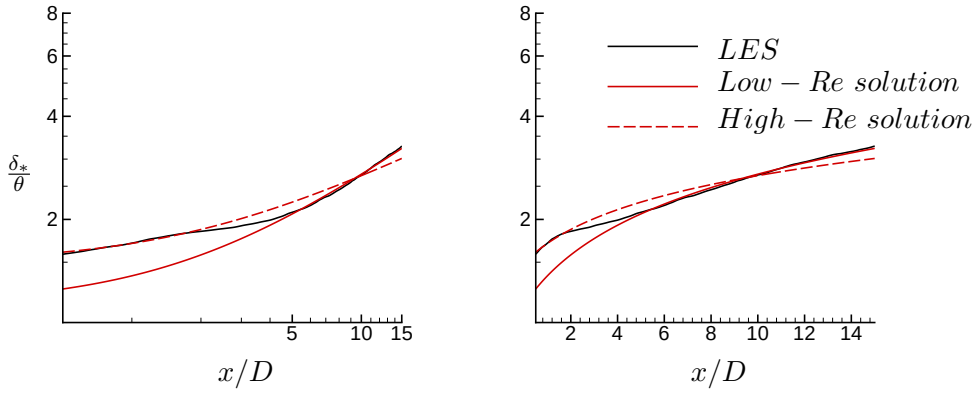

Figure 4.24: Axial evolution of δ_*/θ compared to the similarity laws proposed for axisymmetric wakes in log-log (a) and log-linear (b) axes. Both low-Re ($\sim x^{1/2}$) and high-Re ($\sim x^{1/3}$) similarity solutions are shown.

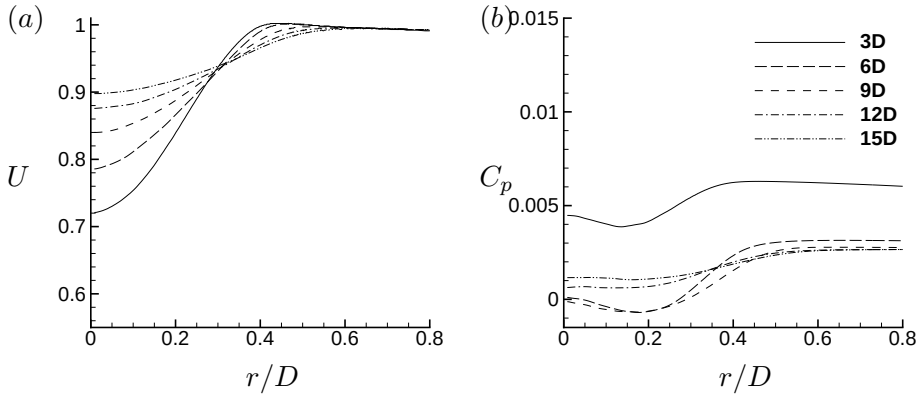

Figure 4.25: The axisymmetric wake: (a) U and (b) C_p at 3, 6, 9, 12 and 15 diameters downstream of the stern.

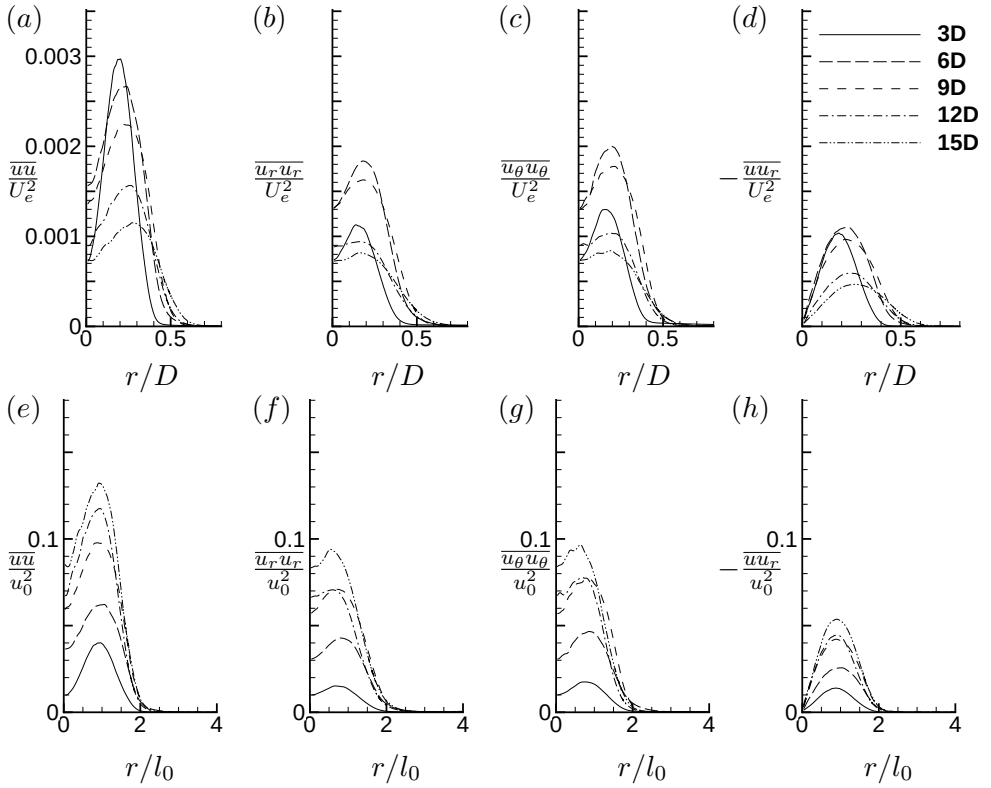

Figure 4.26: The axisymmetric wake: (a) $\overline{uu}$, (b) $\overline{u_r u_r}$, (c) $\overline{u_\theta u_\theta}$ and (d) $\overline{uu_r}$ at 3, 6, 9, 12 and 15 diameters downstream of the stern in physical (a-d) and similarity coordinates (e-h). U_e and $u0$ are edge velocity and centerline deficit respectively.

the locations in the wake is located at $r/l_0 = 1$, identical to the observations of Jiménez et al. [47]. Note that the peak value of all the quantities increases monotonically moving downstream in the wake despite a streamwise decrease in their magnitude (Figure 4.26e-h) because of rapid streamwise decay of the centerline deficit (u_0). In other words, u_0^2 decreases more rapidly as compared to turbulent intensities and Reynolds stress as we move downstream in the wake. Consistent with the previous studies reported in the literature for this geometry, there is no sign of self-similarity in the second-order velocity statistics over the length of the simulated domain.

Mean radial velocities are often neglected in the studies of free shear flows, but they are important quantities when near-field and entrainment effects are important. The transient length needed to achieve self-similarity also depends on entrainment for

shear flows as demonstrated by Babu and Mahesh [147] for both laminar and turbulent round jets. Profiles of mean radial velocity (U_r) are shown in Figure 4.27(a). U_r is small and negative at all the locations shown and the peaks occur at $r/l_0 = 1$. Note that the profiles are not symmetric about $r/l_0 = 1$ and U_r does not go to zero at the edge of the wake. In fact, it is negative and higher in magnitude closer to the hull due to entrainment caused by the separation of the hull boundary layer on the stern. This phenomenon of entrainment by separated shear layers has been studied in the past (see Stella et al. [59] and references therein). It can be shown that $V_s = u_0 \frac{dl_0}{dx}$ is an appropriate scale for U_r as follows.

For an axisymmetric wake, the mean continuity equation is

$$r^* \frac{\partial U^*}{\partial x^*} + \frac{\partial (U_r^* r^*)}{\partial r^*} = 0 \tag{4.13}$$

where, $*$ denotes dimensional quantities. Normalizing with suitable scales for U, U_r and r, which are U_s, V_s and a transverse length scale δ respectively and using chain rule yields,

$$\left(- \frac{U_s}{V_s} \frac{d\delta}{dx^*} \right) r \frac{\partial U}{\partial r} + \frac{\partial (U_r r)}{\partial r} = 0. \tag{4.14}$$

The term in () should be of order 1. The appropriate scale for U is maximum velocity defect, i.e. $U_s = u_0$. The half-wake width (l_0) can be taken as a transverse length scale. Thus,

$$V_s \sim u_0 \frac{dl_0}{dx}. \tag{4.15}$$

Scaling the profiles of U_r with V_s shows a reasonable collapse beyond $9D$, as shown in Figure 4.27(b).

Energy spectra of the streamwise velocity at centerline are shown in Figure 4.28. Note that, there is no sign of coherent shedding (see Figure 4.28b), usually observed for bluff bodies at high Re, consistent with the observations of Jiménez et al. [47] at the present Re.

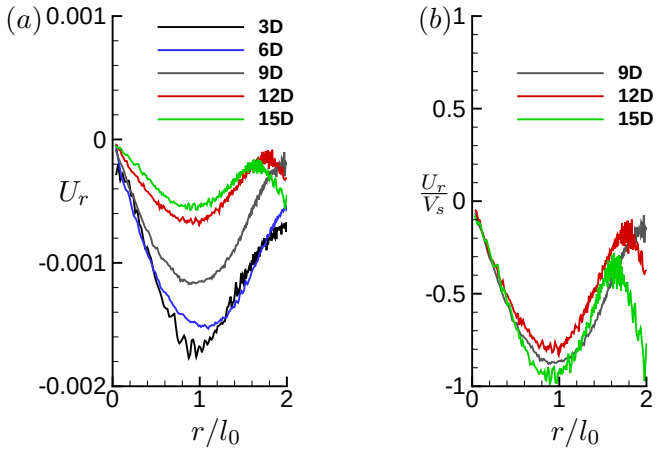

Figure 4.27: The axisymmetric wake: U_r at 3, 6, 9, 12 and 15 diameters (a) U_r scaled with V_s beyond 9 diameters (b) downstream of the stern . $V_s = u_0 \frac{dl_0}{dx}$ is the mean radial velocity scale.

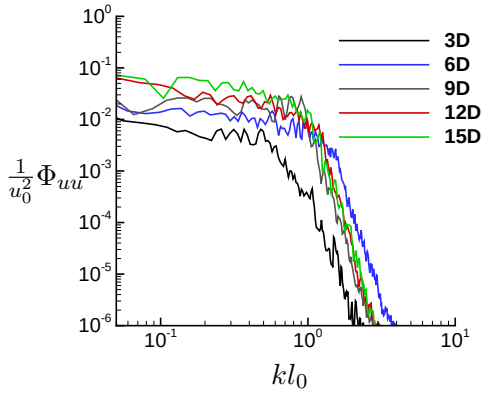

Figure 4.28: Energy spectra of streamwise velocity component at centerline ($r/l_0 = 0$) in the wake at 3, 6, 9, 12 and 15 diameters downstream of the stern.

4.3 Summary

Wall-resolved LES is used to simulate flow over axisymmetric hull (SUBOFF without appendages) at $Re = 1.1 \times 10^6$ at zero angle of pitch and yaw. The length of the computational domain and the level of grid resolution are significantly higher than most past work and chosen to capture axisymmetric wake up to fifteen diameters downstream of the body without any confinement effect. Grid convergence studies have been performed to ensure grid independent numerical solution. LES results for the flow field on the hull are compared to the experimental data of Huang et al. [46] for C_p, C_f and the mean velocity and pressure profiles on the stern. C_p and scaled C_f show good agreement with the experiment and the mean velocity and pressure profiles show similar trend. The axisymmetric wake of the hull is compared to the experiments of Jiménez et al. [47], showing good agreement with the wake width but smaller centerline deficit, probably due to blockage and confinement effects in the experimental setup.

The hull boundary layer and the wake of the hull are discussed in detail. The boundary layer turns turbulent following tripping and evolves until its separation on the stern to form wake. Comparisons of the axisymmetric TBL with planar TBL for first and second order velocity statistics show that very close to the surface, both are similar. However, away from the surface, TKE and Reynolds stress in axisymmetric TBL decay much rapidly as compared to that of planar TBL. This appears to be the effect of curvature, which tend to suppress long structures of the log region of the TBL. The axisymmetric wake shows self-similarity in mean streamwise velocity but not in turbulent intensities, even up to fifteen diameters downstream of the hull. The peaks of turbulent intensities and Reynolds stress in similarity coordinates are located at half-wake width away from the axis at all the streamwise locations. All these observations are consistent with the past studies. The profiles of mean radial velocity and Reynolds stress show reasonable collapse, mainly in the far wake when scaled with appropriate scales. The present simulations show that as the wake evolves downstream, it transitions from high-Re to low-Re similarity solution, as theoretically proposed by Johansson et al. [145].

Chapter 5

Dependence of the stern flow and wake on hull boundary layer

In this chapter, wall-resolved LES is used to study the dependence of the stern flow and axisymmetric wake on the hull boundary layer. The goal is to understand the effect of θ/a and Re_θ of the hull boundary layer on the flow separation and the wake. The simulation details are described in Section 5.1. The generation of turbulent inflow is discussed in Section 5.2. Results are discussed in Section 5.3. The chapter is summarized in Section 5.4.

5.1 Simulation details

5.1.1 Problem setup

The hull has length, $L = 14.29'$ and maximum diameter, $D = 1.667'$ [5]. In this chapter, only the aft portion of the hull is simulated such that the inflow is located $0.56L$ downstream from the nose of the hull, which is used as the origin of the reference coordinate system. Note that the length of the hull is $L = 8.6D$. The computational domain used for the present simulations is shown in Figure 5.1. The cylindrical domain has a radius $6D$ and a length $13.2D$. The radial extent of the domain is larger than that used by Posa and Balaras [55] for their LES of fully-appended SUBOFF at $Re =$

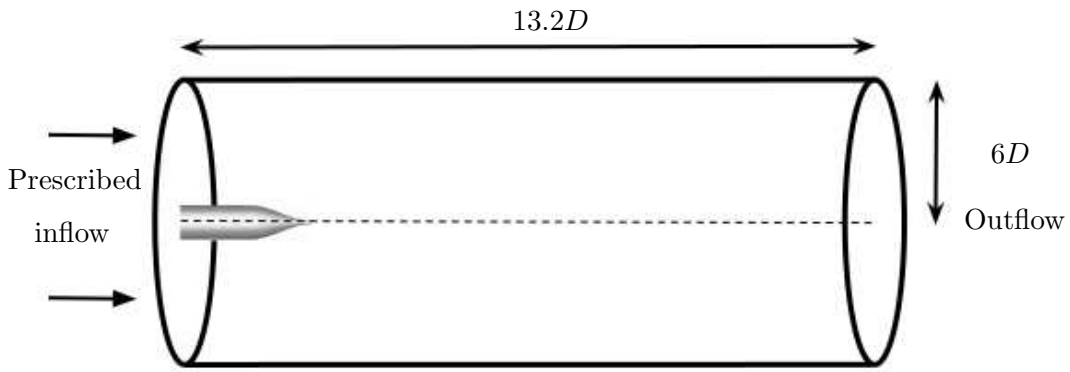

Figure 5.1: The computational domain for the stern simulations.

1.2×10^6, based on length of hull and freestream velocity. They reported that the hull boundary layer grows from $Re_\theta \sim 1000$ at $x/L = 0.2$ to $Re_\theta \sim 2200$ at $x/L = 0.7$ on the fully-appended hull. At $x/L = 0.56$, they reported $Re_\theta = 2000$ approximately. Thus, the inflow of the present domain is chosen to have the same nominal Re_θ. It should be noted however, that their hull boundary layer may have influence of appendages, which creates junction flows. Any such effect is absent in the present simulations.

No-slip boundary conditions are applied to the surface of the body. The radial and outflow boundaries are prescribed with freestream and convective boundary conditions respectively. An axisymmetric TBL with desired characteristics is prescribed at the inflow. The details of turbulent inflow generation and validation are briefly described in Section 5.2. The computational grid used in the present simulations is unstructured and composed of approximately 282 million hexahedral control volumes. A typical transverse cross-section on the hull and the wake has 1600 cells in the azimuthal direction. The grid is clustered close to the hull with a minimum wall-normal spacing of $0.0003D$, where D is the hull diameter. A nominal growth ratio of 1.01 is used to transition from fine to coarser resolution away from the hull in both wall-normal direction on the body and axial direction in the wake. The entire grid is partitioned over 2880 processors and all the simulations are performed with the same grid and time step of $\Delta t U_\infty / D = 0.0012$. The instantaneous flow field is sampled every ten time step to compute statistics, once

Case	$Re_{\theta,inflow}$	θ_{inflow}/a	Δx^+, Δr^+, $a^+\Delta\theta$
$S2000_{base}$	2000	0.078	$10.31 \times 0.68 \times 4.5$
$S2000_{thick}$	2000	0.097	$8.25 \times 0.55 \times 3.6$
$S1600_{base}$	1600	0.078	$8.26 \times 0.55 \times 3.6$

Table 5.1: Details of the computational domain and the grid used for the main simulations. The friction velocity, $u_\tau = 0.044$ is used as a reference to calculate grid resolution in wall units.

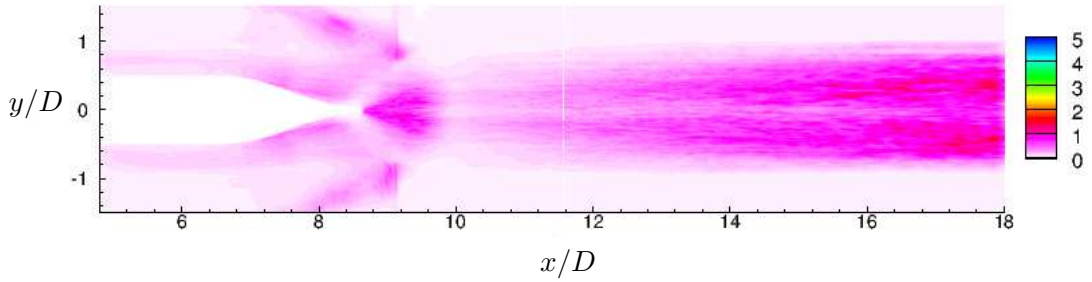

Figure 5.2: The time-averaged eddy viscosity normalized with the molecular viscosity in xy plane.

the initial transients wash out of the domain.

Simulations of flow over the stern portion of the hull are performed using the same computational grid for all the simulation cases. Details of the prescribed axisymmetric TBL and the corresponding grid resolution at a representative location in the region where the flow is attached, are listed in Table 5.1.1. Note that the grid used for the main simulations has approximately four and eight times finer axial and azimuthal resolutions respectively, than that of the corresponding auxiliary simulation. Phase-averaged eddy viscosity normalized with the molecular viscosity is shown in Figure 5.2 for the baseline case ($S2000_{base}$). The magnitude of eddy viscosity is small in the near wall, suggesting that the grid resolution is adequate.

5.2 Turbulent inflow generation

The recycle-rescale method is used to generate turbulent inflow in a series of auxiliary simulations of axial flow over a circular cylinder with diameter identical to that of the

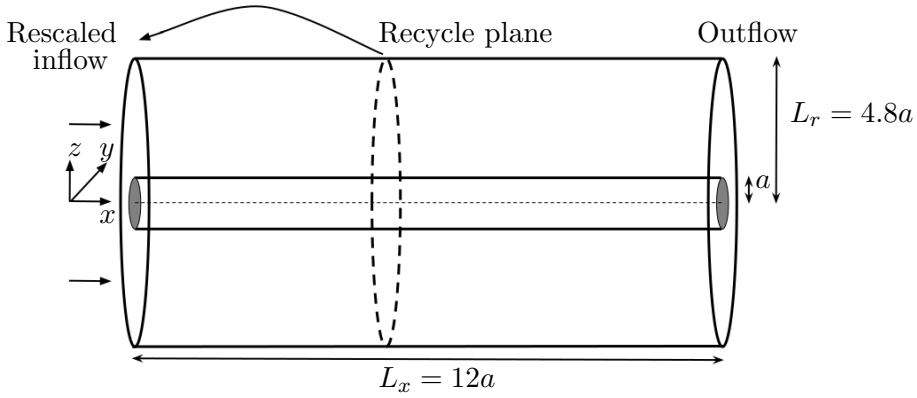

Figure 5.3: The computational domain for auxiliary simulations for generating turbulent inflow.

Case	L_x/a, L_r/a, L_θ	N_x, N_r, N_θ	Δx^+, Δr^+, $a^+\Delta\theta$
$A2000_{base}$	$36 \times 4.8 \times 2\pi$	$1000 \times 200 \times 200$	$41.25 \times 0.68 \times 36$
$A2000_{thick}$	$36 \times 4.8 \times 2\pi$	$1000 \times 200 \times 200$	$33 \times 0.55 \times 28.8$
$A1600_{base}$	$12 \times 4.8 \times 2\pi$	$400 \times 200 \times 200$	$27.5 \times 0.55 \times 28.8$

Table 5.2: Details of the computational domain and the grid used for the auxiliary simulations. The friction velocity, $u_\tau = 0.044$ is used a reference to calculate grid resolution in wall units.

hull, using the LES algorithm and the recycle-rescale methodology described in Chapter 2. Once the flow field reaches statistical convergence, the time series of the velocity field at the desired axial location is stored and subsequently used as inflow to the main simulation.

The computational domain used for the auxiliary simulations is an annular region between two coaxial cylindrical surfaces, with outer and inner radii, $L_r = 4.8a$ and a respectively, where $a = 0.8335$ is the radius of the hull, as shown in Figure 5.3. The recycle plane is located at $9.9a$ downstream of the inflow for all the cases. The details of the computational domain and grid resolution for each auxiliary simulation are listed in Table 5.2. In order to minimize the computational cost of the inflow generation, only large scales are resolved in the auxiliary simulations. The details of the auxiliary simulations are listed in Table 5.2.

Case	$Re_{\theta,in}$	θ_{in}/a	Re_a	Re_θ	$Re_{\theta,plane}$	θ_{plane}/a
$A2000_{base}$	1250	0.048	26047	1250-2298	2000	0.078
$A2000_{thick}$	1500	0.072	20837	1500-2320	2000	0.097
$A1600_{base}$	1500	0.072	20837	1500-1710	1600	0.078

Table 5.3: Simulation parameters for auxiliary simulations. $Re_{\theta,in}$ and θ_{in}/a are the values prescribed at the inflow of the auxiliary simulations. Re_a is the radius based Reynolds number. $Re_{\theta,plane}$ is the Re based on momentum thickness at that plane (θ_{plane}).

The first and second order statistics of the velocity field at the planes which are extracted and used as inflow for the main simulations are shown in Figure 5.4, for all the cases listed in Table 5.2. In the absence of other relevant data, the planar boundary layer profile at $Re_\theta = 1968$ [133] is shown for qualitative comparison. The mean velocity profiles show good qualitative agreement with the planar boundary layer and a distinct logarithmic layer can be observed for all the cases. The higher value of skin-friction and hence smaller edge velocity in wall units for axisymmetric TBL is observed, which is consistent with the experimental observations reported in the literature [10] and analytically shown in Chapter 3. Note that the rms of velocity fluctuations and Reynolds stress are shown in cylindrical components (axial, radial and azimuthal), whereas that of the planar boundary layer are shown in Cartesian components.

5.3 Results

5.3.1 Overview of the flow field

The general features of the flow field (which are similar for other cases as well) are discussed for the base case ($S2000_{base}$). The instantaneous near-wall flow structures are visualized in Figure 5.5 using isocontour of Q-criterion [141] colored with axial velocity. The fine near-wall structures appear to be adequately resolved. Contours of instantaneous axial velocity, vorticity magnitude and pressure field are shown in Figure 5.6. As mentioned earlier, the inflow is located at $0.56L$ ($= 4.82D$) downstream from the nose of the hull. The flow is initially attached, as expected for a streamlined body.

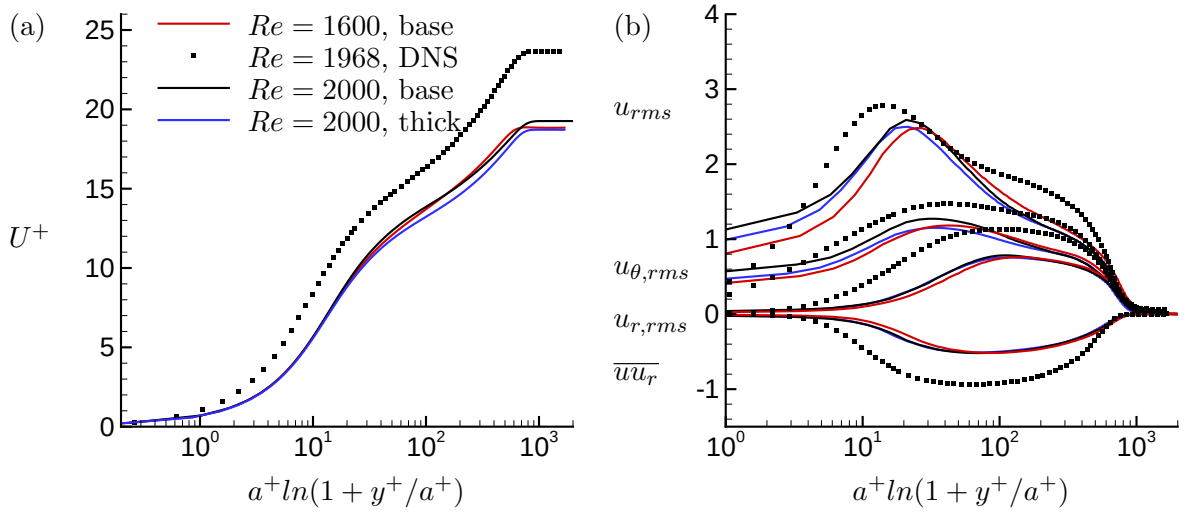

Figure 5.4: Mean (a) and second order (b) velocity statistics for the generated turbulent inflow to be used for the main simulations. DNS results of Jiménez et al. [133] for planar turbulent boundary layer at $Re_\theta = 1968$ are also shown for comparison. The usual abscissa y^+ is modified to $a^+log(1 + y^+/a^+)$ in order to account for small curvature as suggested by Afzal and Narasimha [29]. Note that DNS data show the velocity fluctuations in Cartesian components (u_{rms}, v_{rms}, w_{rms} and $\overline{uv}$) whereas the present results show the same for cylindrical components (u_{rms}, $u_{r,rms}$, $u_{\theta,rms}$ and $\overline{uu_r}$) in (b).

Figure 5.5: The coherent structures are visualized using the isocontour of Q-criterion [141] colored with axial velocity. The flow is from left to right.

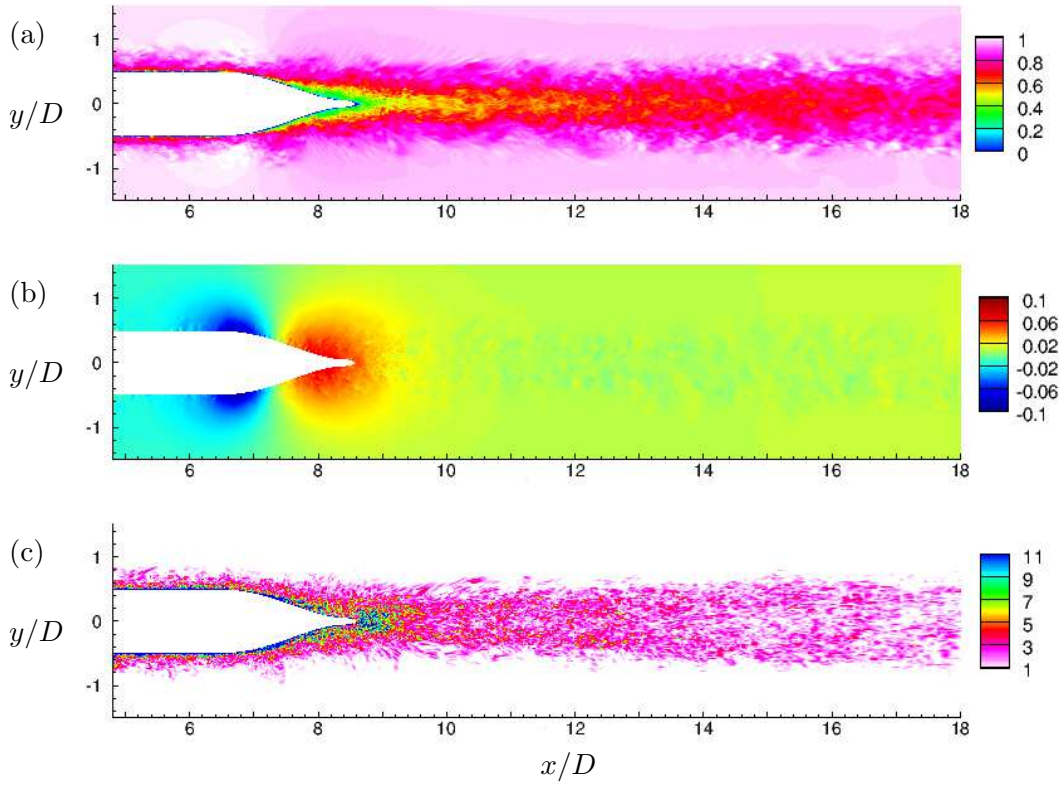

Figure 5.6: The instantaneous flow field: axial velocity (a), pressure (b) and vorticity magnitude (c) in xy plane.

The boundary layer grows rapidly in the presence of geometrically induced adverse pressure gradient and eventually separates to form wake. The slow radial spreading of the wake with increasing streamwise distance is also noticeable. The pressure gradient is negligible near the inflow but becomes adverse beyond $x/D = 6$ as evident in Figure 5.6(b). The pressure field shows small fluctuations in the wake region away from the hull. The regions of intense turbulent activity can be observed looking at the vorticity magnitude (Figure 5.6c), which are mainly the hull boundary layer and the wake. The vorticity magnitude decreases moving downstream in the wake.

The instantaneous axial velocity and vorticity magnitude are shown at a representative streamwise location on the body ($x = 5.4D$) where the flow is attached, and in the wake ($6D$ downstream of the body) where the pressure gradient is negligible, in Figures

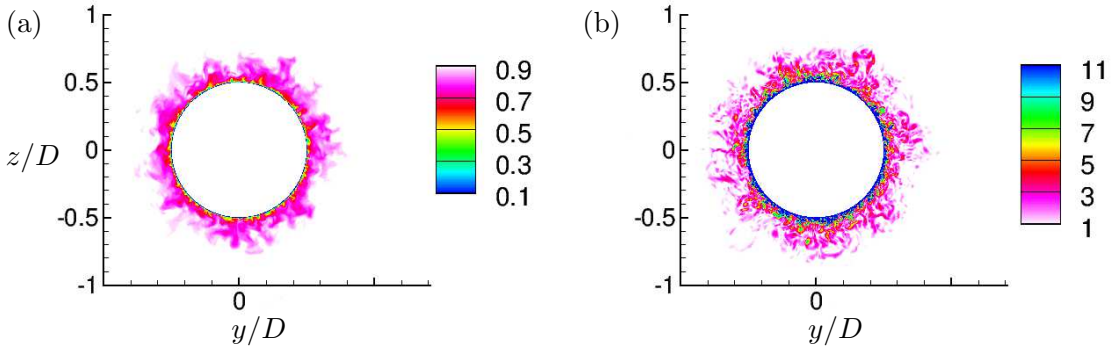

Figure 5.7: The instantaneous flow field: axial velocity (a) and vorticity magnitude (b) in the yz plane at $x = 5.4D$ on the hull.

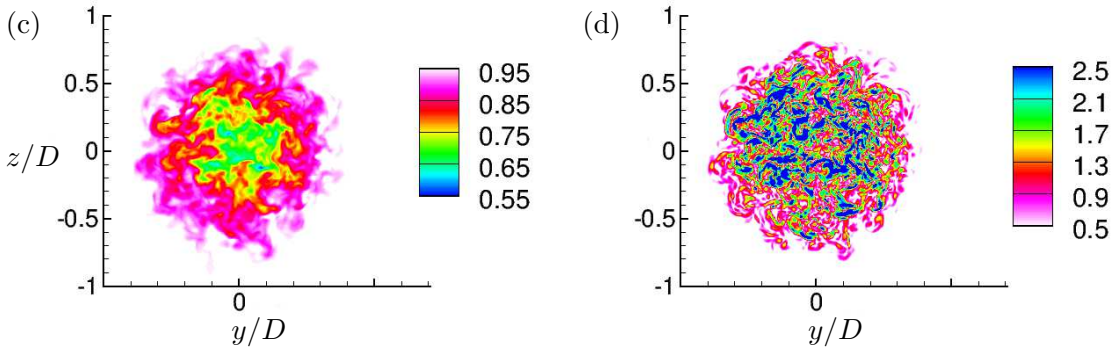

Figure 5.8: The instantaneous flow field: axial velocity (a) and vorticity magnitude (b) in the yz plane in the wake at $6D$ downstream of the hull.

5.7 and 5.8 respectively. A large range of scales can be observed in both the boundary layer, as well as the wake.

The time-averaged flow field is further averaged in the azimuthal direction to compute mean and second-order statistics in cylindrical (axial, radial and azimuthal) components. The mean axial (U) and radial (U_r) velocity and mean pressure are shown in Figure 5.9. Note that the mean azimuthal (swirl) velocity is negligible, and is hence not shown here. U is much larger than U_r away from the hull. The region where flow separates on the stern has a small U_r. The mean pressure gradient is negligible away from the body.

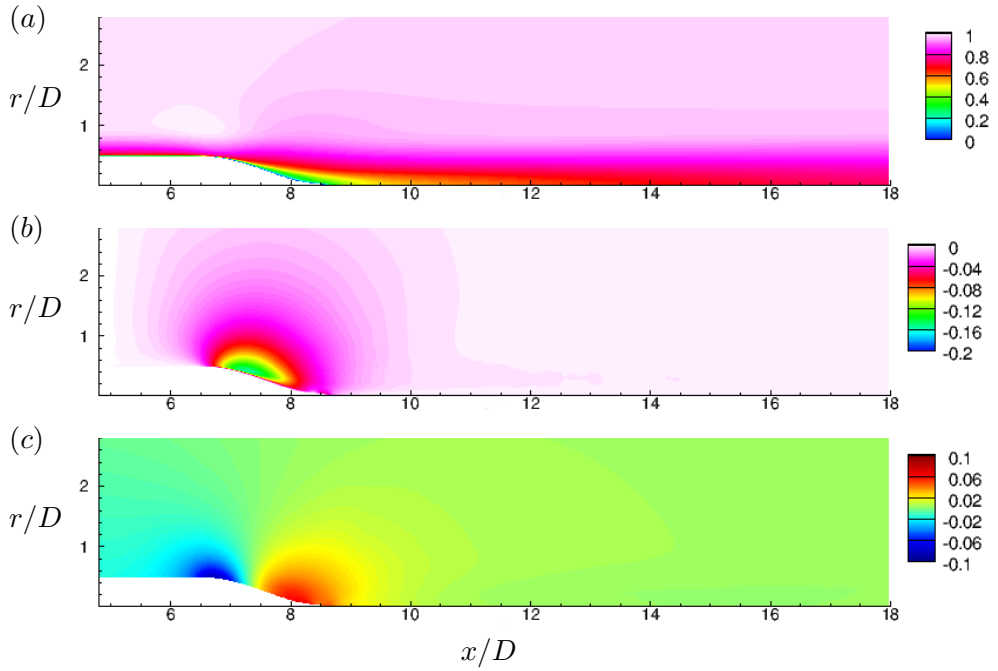

Figure 5.9: The mean velocity in stern region: axial (a) and radial (b) and pressure field (c) in xr plane.

Turbulent intensities ($\overline{u^2}$, $\overline{u_r^2}$, $\overline{u_\theta^2}$) and Reynolds stress (-$\overline{uu_r}$) are shown in Figure 5.10. The axial component of turbulent intensity dominates away from the body, whereas it is comparable to other components in the flow separation region. The flow separation region also has large -$\overline{uu_r}$. The peak of $-\overline{uu_r}$ offsets with the axis in the wake due to flow separation. This bi-modal nature i.e. dual peaks in xy plane was observed in past experiments [47, 48] and LES [55] of flow over SUBOFF.

Although the wake is turbulent, the flow outside the wake is unperturbed and essentially irrotational. The interface between these two regions is termed turbulent/non-turbulent interface (TNTI), and has been widely studied for a variety of canonical shear flows such as wakes [148], jets [149] and boundary layers [150]. The thickness of TNTI scales with the viscous scale as shown by Chauhan et al. [151] for boundary layers and was found to be 0.07 times half-wake width in the far wake at a local Reynolds number $Re = 2000$, based on centerline deficit and half-wake width by Bisset et al. [148]. The magnitude of vorticity decreases very rapidly across the TNTI. Figure 5.11 shows the

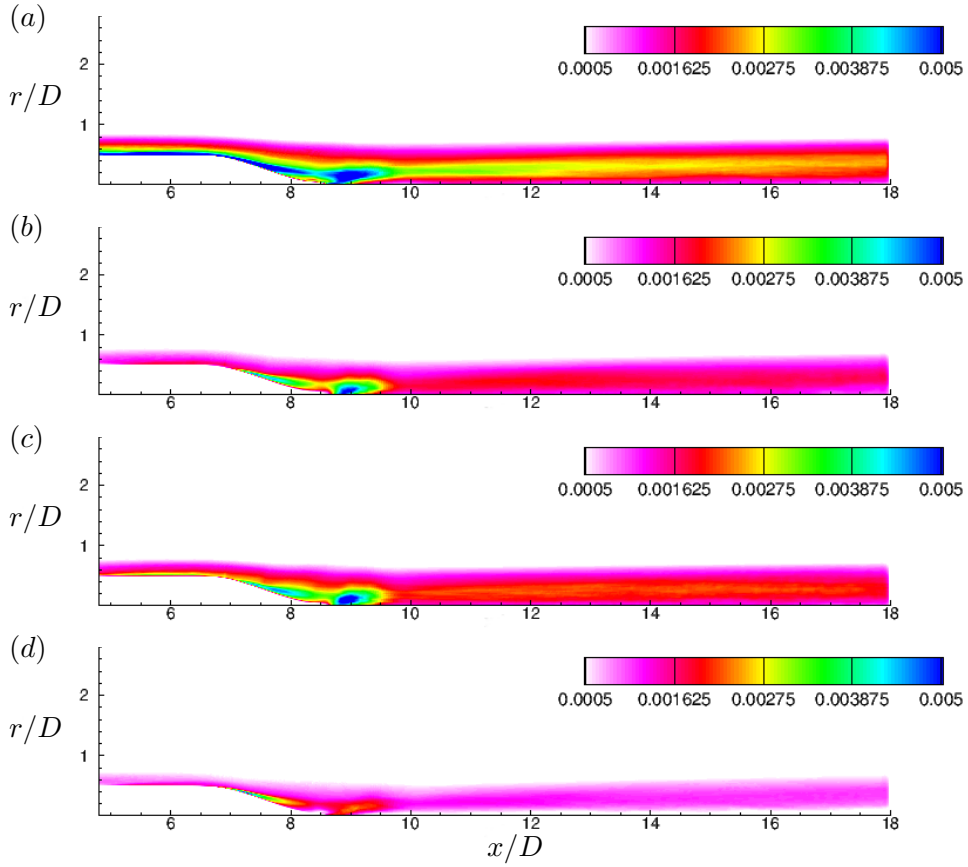

Figure 5.10: The second order velocity statistics: axial (a), radial (b) and azimuthal (c) turbulent intensities and Reynolds stress (d) in xr plane.

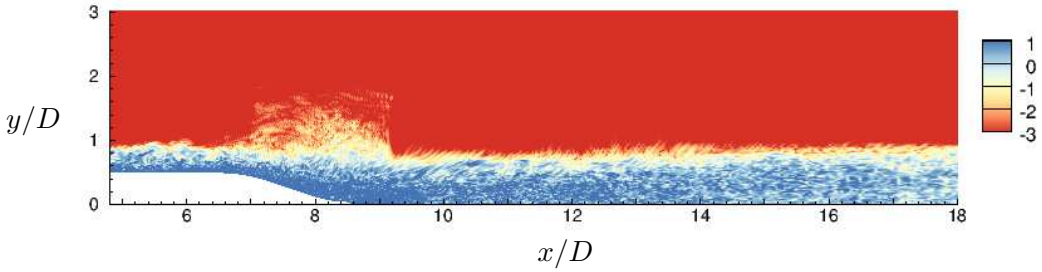

Figure 5.11: The instantaneous turbulent/non-turbulent interface (TNTI) visualized using contours of $ln(\omega)$.

contours of logarithm of vorticity magnitude, to highlight the TNTI. Note that the grid needs a very fine resolution to capture the TNTI width appropriately, which is not attempted here and only a qualitative picture is sought. The TNTI expands in the stern region where flow separates and eventually settles into that for an axisymmetric wake. The region of thicker TNTI is coincident with the region of larger U_r and hence larger entrainment region. Stella et al. [59] suggested that the large-scale entrainment depends on the incoming boundary layer properties, which will be discussed in subsequent sections of this chapter.

In rest of this chapter, the experimental results of Huang et al. [46] are used for comparison wherever possible. Huang et al. [46] reported pressure and skin-friction on the hull at $Re = 1.2 \times 10^7$, based on hull length and freestream velocity. They corrected pressure for confinement effects and also reported profiles of velocity and pressure statistics on the stern at several locations. Note that they did not report the characteristics of the boundary layer in their experiment. Hence, the comparisons presented in this chapter with their data are intended to be qualitative.

5.3.2 Pressure and skin-friction coefficients on the body

Figure 5.12 shows C_p and C_f for all the cases along with the measurements reported by Huang et al. [46]. C_p is insensitive to Re for high Re attached flows but C_f depends on Re. C_p remain largely insensitive to the inflow prescribed to the stern. It shows good agreement with the experiments up to $x/L = 0.7$. However, the subsequent drop and rise in C_p are underpredicted compared to the experiments. A possible reason for this is early separation of the boundary layer on the body due to lower Re compared to the experiments. The drop and rise in C_p around $x/L = 0.8$ and 0.9 respectively is also sensitive to the boundary layer thickness. It appears that making the boundary layer even thinner while maintaining same Re will cause the C_p to be closer to the experiments.

C_f on the other hand, is more sensitive to the characteristic of the inflow. Both Re and boundary layer thickness have an effect on the C_f unlike that of C_p, where only thickness has an effect. All the simulated cases have higher C_f than the experiment

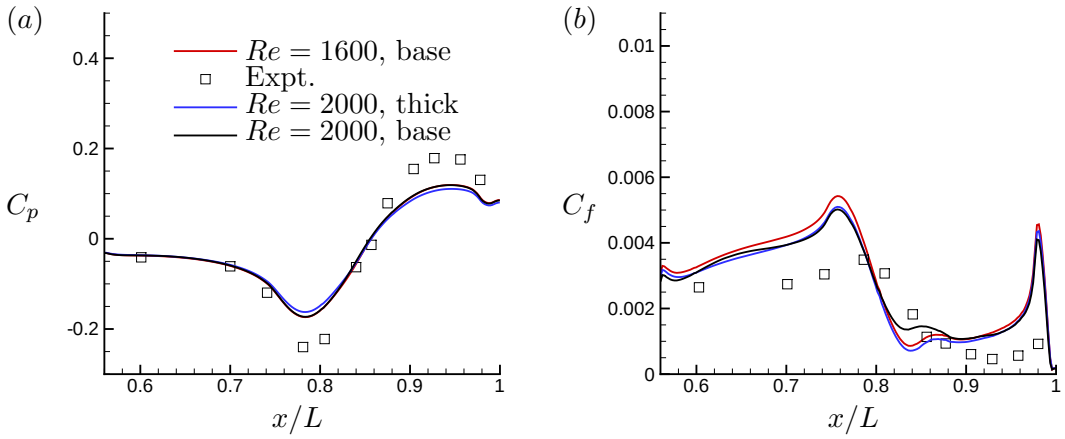

Figure 5.12: The axial evolution of pressure (C_p) (a) and skin-friction (C_f) (b) coefficients on the stern. Symbols are measurements of Huang et al. [46] at $Re = 1.2 \times 10^7$.

because of higher value of Re in the experiment. There is an initial drop in C_f until $x/L = 0.58$ and then the values increase gradually until $x/L = 0.75$ for all the cases. The length between inflow and $x/L = 0.58$ is $0.34a$, which is equal to $4.4\theta_{in}$ for the base thickness cases. This adaptation length is not numerical, but a regular feature of simulations using a prescribed turbulent inflow as observed in the literature [133, 135, 152]. Note that the $S1600_{base}$ case has higher value of C_f until $x/L = 0.8$. All the inflow cases have same C_f beyond $x/L = 0.9$.

5.3.3 Dependence of the stern flow field on axisymmetric TBL characteristics

The flow separates on the stern and the location of separation is sensitive to the incoming boundary layer. Figure 5.13 shows the mean velocity profiles extracted at $x/L = 0.904$ and 0.978 on the hull. These stations on the stern are chosen because of the availability of data from the experiments [46]. Both axial (U) and radial (U_r) velocities are shown. U_r is small and relatively insensitive to the TBL characteristics. U appears more sensitive to incoming TBL thickness than that to Re_θ.

At the same locations, profiles of rms of velocity fluctuations (u_{rms}, $u_{r,rms}$ and

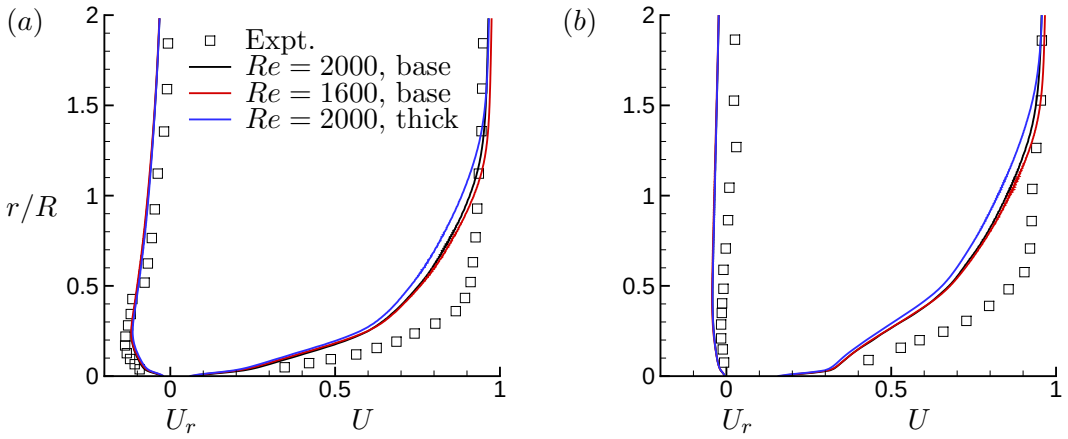

Figure 5.13: Profiles of mean axial (U) and radial (U_r) velocity at $x/L = 0.904$ (a) and 0.978 (b). Symbols are measurements of [46] at $Re = 1.2 \times 10^7$.

$u_{\theta,rms}$) and Reynolds stress ($-\overline{uu_r}$) are shown along with the experimental data in Figures 5.14 and 5.15 respectively. All these quantities show a displacement and spreading away from the axis moving downstream from $x/L = 0.904$ to 0.978. This behavior is consistent with past work on this geometry [47, 48, 55]. At both locations, the magnitude of velocity fluctuations are comparable for all components. Keeping the same thickness, the lower Re case ($S1600_{base}$) has higher velocity fluctuations than the base case ($S2000_{base}$). This is possibly a consequence of early flow separation on the stern. On the other hand, a thicker TBL at base Re has higher fluctuations mainly in the outer part of the boundary layer compared to other cases. In general, $-\overline{uu_r}$ shows similar trend as that of velocity fluctuations at both the locations. However, the magnitude of $-\overline{uu_r}$ decreases sharply from $x/L = 0.904$ to 0.978 for all the cases, unlike that reported by Huang et al. [46]. A possible reason for this behavior is larger flow separation in the present cases compared to the experiment, which were conducted at higher Re.

5.3.4 Dependence of the wake on TBL characteristics

The wake of the body is closely related to its boundary layer. Figure 5.16 shows the mean axial velocity profile in the wake, $6D$ downstream of the stern for all the cases.

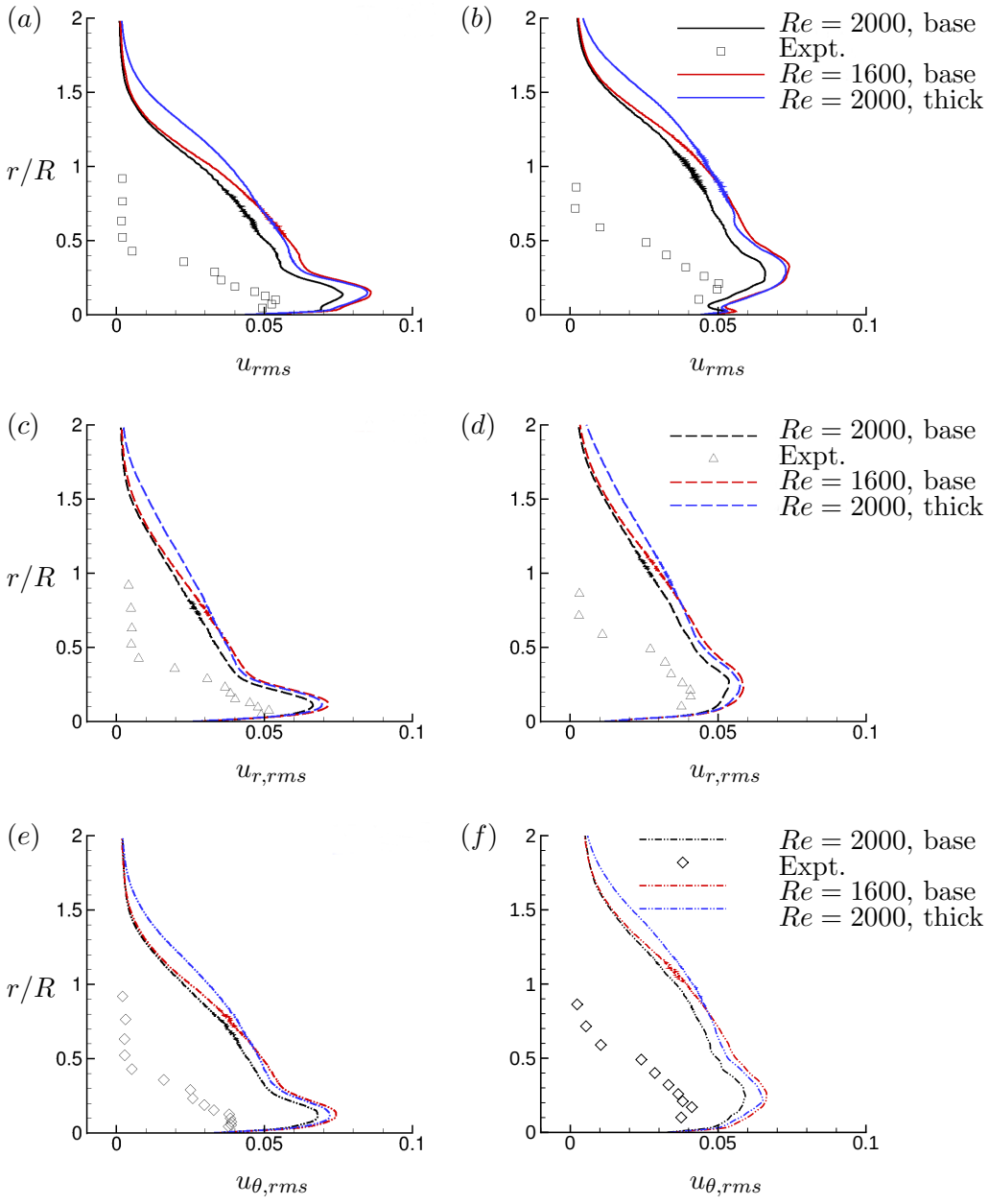

Figure 5.14: Profiles of rms of axial (u_{rms}), radial ($u_{r,rms}$) and azimuthal ($u_{\theta,rms}$) velocity at $x/L = 0.904$ (a,c,e) and 0.978 (b,d,f). Symbols are measurements of Huang et al. [46] at $Re = 1.2 \times 10^7$.

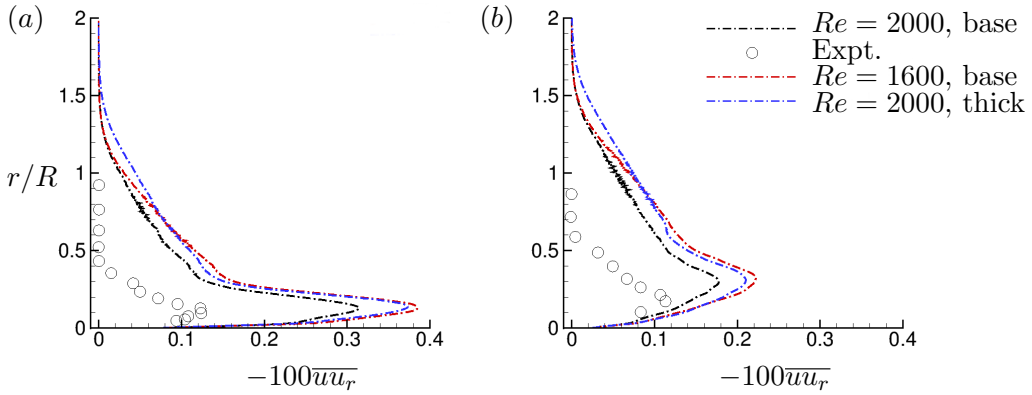

Figure 5.15: Profiles of Reynolds stress ($-\overline{uu_r}$) at $x/L = 0.904$ (a) and 0.978 (b). Symbols are measurements of Huang et al. [46] at $Re = 1.2 \times 10^7$.

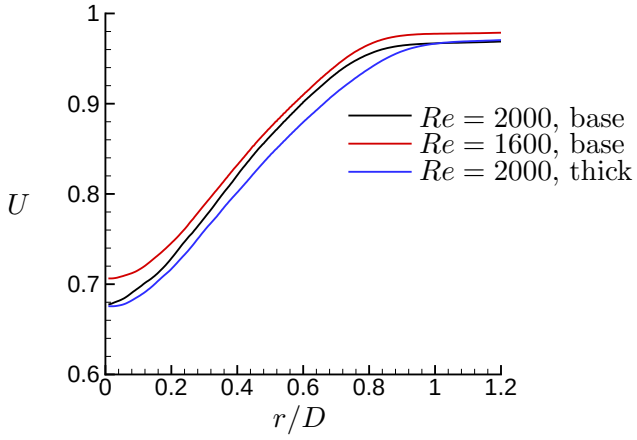

Figure 5.16: Profiles of mean axial velocity (U) at $6D$ downstream of the stern.

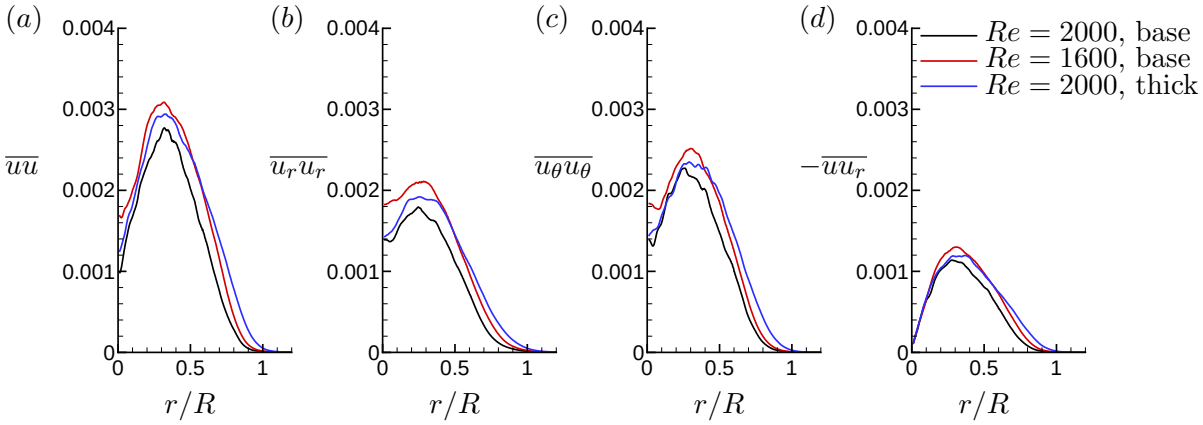

Figure 5.17: Profiles of $\overline{uu}$ (a), $\overline{u_r u_r}$ (b), $\overline{u_\theta u_\theta}$ (c) and $-\overline{uu_r}$ (d) at $6D$ downstream of the stern.

The edge velocity is sensitive to Re_θ of the incoming TBL. The lower Re_θ case has higher edge and centerline velocities. However, the change in θ has no such effect. At the same location, profiles of mean turbulent intensities and Reynolds stress are shown in Figure 5.17 for all the cases. The turbulent intensities and Reynolds stress are sensitive to both Re_θ and θ. The base case has lowest peak value for all the quantities. A possible reason for this can be that both smaller Re_θ and larger θ can promote early separation and hence enhanced turbulence in the stern region. All the components of velocity fluctuations are comparable in magnitude with the axial component being the highest and the radial being the lowest.

5.4 Summary

The influence of the boundary layer characteristics on the flow field in the stern region and the wake of a streamlined body of revolution is studied using wall-resolved LES. The geometry is the stern portion of DARPA SUBOFF without appendages, which has been used in numerous past studies. LES of flow over the body is performed first at an inflow $Re_\theta = 2000$ and $\theta/a = 0.078$. In order to study the effect of inflow Re_θ and θ, two additional simulations are performed: (i) thicker TBL keeping Re_θ same and (ii) lower

Re_θ keeping θ/a same. Turbulent inflows needed for the simulations are generated from auxiliary simulations of spatially evolving axisymmetric TBL, which employ a recycle-rescale method. The computational grid is designed to avoid confinement effects and adequately resolve all essential flow features.

Pressure coefficient on the body is largely insensitive to the incoming boundary layer characteristics, except in the vicinity of flow separation, where it is more sensitive to θ. Skin-friction on the other hand, is very sensitive to the boundary layer characteristics. The boundary layer characteristics determine the location of flow separation and hence, the flow field in the stern region and the wake. It is shown that a small variation in Re_θ or θ on the body can lead to a different flow field in the stern region and the wake.

Chapter 6

LES of propeller wake at design operating condition

In this chapter, well-resolved LES of flow over a marine propeller is performed at design advance ratio. The objectives of this chapter are to: (i) evaluate the ability of LES to capture the complex evolution of propeller wakes, (ii) study the flow field in blade passages and the origin of loads on propeller and (iii) understand the complex dynamics of the propeller wake and its transition to instability. Simulation details including the computational grid and boundary conditions are described in Section 6.1. The simulations are validated against experimental data in Section 6.2 and results are discussed in Section 6.3. The mechanisms of propeller wake instabilities are discussed in Section 6.4. The dynamics of the propeller wake is discussed in Section 6.5. The chapter is summarized in Section 6.6.

6.1 Simulation details

Simulations are performed for marine propeller DTMB 4381, which is a five-bladed, right-handed propeller with variable pitch, no skew and no rake. The geometric details of the propeller are reported in Bridges [6]. The spanwise distribution of chord length and blade twist for this propeller is shown in Figure 6.1.

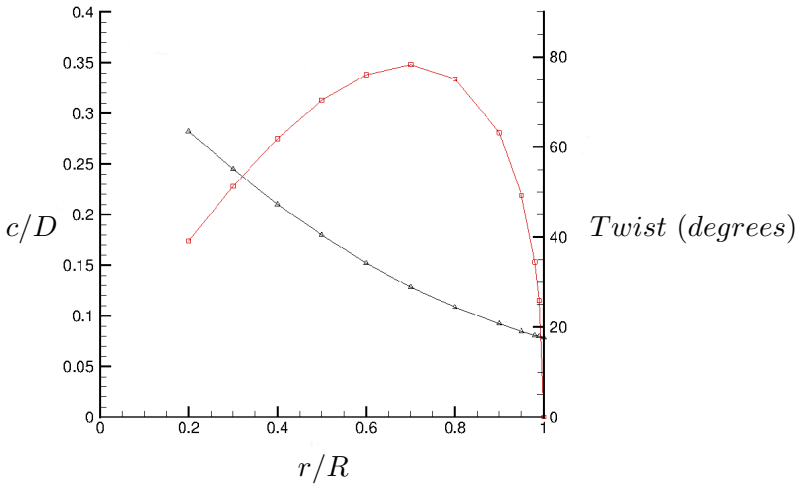

Figure 6.1: Chord (–□–) and twist angle (–△–) distribution for P4381 blades.

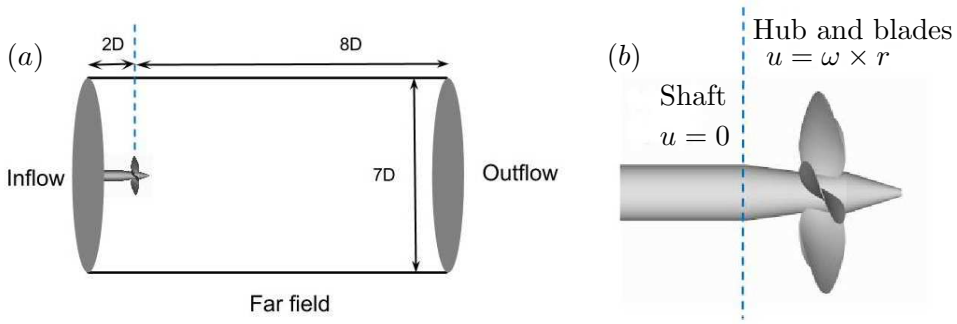

Figure 6.2: (a) Computational domain and boundary conditions on domain boundaries, (b) boundary conditions on solid walls.

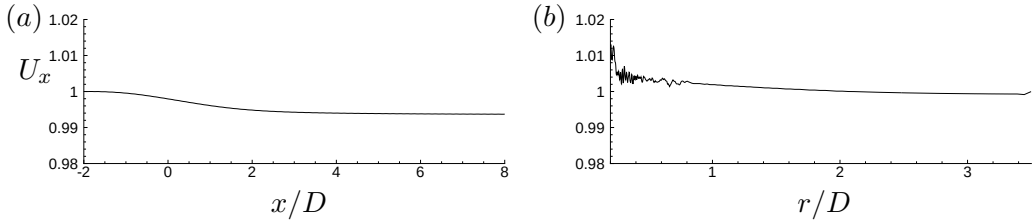

Figure 6.3: The variation of axial velocity (U_x) in : (a) streamwise direction at $r/D = 3.2$ and (b) radial direction at $x/D = -2$. The variation of axial velocity from freestream is less than 1%.

The domain size affects the propeller wake width and the pitch [e.g. 153]. Therefore, the computational domain (Figure 6.2) is designed to be large enough to avoid any confinement effect. The computational domain is a cylinder of diameter $7.0D$ and length $10.0D$ where, D is the diameter of the propeller disk. The blockage ($\epsilon = A_d/C$, where A_d is the disk area of propeller and C is the area of test-section cross-section) is 0.082. As a rule of thumb, it is often assumed that if $\epsilon < 0.1$, the rotor wake is practically unconfined and physical phenomena like wake instability are negligibly affected [154]. The streamwise variation of the axial velocity is negligible ($< 1\%$) at $r/D = 3.2$ as shown in Figure 6.3(a).

The reference coordinate system is chosen such that the blades of the propeller are located at the origin and the flow is in the direction of positive x. The domain extends $2D$ upstream and $8D$ downstream of the propeller. Preliminary simulations (not shown here) were performed with a longer domain in upstream region with inflow plane located at $6D$ upstream of the propeller. The radial variation of the axial velocity at $2D$ upstream of the propeller for this domain is negligible ($< 1\%$) as shown in Figure 6.3(b). It was concluded that position of inflow at $2D$ upstream of the propeller will have negligible effect on propeller wake evolution. Hence, the present simulations can be considered devoid of any confinement effects.

Freestream velocity boundary conditions are specified at the inlet and the lateral far field boundaries. Convective boundary conditions are prescribed at the outflow. Since the velocities in the governing equations are written in the inertial frame, boundary conditions on solid walls are also prescribed in the inertial frame. Thus, boundary

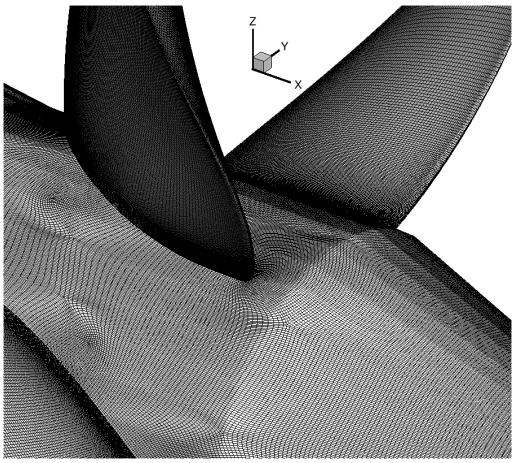

Figure 6.4: Close up of surface mesh.

conditions on the rotor part, blades and hub are specified as $u = \omega \times r$, while those on the shaft are prescribed as no-slip boundary conditions. A schematic of the computational domain and boundary conditions is shown in Figure 6.2.

In this chapter, simulations are performed using a computational grid which has has 181 million control volumes consisting of only hexahedral cells. The unstructured grid for the propeller is shown in Figure 6.4. The grid is designed carefully to capture all the essential features of the flow field. Any transverse cross-section on the shaft has 600 cells in azimuthal direction. The radial cross-section of each blade has 324 cells along its circumference for most part except near the tip. There are at least 170 cells in the radial direction extending from root to tip on each blade. The grid is clustered close to all solid surfaces. Ten layers of hexahedral cells are extruded from the surface with a minimum wall-normal spacing of $0.0017D$ on blades and $0.00017D$ on hub and shaft surfaces to resolve near-wall flow features. A growth ratio of 1.02 is applied at all solid surfaces to transition from fine to coarser resolution away from the surface. The grid is refined in the wake region of the propeller to capture small scales. The entire grid is partitioned over 2048 processors and the simulations are performed with a time step of 0.001 unit, which corresponds to 10668 computational time steps per rotation.

6.2 Validation

Large Eddy Simulations are performed at design advance ratio, $J = 0.889$ at a Reynolds number $Re = 894,000$. The value of Re is chosen to match with the experimental conditions [101, 155]. The advance ratio J and Reynolds number Re are defined as

$$J = \frac{U}{nD}, \quad Re = \frac{UD}{\nu}$$

where U is the freestream velocity, n is the propeller rotational speed, and D is the diameter of the propeller disk. Using the velocity magnitude experienced by the airfoil section of the blade and chord length, the Reynolds number

$$Re_C = \frac{U_{0.7}c_{0.7}}{\nu}$$

where $U_{0.7}$ and $c_{0.7}$ are the velocity magnitude and chord-length at a radial location of $r/R = 0.7$. Here,

$$U_{0.7} = \sqrt{U^2 + (2\pi 0.7Rn)^2}.$$

The flow parameters of the simulations and experiments are listed in table 6.1. Here, OW and WT refers to the open water tow tank and water tunnel experiments respectively [101, 155].

Defining Thrust T as the axial component of force and torque Q as the axial component of the moment of force, the non-dimensional thrust coefficient K_T and torque coefficient K_Q are given by

$$K_T = \frac{T}{\rho n^2 D^4} \quad and \quad K_Q = \frac{Q}{\rho n^2 D^5},$$

where ρ is the density of the fluid.

The computed values of mean K_T and K_Q are compared to the experimental results of Jessup et al. [101, 155] and Hecker and Remmers [156] in Table 6.1. Jessup et al. [101, 155] report experiments conducted in 36 inch water tunnel (WT) and open water towing-tank (OW) whereas Hecker and Remmers [156] report experiments conducted in

	Re ($\times 10^5$)	Re_C ($\times 10^5$)	$\langle K_T \rangle$	$\langle K_Q \rangle$
LES	8.9	8.3	0.21	0.041
OW [101]	11	10.2	0.201	0.0421
WT [155]	8.9	8.3	0.18	0.038
OW [156]	6.47	6	0.211	0.042

Table 6.1: Flow parameters and mean values of thrust and torque coefficient at design condition.

an open water towing-tank. LES results for $J = 0.889$ (Table 6.1) show good agreement with experiments for mean value of K_T and K_Q. The measured values of loads is slightly smaller in the water tunnel, possibly due to tunnel effects. Our computed values of mean K_T and K_Q show good agreement with tow-tank data.

The phase-averaged flow field in blade wake is compared to PIV measurements [157] in Figure 6.5. The contours of computed radial and axial velocity fields are compared to the experimental data in Figure 6.5(a-d). The thin vortex sheet in blade trailing edge wake is nicely captured in the simulations which can be seen in both axial and radial velocity fields. The jump in radial velocity is sharper in results obtained from LES as compared to that of PIV showing the level of resolution of the computational grid. The axial velocity contours also show better resolution of the tip vortex and blade wake in LES compared to that of the experiments having coarser spatial resolution. For more detailed comparison, profiles of axial velocity are shown at three streamwise locations ($x/D = 0.06$, 0.08 and 0.1) in Figure 6.5(e-g) and also at three radial locations ($r/D = 0.35$, 0.4 and 0.45) in Figure 6.5(h-j). Overall, the LES results show good agreement with the experiments.

The phase-averaged eddy viscosity normalized with the molecular viscosity is shown in Figure 6.6. The magnitude of eddy viscosity is small in the near field of propeller wake suggesting that the grid is resolving the flow field adequately.

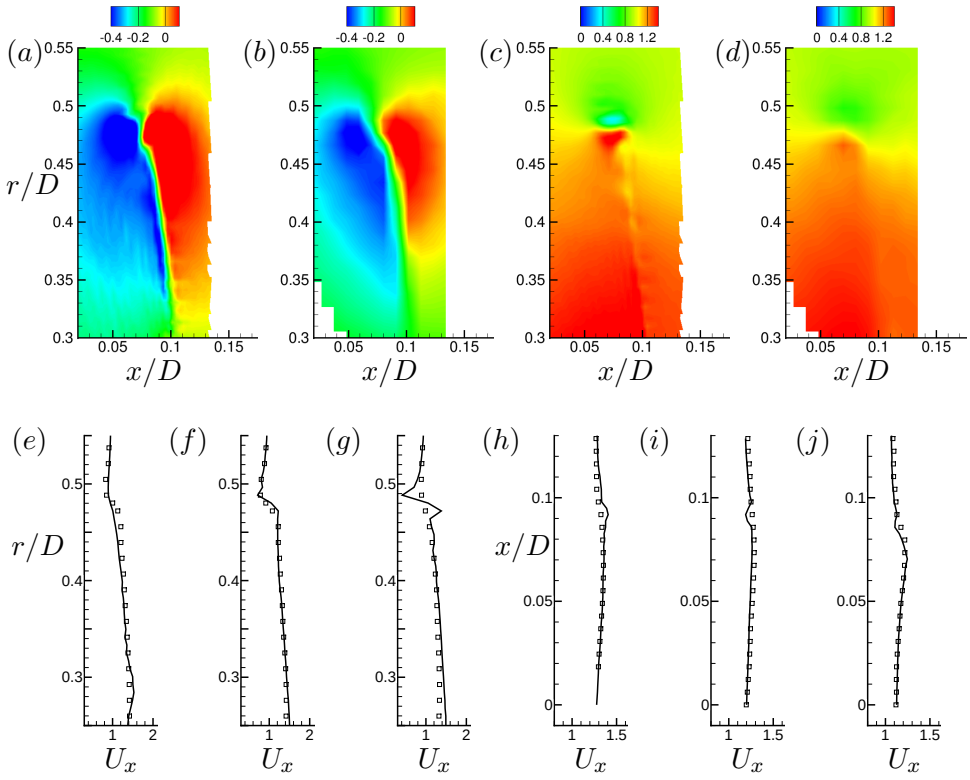

Figure 6.5: Phase-averaged blade wake: comparison between LES (a,c) and PIV (b,d); radial (a,b) and axial (c,d) velocities are compared. Axial velocity profiles are extracted and compared to PIV at streamwise (e-g) locations $x/D = 0.06$ (e), 0.08 (f) and 0.1 (g); and radial (h-j) locations $r/D = 0.35$ (h), 0.4 (i) and 0.45 (j). —, LES; ▫ , Experiment (PIV). The values are normalized with U.

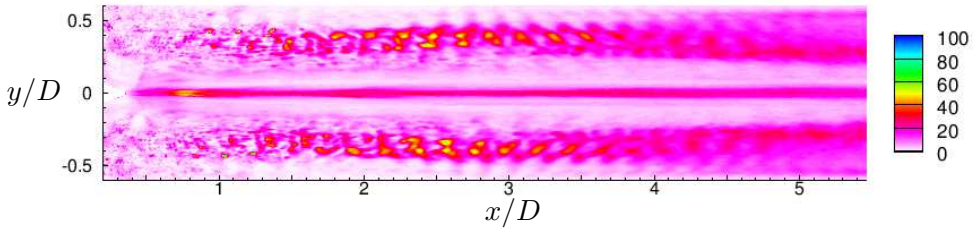

Figure 6.6: Phase-averaged contours of eddy viscosity normalized with the molecular viscosity.

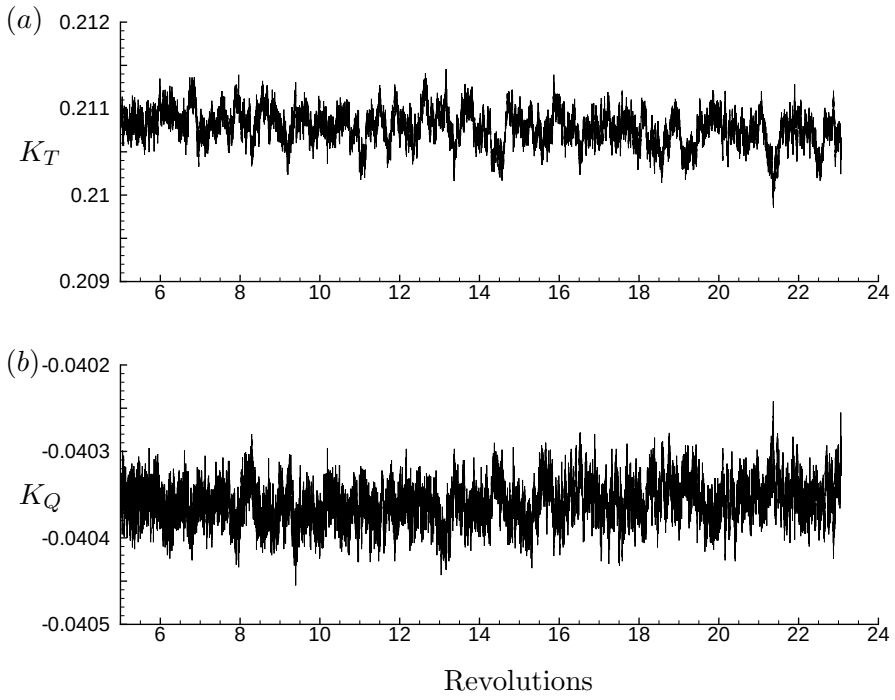

Figure 6.7: Time history of unsteady loads on propeller: (a) K_T and (b) K_Q.

6.3 Results

6.3.1 Propeller loads

The time history of thrust (K_T) and torque (K_Q) coefficient are shown in Figure 6.7. Unlike off-design conditions like crashback [98], the deviation of loads from the mean is small at design conditions. The contribution of pressure and viscous forces to the thrust generated by the propeller is shown in Figure 6.8(a). Note that the viscous force is negative. The magnitude of viscous contribution to thrust is compared to that of pressure. Pressure force is two orders of magnitude higher than that of viscous force generated by the propeller.

The frequency spectra of the loads are computed by dividing the time history into a finite number of segments with 50% overlap, applying a Hann window and rescaling to maintain the input signal energy. Each such segment is then transformed into the

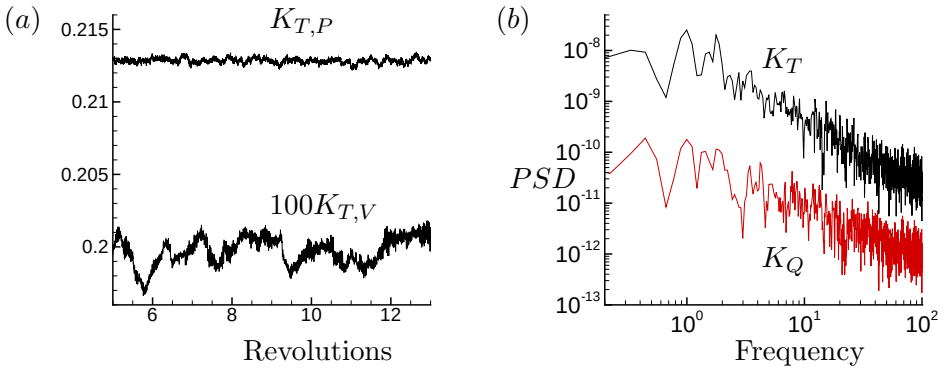

Figure 6.8: (a) Pressure and viscous contribution to thrust generated by the propeller and (b) PSD of unsteady loads, K_T and K_Q.

frequency domain by taking a Fast Fourier Transform (FFT). The power spectral density (PSD) is then averaged over all the segments. Figure 6.8(b) shows the PSD of the magnitude of K_T and K_Q as a function of non-dimensionalized frequency (rev^{-1}). The unsteady loads on the propeller are broadband at design loading as evident from PSD of both K_T and K_Q. Figure 6.9(a) and (b) shows C_p with streamlines on the pressure and suction sides of propeller blades respectively. C_p is defined as $\frac{p-p_0}{0.5\rho U^2}$ where p is pressure on the blade and p_0 is freestream pressure. The flow accelerates on the suction side of the blade for the most part as evident from the lower pressure in that region. For both pressure and suction sides, the trailing edge region near the tip of the blade has the lowest pressure.

In order to understand the contribution of different parts of blades to K_T, the entire blade is split into 10 equal parts in radial direction and the contribution to K_T from each part is shown in Figure 6.10(a) for both pressure and suction sides. Note that most of the thrust is generated from the region around the mid span of the blades. This is because the blade has the highest chord-length in mid span and hence larger surface area for lift generation. The average spanwise loading on each blade can be computed from the circumferentially averaged azimuthal velocity similar to Jessup et al. [101] as follows:

$$G(r) = r\overline{U_\theta}(r)/Z \tag{6.1}$$

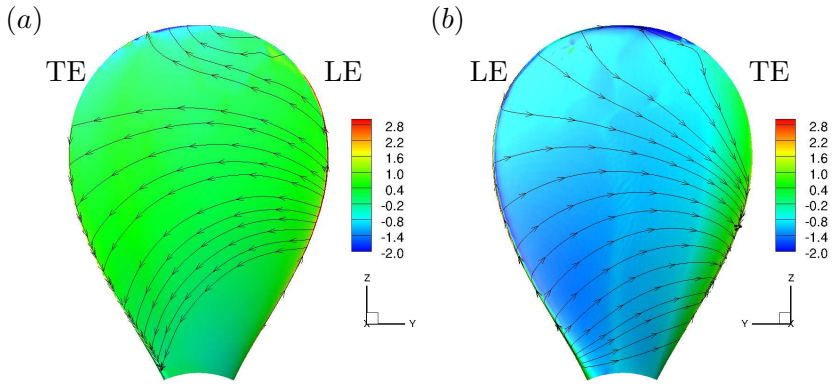

Figure 6.9: Pressure coefficient (C_p) on propeller blade with streamlines at $J = 0.889$. (a) pressure side and (b) suction side.

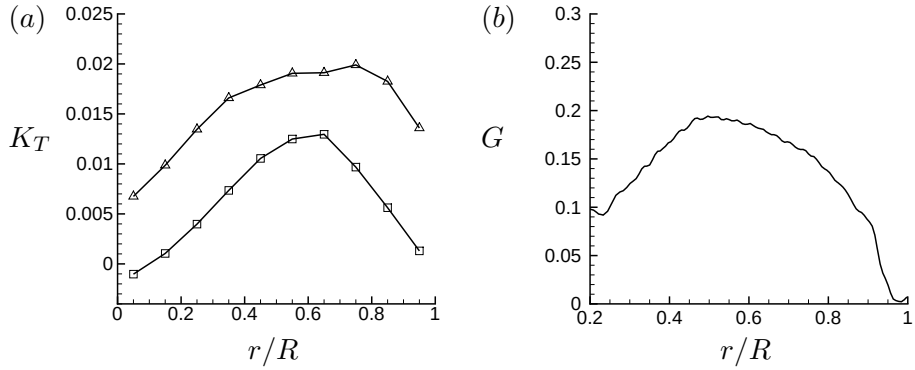

Figure 6.10: (a) Radial distribution of thrust coefficient: pressure side, –△–; suction side, –□– and (b) average circulation at $x = 0.23R$ at design load.

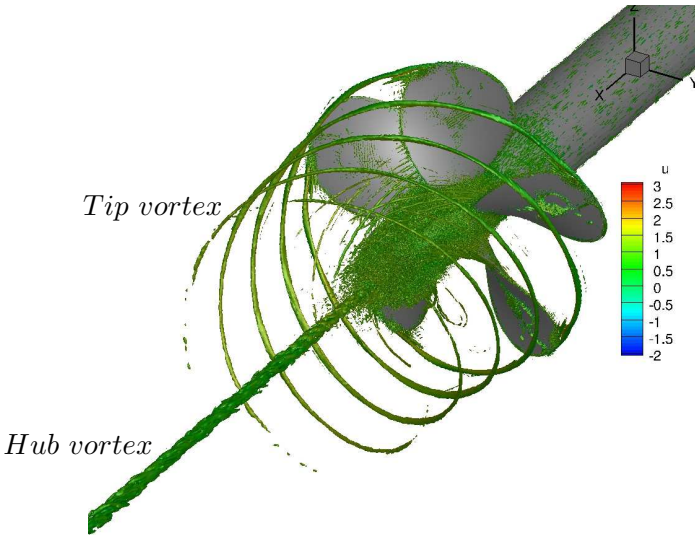

Figure 6.11: Isocontour of λ_2 colored with axial velocity showing hub and tip vortices.

where Z is the number of blades. The radial distribution of average spanwise loading is computed at $0.23R$ downstream of the propeller using equation 6.1 as shown in Figure 6.10(b). The blade is gently loaded at the tip. This has an effect on the strength of the tip vortices generated by the propeller. A higher loading near the tip would generate stronger and larger tip vortex. The strength of the vortices shed by the blade trailing edge is directly related to the radial gradient of circulation near that section of the blade. The average circulation for the propeller blades reach a maximum around $0.5R$ followed by a decrease to zero at the tip. Thus, this propeller at design loading is expected to have stronger blade trailing edge wake as compared to propellers with heavy tip loading. This has major consequences in the dynamics of wake evolution as discussed in the following sections.

6.3.2 Axial evolution of propeller wake

The propeller wake consists of five helical tip vortices (one originating from each blade) and an axial hub vortex. The coherent vortical structures in the propeller wake is visualized using λ_2 criterion [158]. λ_2 is the median of the three eigenvalues of $S^2 + \Omega^2$; here S and Ω are respectively the symmetric and antisymmetric parts of the velocity

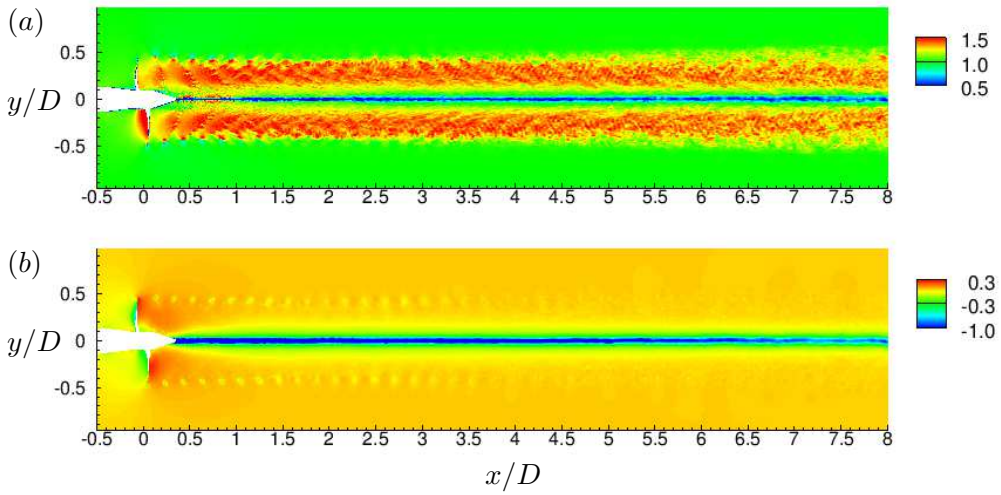

Figure 6.12: Instantaneous flow field in xy plane: (a) axial velocity and (b) pressure. The axial velocity is normalized with U whereas pressure field is normalized with ρU^2.

gradient tensor ∇u. The isocontour of λ_2 colored with axial velocity is shown in Figure 6.11. The structures at the inner radial location very near to the propeller are formed by the shedding of vorticity in the wake of individual blades. Figure 6.12 shows the instantaneous flow field in xy plane. The near field is dominated by coherent tip vortices and blade trailing edge wake. These vortical structures become unstable and eventually break up to form the far wake. The vortex cores are seen clearly in contours of pressure field as a region of low pressure. The region inside the hub vortex has the lowest pressure, and hence is more susceptible to cavitation. The hub vortex region remains coherent with minor oscillations in the far field.

The flow field is phase-averaged over more than 15 rotations of the propeller after the transients die out and analyzed in radial and axial planes from near to far field. Figure 6.13 shows the phase-averaged axial velocity and vorticity magnitude for the entire wake. Note the acceleration of the flow through the propeller, contraction of slipstream and straining of the axial velocity in the near field. The axial velocity plot shows that the propeller wake has higher axial velocity than that of freestream everywhere except in the hub vortex region, which is straight and confined to a thin region near axis. The vorticity field shows that the thin trailing edge wakes generated by the rotating

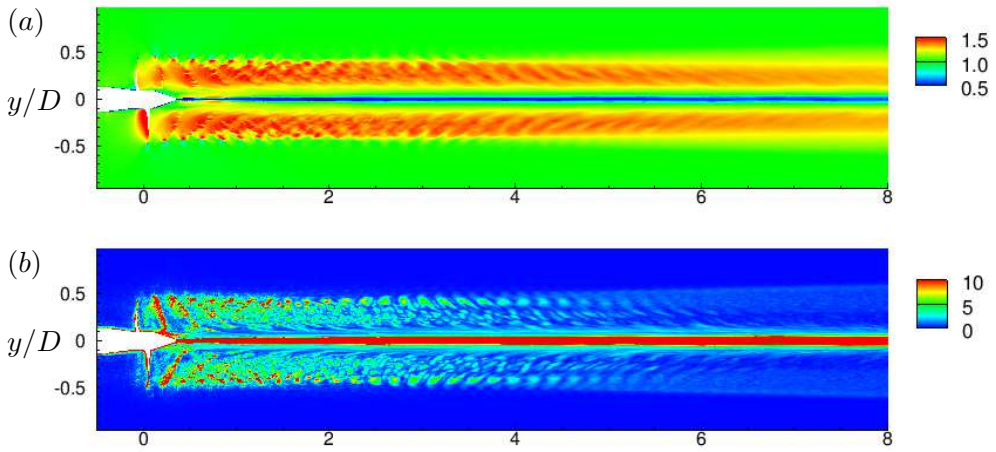

Figure 6.13: Phase-averaged flow field in xy plane: (a) axial velocity and (b) vorticity magnitude. The axial velocity is normalized with U. The vorticity magnitude is normalized using U and R.

blades break apart in the near field, generating a wake composed of hub and tip vortices along with smaller vortices which are generated by the break up of blade trailing edge wakes. In the far field, the vortical structures present near the edge of the propeller wake weaken progressively until they are indistinguishable beyond $5D$ as observed in Figure 6.13(b).

The pressure fluctuations and TKE are shown in the axial plane in Figure 6.14. In the near field, the signature of blade can be observed in both pressure fluctuations and TKE. The values of pressure fluctuation and TKE is negligible in the region of stable tip vortex. In fact, there is a streamwise decay in TKE in the near field up to 1 diameter. This is due to decay of the shear layer of the blade wake which is the source of TKE production in the near field. As soon as the tip vortex becomes unstable, both pressure fluctuations and TKE start increasing again. After roughly 3 diameters downstream of the propeller, the tip vortex breaks down completely producing TKE. Subsequently, the radial extent of both pressure fluctuations and TKE spreads as we move further downstream. In the hub vortex, the TKE first decreases and then increases as we move downstream. The higher value of TKE in the hub vortex near the propeller is due to

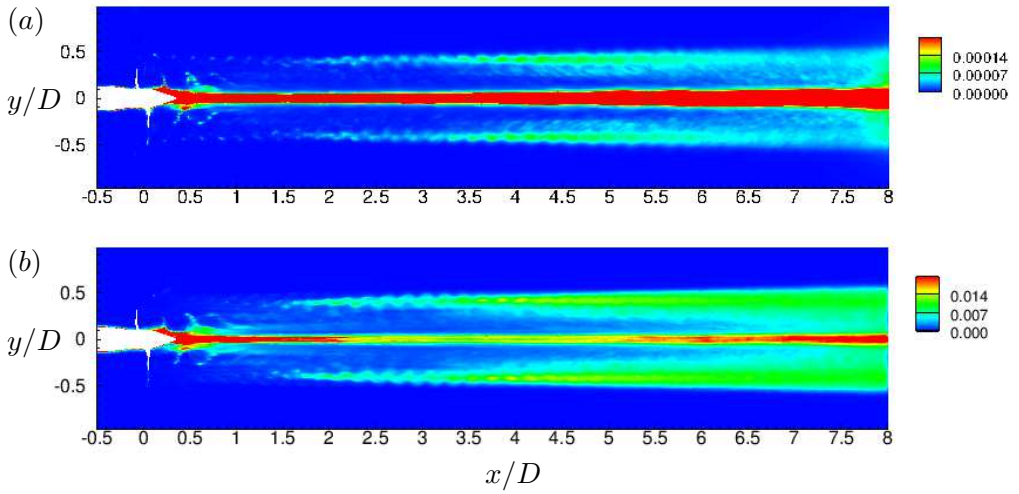

Figure 6.14: Phase-averaged flow field in xy plane: (a) pressure fluctuations and (b) turbulent kinetic energy. The flow field quantities are normalized appropriately using ρ and U.

unsteadiness generated by flow separation on the hub. As we move axially downstream in the hub vortex, there is a sharp decrease in TKE followed by an increase in TKE after the tip vortices destabilize. The tip vortex destabilization causes oscillations in the hub vortex leading to the production of turbulence. This streamwise growth of TKE increases rapidly in the hub vortex once the tip vortices break down completely. This behavior supports the hypothesis of Felli et al. [77] that there is a cause-effect relationship between the tip and hub vortex instability in propeller wakes.

A series of transverse planes are extracted at 9 streamwise locations, one upstream ($x/D = -0.2$) and 8 downstream ($x/D = 0.2, 0.4, 0.6, 1, 1.5, 3, 5$ & 7) of the propeller. The phase-averaged axial velocity, vorticity magnitude and turbulent kinetic energy are discussed below.

Flow upstream of propeller

The flow field of the propeller is shown at $x/D = -0.2$ (i.e. $0.2D$ upstream of the propeller) in Figure 6.15. The suction effect of the propeller can be seen in the axial velocity (Figure 6.15a). The vorticity and turbulent kinetic energy show that the

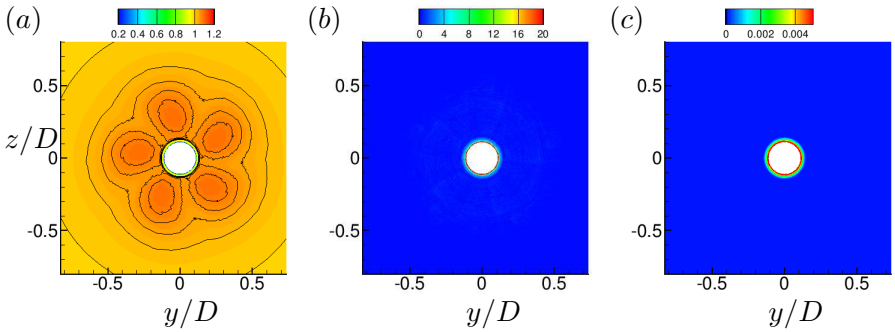

Figure 6.15: Upstream: phase-averaged axial velocity (a), vorticity magnitude (b) and TKE (c) at $x/D = -0.2$. Isolines of axial velocity are also shown from 1 to 1.2 to illustrate the suction effect of propeller. The flow field quantities are normalized appropriately using ρ, R and U.

propeller-induced perturbations do not produce significant turbulence in the upstream region. This shows that the propeller has negligible effect on its own inflow (i.e. the upstream region). All the vorticity and turbulence lie in the hub boundary layer as seen in Figure 6.15(b) & (c) respectively.

Near wake

The evolution of propeller wake in the near field is shown in Figure 6.16 at $x/D = 0.2$, 0.4 and 0.6. The vortex system comprising tip and hub vortices along with the thin vortex sheet shed by trailing edge of the blades are clearly seen. The visual inspection of instantaneous axial velocity and vorticity contours do not show any out-of-phase unsteadiness, suggesting that the trailing edge vortex sheet undergoes viscous dissipation and it is not an effect of phase-averaging. The progressive increase in the radial variation of pitch as we move downstream, causes large deformation in vortical structures present in the wake leading to the break up of the tip vortices from their respective blade wakes. The bending in blade wake also brings the tip vortex close to the trailing edge wake of the next blade, thereby assisting in further distortion and destabilization. This behavior was seen in the experiments of Felli et al. [76] as well. In their experiments, they varied the number of blades in propeller from 2 to 4 and reported that this effect was more pronounced as the number of blades increased. The generation of turbulence

is directly correlated with the destabilization of the vortices in the wake as evident from the contours of the turbulent kinetic energy.

A closer look at the axial velocity and vorticity shows break up of blade trailing edge vortex sheet. The stability and behavior of vortex sheets have been explored by many authors in the past [159–161]. Moore [159] studied the evolution of an initially plane vortex sheet which is similar to the wake generated by a fixed wing aircraft and suggested that a finite vortex sheet with a tip vortex at its end undergoes a spiral roll-up. This in turn entrains some vorticity in the tip vortex, causing an instantaneous change in the velocity field at the locations of other vortices. These perturbations lead to the Kelvin–Helmholtz instability in the region between the tip vortex and the unstretched part of the vortex sheet. The break up of blade trailing wake in the near field seems to follow a similar mechanism. However, in the present case we have an additional counter rotating hub vortex at the other end of blade trailing edge wake vortex sheet.

Figure 6.17 shows the axial component of vorticity fields at $0.4D$ and $0.6D$ downstream of the propeller. The spiral roll-up of the blade wake vortex sheet can be clearly seen. As seen in Figure 6.17(b), the blade wake has undergone complete spiral roll-up forming smaller vortical structures. These smaller vortex structures from the radially outward part of the blade interacts with the tip vortices, which among other things, dictates the evolution of propeller wake in the intermediate field.

It can be seen that although the tip vortices have broken apart from their respective blade wake, still they are stable, which is supported by the lack of turbulence in the region of tip vortices. In conclusion, the near field of propeller wake is characterized by the progressive distortion, viscous dissipation and eventual break up of thin blade trailing edge wakes leading to separation of tip vortices from their respective blade wakes.

Intermediate wake

The intermediate wake is characterized by the growth of the instabilities in tip vortices. The wake becomes increasingly unstable as we go downstream, as evident from the plots of turbulent kinetic energy (figure 6.18) from $x/D = 1$ to 1.5. The flow field

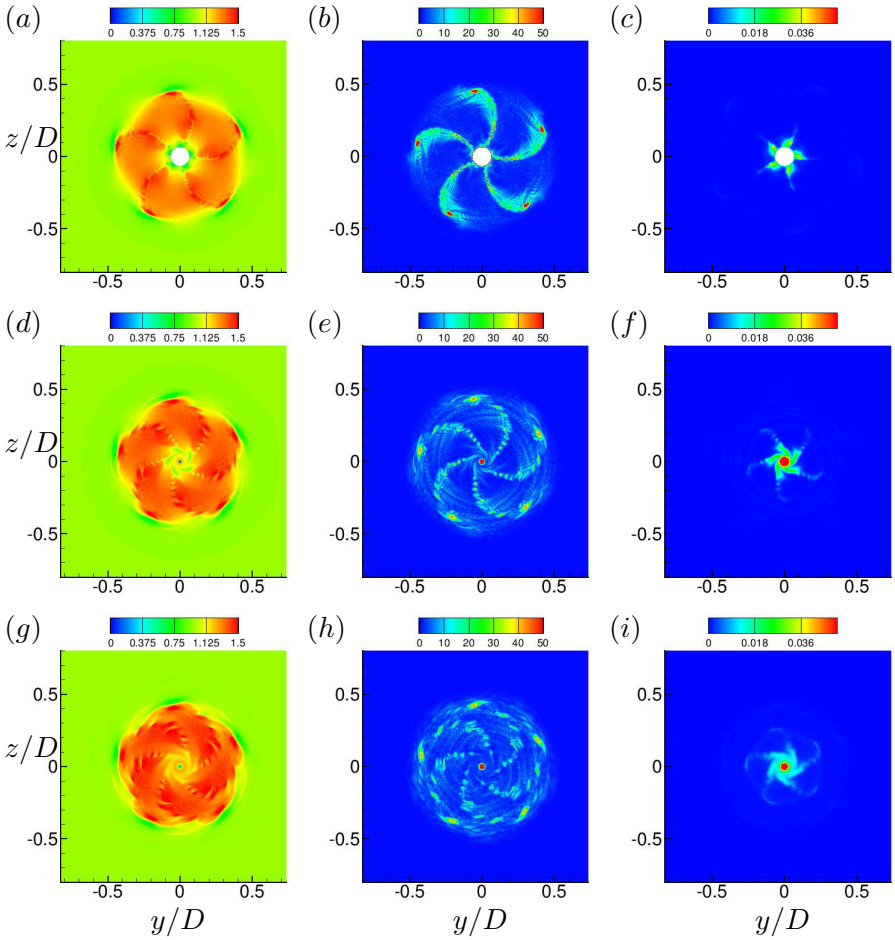

Figure 6.16: Near wake: phase-averaged axial velocity (a,d,g), vorticity magnitude (b,e,h) and TKE (c,f,i) at $x/D = 0.2$ (a-c), 0.4 (d-f) and 0.6 (g-i). The flow field quantities are normalized appropriately using ρ, R and U.

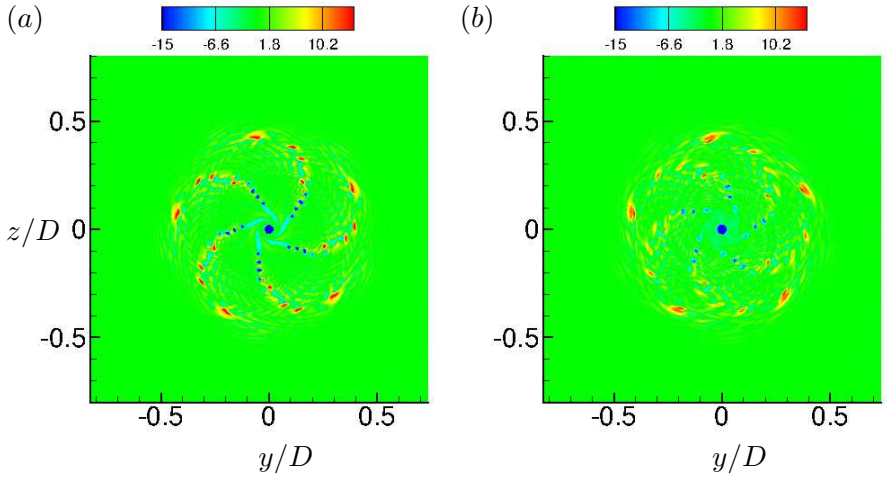

Figure 6.17: Roll-up in blade trailing edge wake. Axial component of vorticity at $x/D = 0.4$ (a) and 0.6 (b). The values are normalized appropriately using U and R.

at $x/D = 1.5$ shows the weakening of tip vortex signatures as compared to $x/D = 1$. The vorticity plot at $x/D = 1.5$ (Figure 6.18e) shows additional vortical structures along with the tip vortices. The possible mechanism of their formation is described as follows. As described in previous section (§6.3.2), the blade trailing edge wake which is a thin vortex sheet, breaks up into smaller fragments (Figure 6.16). Figure 6.19 shows z-component (out-of-plane) of vorticity. It can be seen that the tip vortices and hub vortex are of opposite sign whereas the tip vortex and trailing edge wake of the preceding blade are of same sign, hence they attract each other. The tip vortex being stronger, pulls the weak blade wake vortices closer to its own axial plane as the wake evolves from near field to the intermediate field. These vortical structures are responsible for the onset of turbulence and pressure fluctuations generation near the edge of the wake seen earlier in Figure 6.14.

It should be noted that the mechanism of mutual-inductance mode of instability explained here is fundamentally different than what was observed and described by earlier authors. Di Felice et al. [73] and Felli et al. [75] explained that the interaction between the tip vortex and the trailing wake of the adjacent blade in the same transverse plane

cause the tip vortex to break apart from its trailing edge blade wake. Felli et al. [77] performed detailed experiments with propellers and noted that the transition to instability may be correlated more to spiral-to-spiral interaction than to the complete development of trailing wake roll-up. They explained that the mutual-inductance between the adjacent tip vortices causes the adjacent tip vortex spirals to roll-up around each other causing *leap-frogging*, particularly for a four-bladed propeller due to proximity of tip vortex spirals. However in the present case, we see mutual-inductance between tip vortex and adjacent blade wake in the axial plane. The possible reason for the difference in the mechanism of mutual-inductance between the present case and those reported earlier in the literature is the blade geometry itself. The blade geometry of the propeller used in the experiments of Di Felice et al. [73], Felli et al. [75] and Felli et al. [77] is such that it is highly loaded at the tip, thus shedding strong tip vortices. The blades also have a forward rake and slight skew. On the other hand, the propeller used here is without any skew and rake and is nominally loaded (see Figure 6.10b) at the tip, thus shedding a relatively weaker tip vortex and a stronger blade trailing edge wake at design conditions.

Hence, although the mutual-inductance mode of instability is dominant in wake destabilization, the actual mechanism is dependent on the geometry as well as the operating condition. Propellers which are highly loaded at the tip will produce stronger tip vortices, causing spiral-to-spiral interaction of tip vortices to be the dominant mechanism of wake instability as opposed to the propellers with nominally loaded tip, where the interaction between the blade wake and adjacent tip vortices in both axial and transverse planes is the dominant mechanism for the propeller wake instabilities.

Far wake

The evolution of propeller wake in the far field is shown in Figure 6.20. The contours of phase averaged axial velocity, vorticity and turbulent kinetic energy contours are plotted at $x/D = 3$, 5 and 7 downstream of the propeller. Once the tip vortices destabilize completely in the intermediate wake, the wake evolves as a shear layer in both axial and azimuthal direction. These shear layers are susceptible to shear layer instabilities.

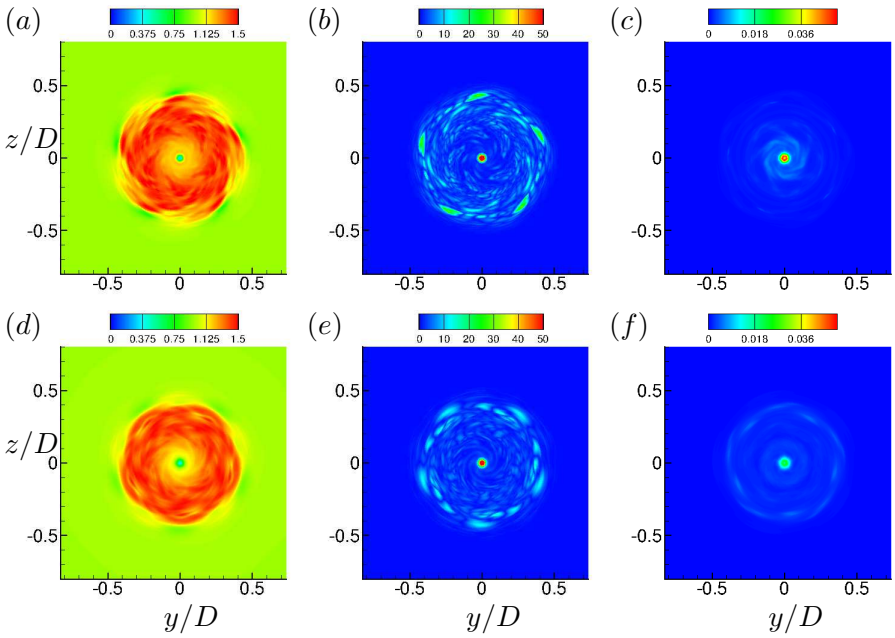

Figure 6.18: Intermediate wake: phase-averaged axial velocity (a,d), vorticity magnitude (b,e) and TKE (c,f) at $x/D = 1$ (a-c) and 1.5 (d-f). The values are normalized appropriately using U and R.

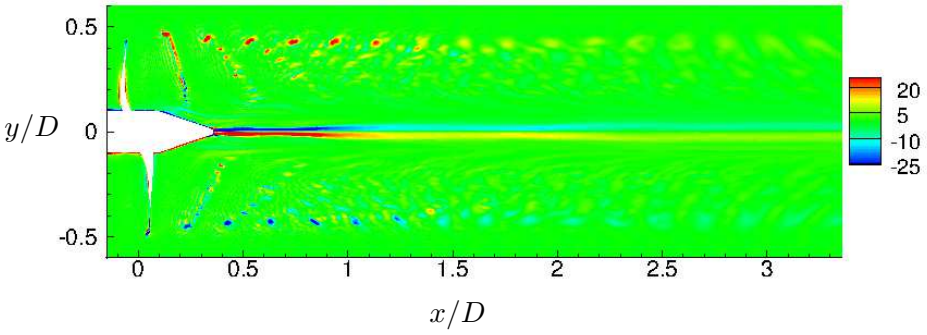

Figure 6.19: Close-up view of z-component of vorticity in xy plane. The values are normalized appropriately using U and R.

There are minor signs of the Kelvin–Helmholtz instabilities in both axial (Figure 6.13a) and azimuthal (Figure 6.20a) shear layers around $x = 3D$. The turbulent kinetic energy plots suggest generation of turbulence in the outer edge of the wake as well as the hub vortex core. The region between the outer edge of wake and the edge of hub vortex is comparatively less turbulent. This region seems to possess some flow structures which look like mild signature of propeller blades mainly in the axial velocity field. This could be related to the centrifugal instability of the propeller wake which acts as a swirling jet of fluid around an axial hub vortex. The vorticity plots suggest that all the tip vorticity is dissipated and most of the vorticity lies in the hub vortex (Figure 6.20e).

6.3.3 Flow in blade passage

The phase-averaged axial velocity and pressure field in the vicinity of the propeller are plotted in Figure 6.21 for two cylindrical cut planes at $r/R = 0.4$ & 0.7 showing flow field details at root and mid span sections of propeller blades respectively. The flow is attached at both these radial locations. Acceleration of flow can be seen in the blade passage which create pressure difference across the blade sides generating net force and torque. The wake of blades has trailing edge vortices which give appearance of streaks in the plots. The spreading of the wake of the airfoil sections of blades can also been seen here. The blade wakes have larger spreading near mid span section as compared to blade root. The spreading in the phase-averaged velocity field is the result of unsteadiness in the flow field which increases as we move downstream.

The phase-averaged axial velocity (Figure 6.22), vorticity magnitude (Figure 6.23) and turbulent kinetic energy (Figure 6.24) are plotted in $x\theta$ plane at three radial distance of 40%, 70% and 95% radius from the axis for the entire wake. Stripes of low and high velocity are distinct in near field. The wakes from the adjacent blades interact with each other as they evolve downstream. Such interactions are particularly stronger for a five-bladed propeller as the blade wakes are closer to each other as compared to say, two-bladed propellers. The spatial oscillations in the blade wakes causes meandering and smearing as observed in the plots of phase-averaged flow field quantities. Such effects are very prominent between $1 < x/D < 3$. Note that there is lack of distinct low and

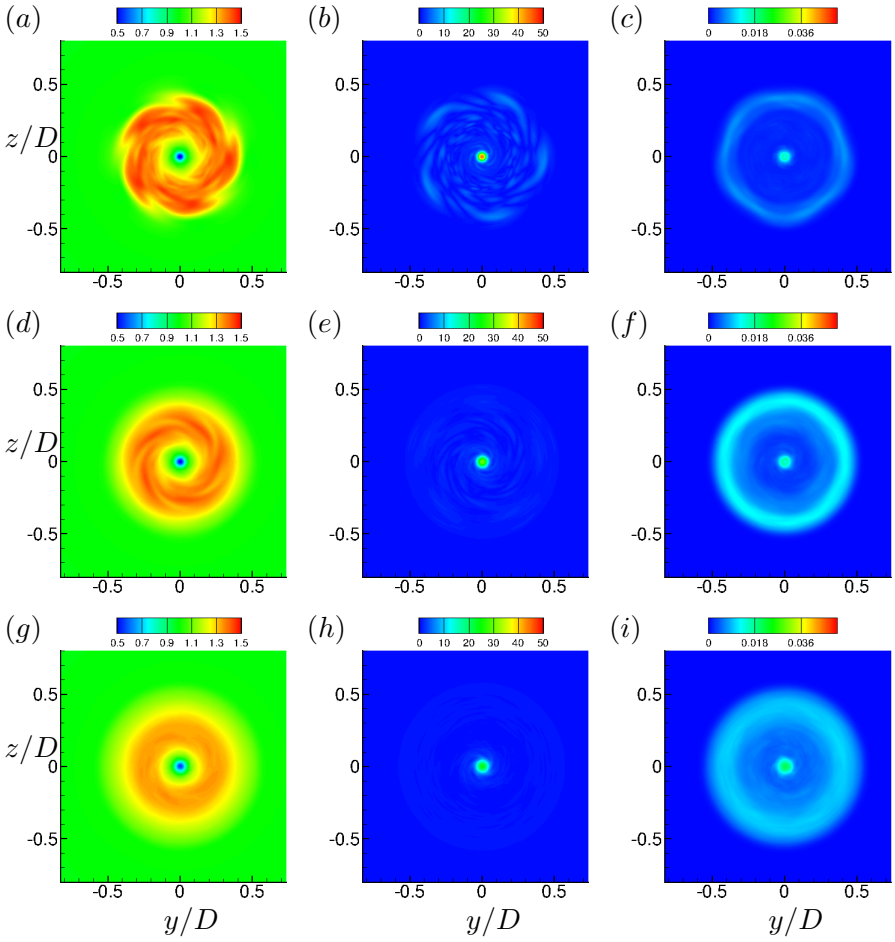

Figure 6.20: Far wake: phase-averaged axial velocity (a,d,g), vorticity magnitude (b,e,h) and TKE (c,f,i) at $x/D = 3$ (a-c), 5 (d-f) and 7 (g-i). The values are normalized appropriately using U and R.

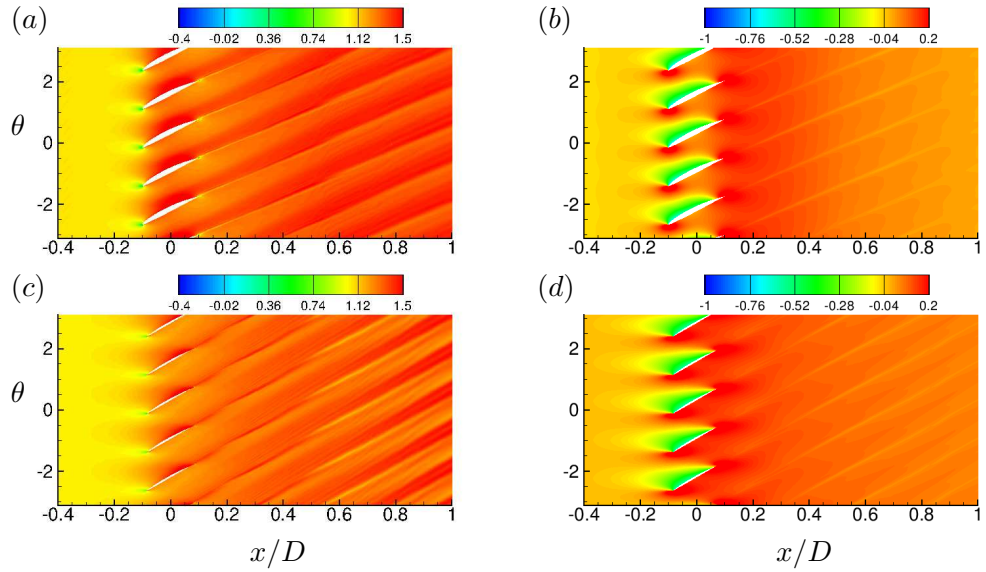

Figure 6.21: Phase-averaged axial velocity (a,c) and pressure (b,d) in $x\theta$ plane at: $r/R = 0.4$ (a,b) and $r/R = 0.7$ (c,d). The axial velocity and pressure are normalized with U and ρU^2 respectively.

high velocity regions at $0.95R$ radially outward from axis. This is because of low loading and chord length at this radial location. Nevertheless, there is shedding of tip vortices whose effect is seen in near field but then, the wake undergoes streamtube contraction. Also, the slope of the stripes depends on blade twist and loading conditions. As blade twist (Figure 6.1) and approach velocity vary with varying radial location, the slope of the stripes varies radially. This slope is smallest near the root and increases radially outward from axis. Blade wakes contain vorticity which form stripes in vorticity plots as well (Figure 6.23). These striped patterns are clear even at $0.95R$ which is due to high velocity gradients in this region. Wake contraction effects are visible here as well. There appear to be stripes of vorticity at $r/R = 0.7$ around $x/D = 2$. This is formed by the process of entrainment of the small vortical structures formed by the break up of blade trailing edge wakes by the tip vortices, which happens in the intermediate wake as discussed in section §6.3.2. The transition of blade wakes to instability can be visualized by turbulent kinetic energy (Figure 6.24). The turbulence is produced near the root first. This is because of viscous diffusion of thin blade wake. This onset of turbulence

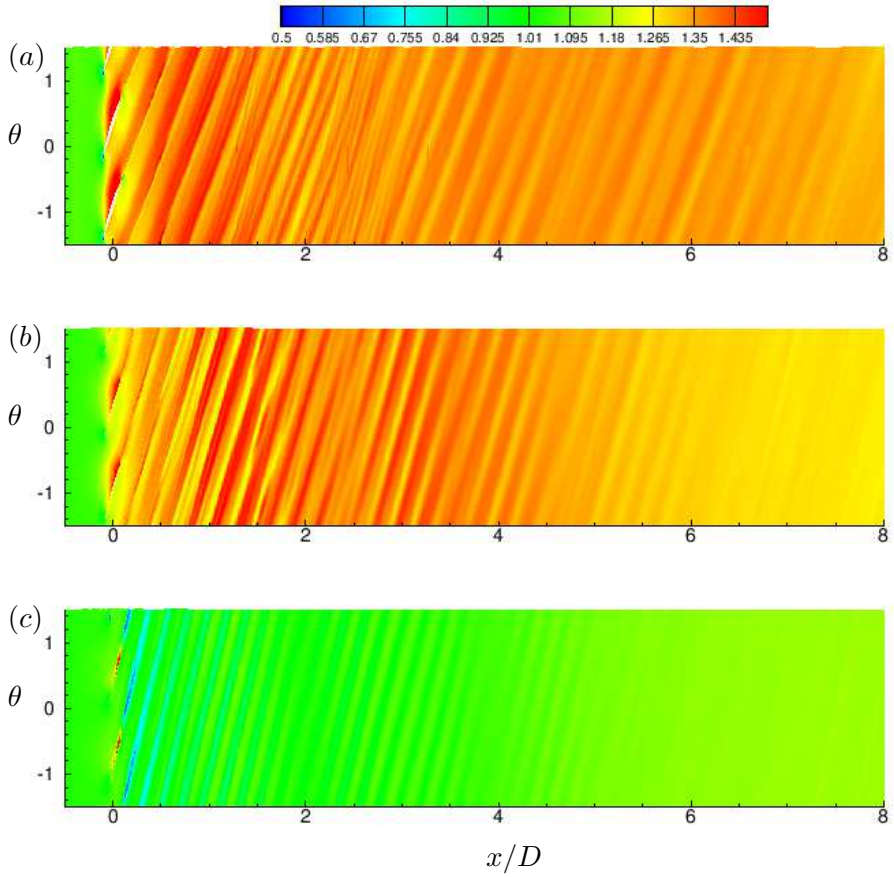

Figure 6.22: Phase-averaged axial velocity in $x\theta$ plane at $r = 0.4R$ (a), $0.7R$ (b) and $0.95R$ (c). The values are normalized with U.

production moves downstream as we move radially outwards.

6.3.4 Azimuthal-averaged propeller wake

In order to analyze the propeller wake, the phase-averaged flow field is further averaged in azimuthal direction to obtain azimuthal-averaged flow features. The inception of tip vortex instabilities creates oscillations in envelope of wake. Felli et al. [77] plotted the standard deviation image calculated over 1000 snapshots in time, which they used to identify the location of instabilities in hub and tip vortices. Figure 6.25(a) shows the azimuthal-averaged wake envelope of the propeller where dark shade shows region where

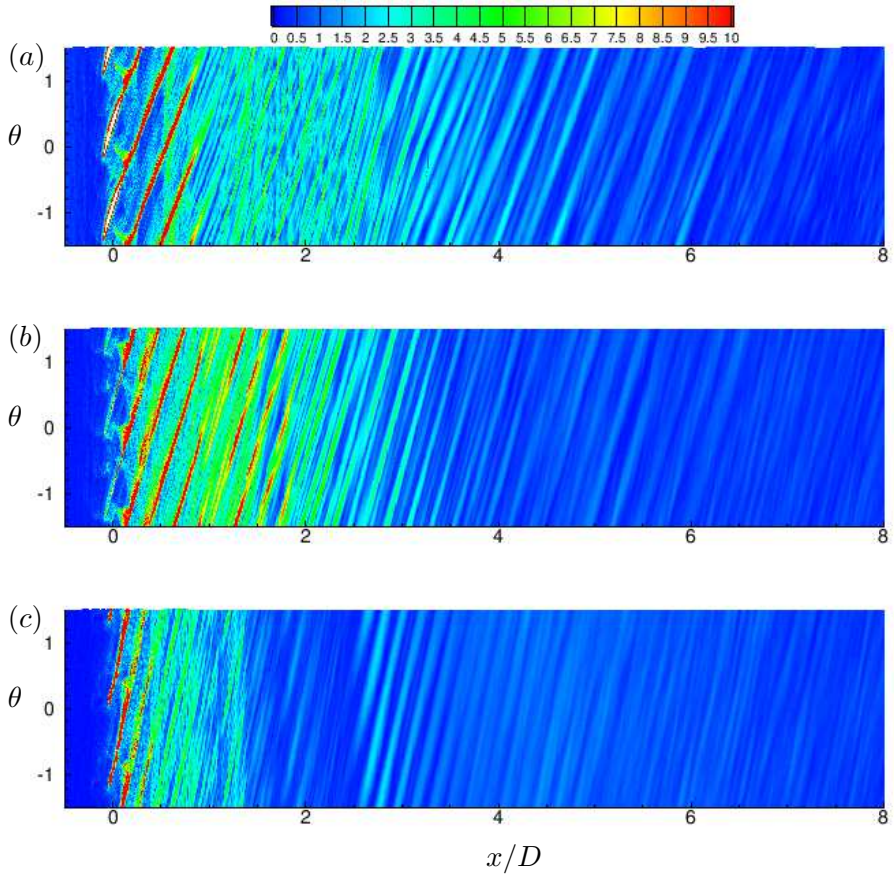

Figure 6.23: Phase-averaged vorticity magnitude in $x\theta$ plane at $r = 0.4R$ (a), $0.7R$ (b) and $0.95R$ (c). The values are normalized appropriately using U and R.

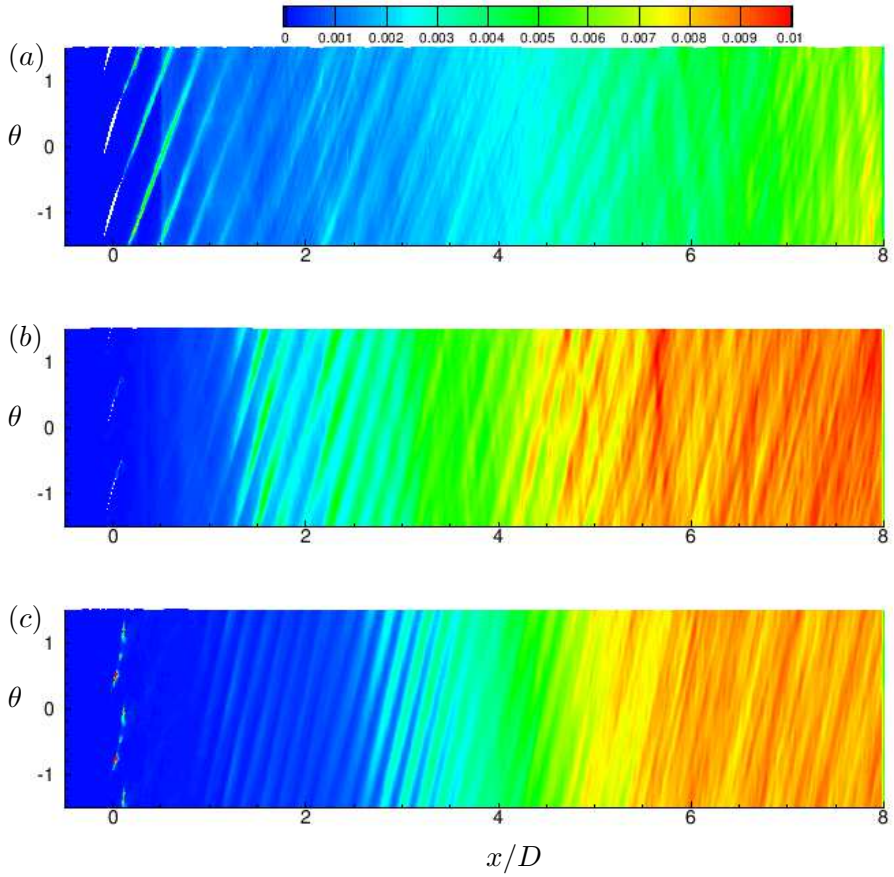

Figure 6.24: Phase-averaged turbulent kinetic energy in $x\theta$ plane at $r = 0.4R$ (a), $0.7R$ (b) and $0.95R$ (c). The values are normalized appropriately using U.

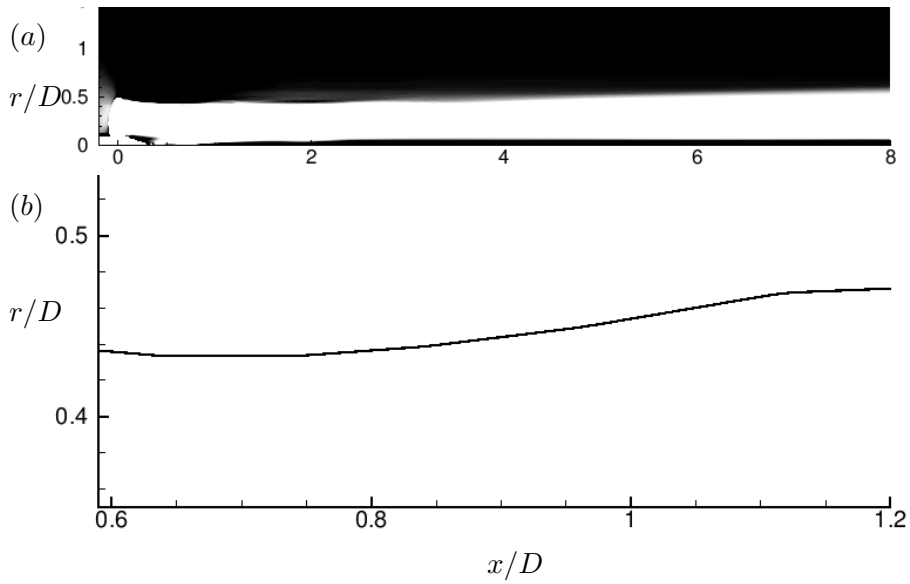

Figure 6.25: (a) The envelope of propeller wake and (b) the line tracing the envelope of propeller wake in the near field.

axial velocity is higher than the freestream velocity. The line tracing the wake envelope is extracted as shown in Figure 6.25(b), where it is plotted in the region of near field. The method used by Felli et al. [77] is applied to get the axial location where the tip vortex destabilizes, which is at $x/D = 0.8$.

Azimuthal-averaged velocity components are shown in Figure 6.26. In the near field, a low axial momentum region is seen, which is created by flow separation on the hub. The radial velocity U_r is very small everywhere in the domain except in the vicinity of the blade where it is negative. This is because the propeller entrains fluid from its surrounding and pushes it downstream. The major difference between streamwise velocity and azimuthal velocity fields is that the maximum of azimuthal velocity at any streamwise location lies in the hub vortex whereas that of streamwise velocity lies around mid span of the propeller. The higher axial velocity around mid span of propeller leads to faster advection of blade wake compared to the tip vortices. This brings the tip vortex of a blade very close to the trailing edge wake of the previous blade (see Figure 6.13). The radial decrease in azimuthal velocity outside hub vortex makes the

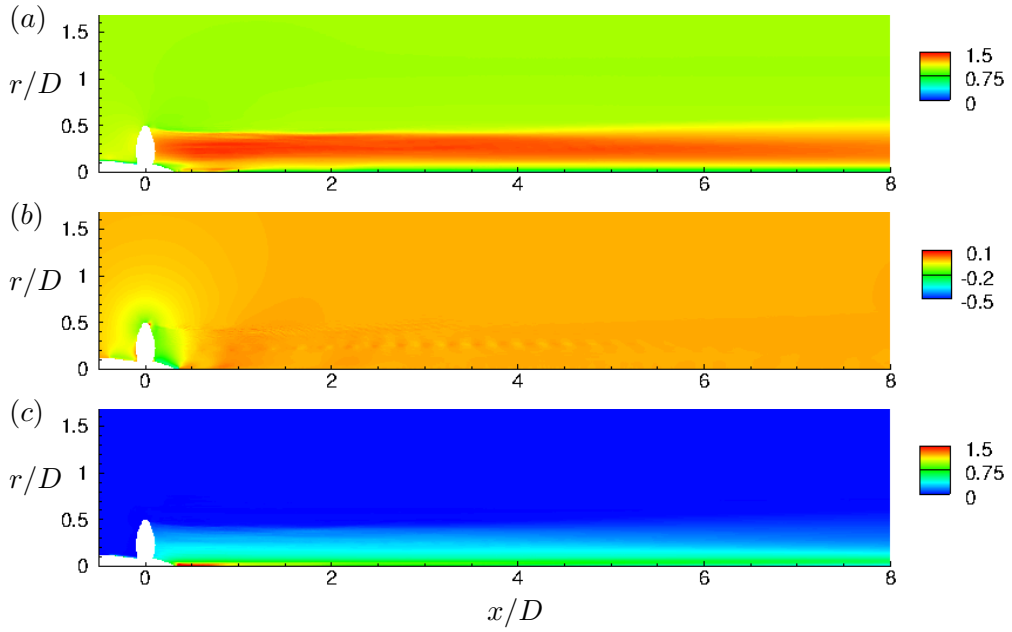

Figure 6.26: Azimuthal-averaged velocity components in xr plane: (a) axial, (b) radial and (c) azimuthal. The values are normalized with U.

blade trailing edge wake rotate faster than tip vortices which are located at the edge of propeller wake. This leads to increase in bending of the blade wakes (see Figure 6.16). All of these phenomena assist in the mutual-inductance mode of instabilities which will be discussed in Section 6.4.

Profiles of velocity components are extracted at 5 locations from $2D$ to $6D$ downstream of the propeller as shown in Figure 6.27. Wake contraction in the near field leads to smaller wake width as compared to propeller radius at $2D$. It is interesting to see that all the profiles overlaps up to $r = 0.2R$ except the profile at $x = 2D$ in the axial velocity. This means the streamwise variation of axial velocity is negligible for $x > 3D$ i.e. in the far field in the inner part of the propeller wake. It can also be seen that as the wake evolves downstream, the profile becomes smoother mainly near the edge of the wake, which signifies diffusion and expansion of wake as one moves from $2D$ to $6D$.

It is interesting to see that the mean axial velocity in the propeller wake is higher than freestream everywhere except in the hub vortex. The azimuthal velocity is zero outside

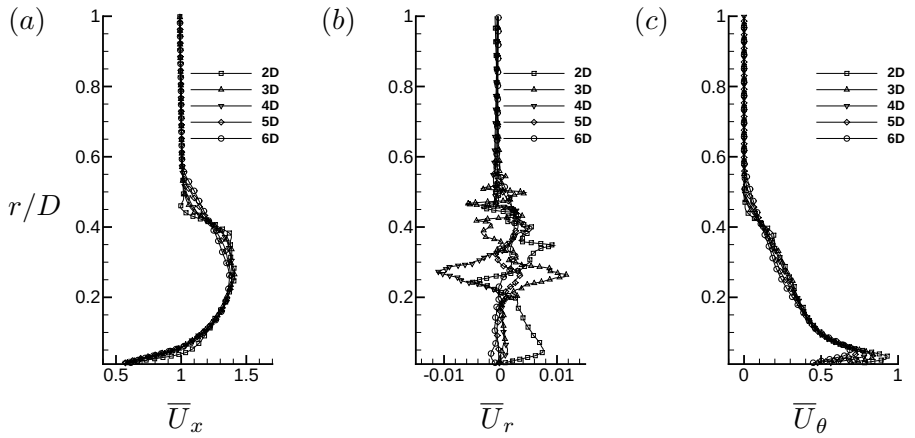

Figure 6.27: Azimuthal-averaged profile of velocity components: (a) axial, (b) radial and (c) azimuthal. The values are normalized appropriately with U.

propeller wake. The fluid column has an angular momentum which decays as we move radially outwards. Thus, the propeller wake can be thought of as a superimposition of swirling velocity along with a high axial momentum surrounding the *wake of hub* which has an axial momentum deficit.

Figure 6.28 shows azimuthal-averaged mean square velocity fluctuation components. The profiles are also extracted at 5 locations from $2D$ to $6D$ downstream of the propeller (Figure 6.29). The streamwise and azimuthal components grow after the tip vortices become unstable whereas the radial fluctuations are very high in the region of stable tip vortex. A possible reason is mutual interaction between adjacent spirals of helical tip vortices which are strongest in the near field. The radial extent of velocity fluctuations grow for all components as we move downstream after the tip vortices become unstable. This is observed clearly in the plots of radial profile of mean square velocity components (Figure 6.29). The axial velocity fluctuations are high in the region of tip vortices (edge of wake) and hub vortex (near axis). The axial velocity fluctuations are nearly constant in the entire wake except in hub and tip vortices. The axial velocity fluctuations remain fairly constant in the hub vortex beyond $x = 3D$. The radial velocity fluctuations show a remarkably different behavior. The radial velocity fluctuations in the hub vortex decay

from $2D$ to $3D$ followed by a subsequent growth. This can be explained as follows. The flow separation on the hub creates a region of high turbulence near end of hub. These high fluctuations in all velocity components undergo viscous dissipation up to $3D$. Till $x = 3D$, the tip vortices break down completely which disturbs the equilibrium of the system containing hub and tip vortices. This causes the hub vortex to oscillate in the radial direction, thus increasing fluctuations in radial component of velocity field. Outside the hub vortex, two peaks are observed in the radial velocity fluctuation profile. These peaks flatten out in the far wake. There is negligible fluctuation in azimuthal velocity component except in the region of hub and tip vortices. The Reynolds stress component $\overline{u'_x u'_r}$ shows higher value in the vicinity of hub and wake edge after the destabilization of tip vortices. The roll-up of blade trailing edge wake in the near wake also increases the value of $\overline{u'_x u'_r}$ as can be seen in the near field. The profiles of $\overline{u'_x u'_r}$ show that its value is negative in hub vortex region where it is positive everywhere else in the wake.

The azimuthal-averaged Reynolds stress is shown in Figure 6.28(d). As evident from the plot, Reynolds stress is maximum near the edge of the wake from $x/D = 1.5$ to 3.5, after that it grows rapidly in radial as well as streamwise direction. Thus, this is the region of intense turbulent production which can be seen in Figure 6.14(b). The radial profiles at 5 streamwise locations downstream of the propeller is also plotted in Figure 6.29(d). The radial expansion of the region of high Reynolds stress is clearly evident. Also, the peak of the Reynolds stress profile decreases in far wake as seen in the profiles from $4D$ to $6D$.

The azimuthal-averaged pressure and mean square pressure fluctuations are shown in Figure 6.30(a) and (b) respectively. The low pressure cores of tip vortices appear as a streak here because of averaging in azimuthal direction. The hub vortex is the region of low pressure and is therefore most susceptible to cavitation. There is negligible streamwise gradient in pressure field beyond $x = 3D$ i.e. in the far wake. The pressure fluctuation shows trend similar to axial and azimuthal velocity fluctuations as discussed earlier. The region inside hub vortex contains large pressure fluctuations. This is also evident from the profiles of pressure fluctuations as shown in Figure 6.31(a). The radial

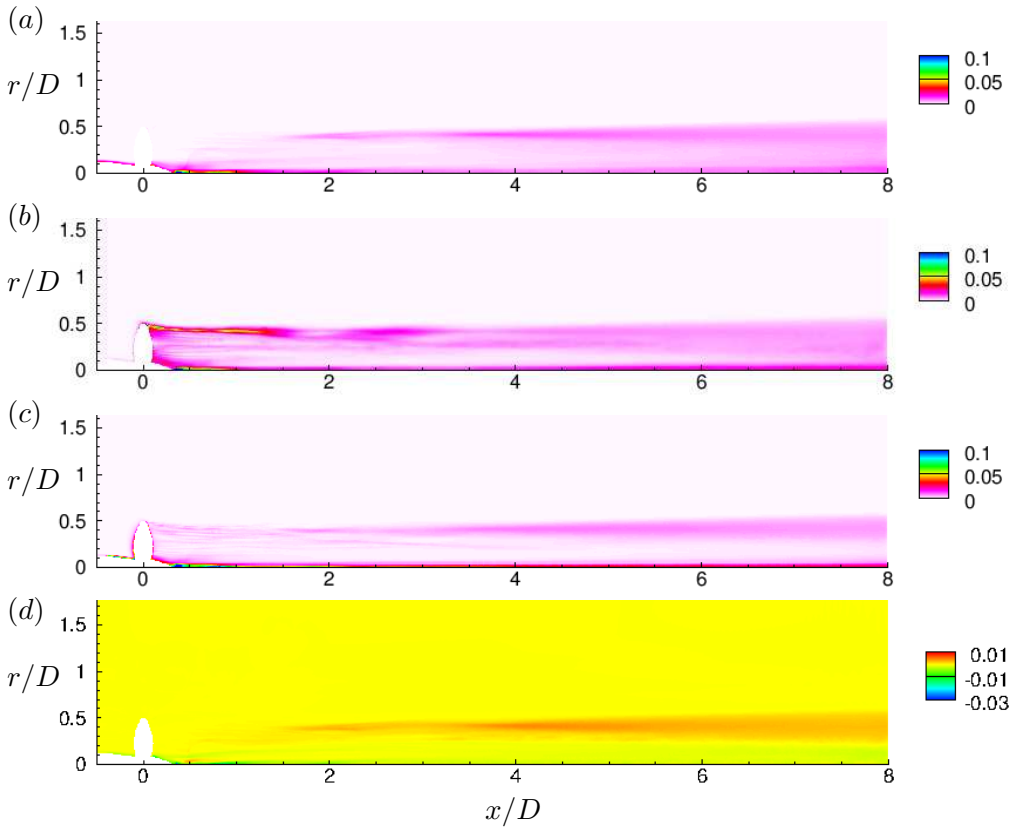

Figure 6.28: Azimuthal-averaged mean square velocity fluctuations in xr plane: (a) axial ($\overline{u'_x u'_x}$), (b) radial ($\overline{u'_r u'_r}$), (c) azimuthal ($\overline{u'_\theta u'_\theta}$) and (d) Reynolds stress ($\overline{u'_x u'_r}$). The values are normalized with U^2.

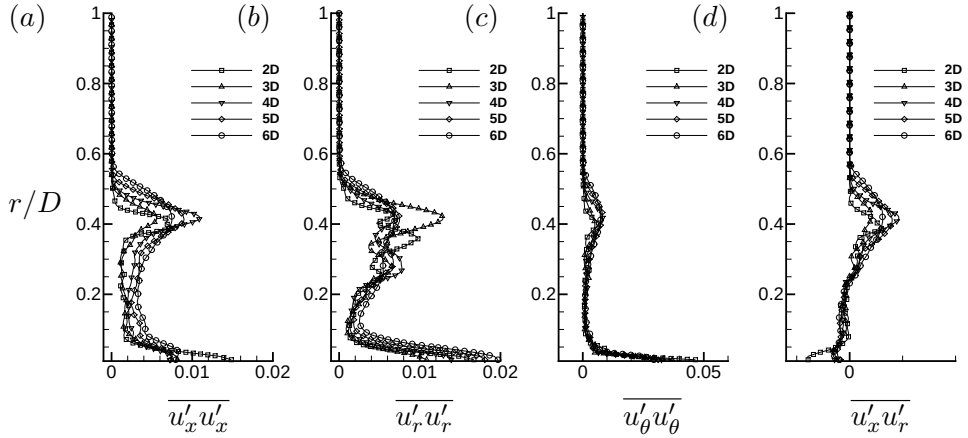

Figure 6.29: Azimuthal-averaged profile of mean square velocity fluctuations: (a) axial ($\overline{u'_x u'_x}$), (b) radial ($\overline{u'_r u'_r}$), (c) azimuthal ($\overline{u'_\theta u'_\theta}$) and (d) Reynolds stress ($\overline{u'_x u'_r}$). The values are normalized with U^2.

extent of high pressure fluctuations near edge of wake increases as the wake expands in the far field. A small region of high pressure fluctuations is seen in near field at $(x/D, r/D) = (0.5, 0.2)$. This seems to be the effect of oscillations in blade trailing edge wake near the root of blades in near field. Overall, the pressure field suggests that the propeller awake away from the blade evolves from near field to far field in a nominal zero pressure gradient environment in axial direction and hence, the far wake in particular can be treated as a column of fluid swirling around an axial hub vortex such that the net axial linear momentum and azimuthal angular momentum are conserved. Hence, the possibility of existence of a self-similar solution in far wake exists.

Figure 6.30(c) shows azimuthal-averaged turbulent kinetic energy. The turbulent kinetic energy is high near end of hub because of fluctuations caused by flow separation on the hub. The magnitude of turbulent kinetic energy decreases rapidly as we move downstream in near axis region in near wake. There is negligible turbulence near edge of the wake in near field due to stable tip vortices as already discussed earlier. The turbulent kinetic energy grows both near axis and near edge of the propeller wake beyond $x/D = 1.5$ following the onset of instabilities in tip vortices. The turbulent kinetic energy grows both in magnitude and radial extent moving further downstream.

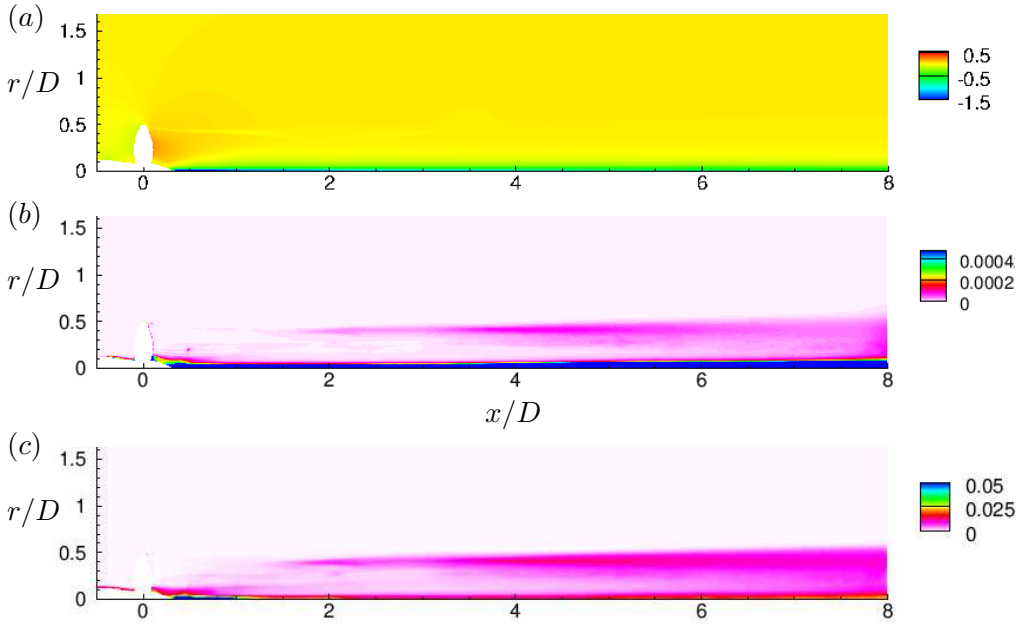

Figure 6.30: Azimuthal-averaged pressure (a), mean square pressure fluctuation (b) and turbulent kinetic energy (c) in xr plane. The values are normalized appropriately using ρU^2.

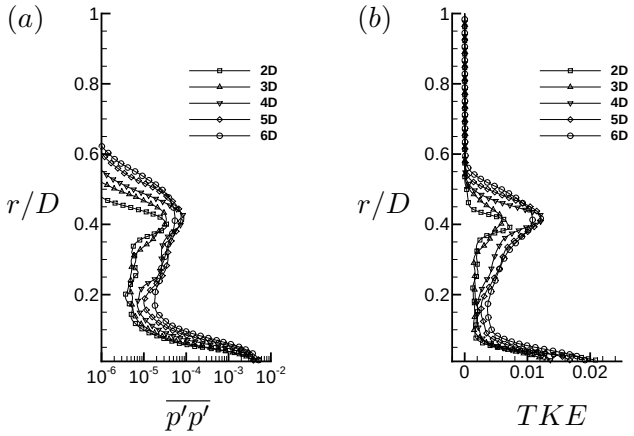

Figure 6.31: Azimuthal-averaged profile of mean square pressure fluctuation (a) and turbulent kinetic energy (b). The values are normalized using ρU^2.

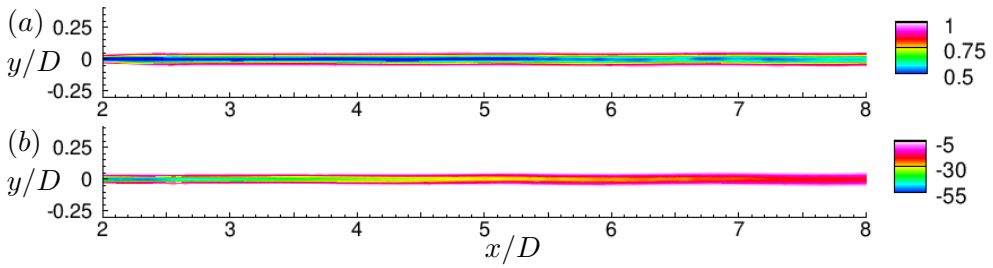

Figure 6.32: Hub vortex: phase-averaged axial velocity (a) and axial vorticity (b) in xy plane. The values are normalized appropriately using U and R.

In general, the turbulent kinetic energy increases in the far wake as seen in radial profile of TKE (Figure 6.31b).

6.3.5 The hub vortex

The hub vortex is an important component of propeller wake which dominates the flow field. The phase-averaged axial velocity and axial vorticity in the hub vortex region is shown in Figure 6.32. Figure 6.33 shows the phase-averaged azimuthal (swirl) velocity at multiple axial locations from 2 to 7 diameters downstream of the propeller. A circle of radius $0.1D$ centered on the axis of propeller is also shown for reference. Both these figures confirm that the hub vortex remains coherent throughout the simulated domain. However, minor oscillations about the propeller axis can be observed mainly beyond $x/D = 4$ (Figure 6.33c-f). Note that the hub vortex is non-axisymmetric. This deviation from axisymmetry increases in far wake. The large values of velocity and pressure fluctuations observed earlier in the hub vortex is the result of azimuthal-averaging of this non-axisymmetric hub vortex.

The radial profiles of azimuthal-averaged velocity and mean square velocity fluctuations discussed earlier (Section 6.3.4) is reproduced in Figure 6.34 with y axis zoomed-in to focus in the region of hub vortex.

The flow field in the hub vortex region shows large axial and azimuthal (swirl) velocities whereas the radial velocity is negligible. Note that the variation in axial velocity is negligible in far field whereas the swirl velocity keeps decreasing with increasing streamwise distance from the propeller. The large swirl velocity is important to the stability of

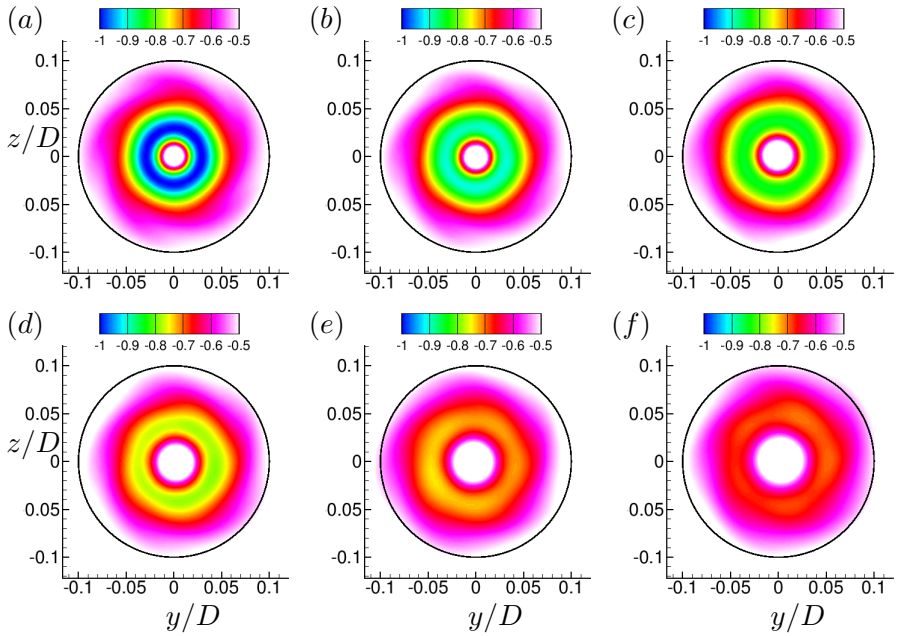

Figure 6.33: Hub vortex: phase-averaged azimuthal (swirl) velocity at $x/D = 2$ (a), 3 (b), 4 (c), 5 (d), 6 (e) and 7 (f) downstream of the propeller. Black solid line is a circle of radius $0.1D$ centered on the axis of propeller.

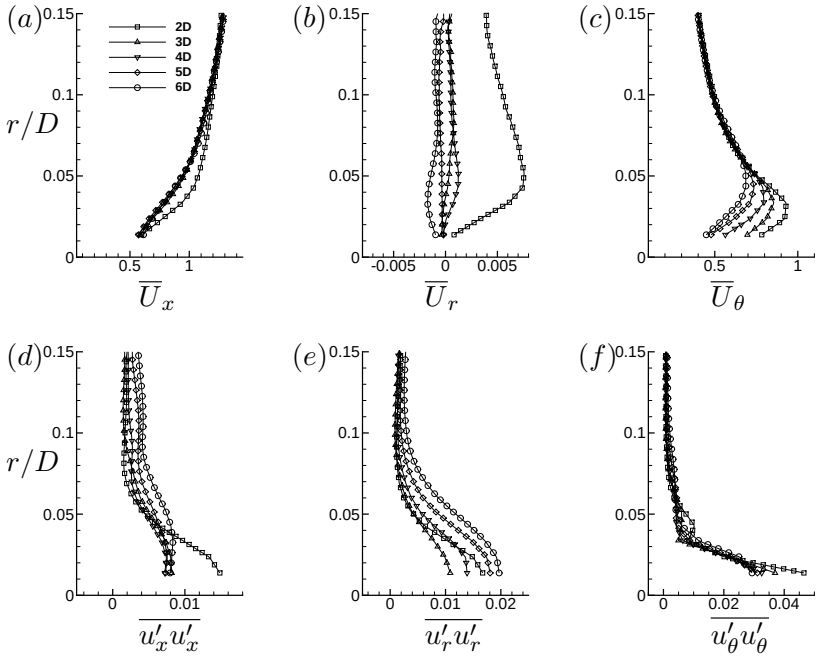

Figure 6.34: Azimuthal-averaged profile of components of velocity (a-c) and mean square velocity fluctuations (d-f) at locations $x/D = 2$, 3, 4, 5 and 6. The values are normalized appropriately using U.

the propeller wake as concluded by Okulov and Sørensen [70], who modeled the hub vortex field by assigning vorticity distribution. They showed that the inclusion of a simple Rankine vortex (to model the hub vortex field) to the Joukowski model could predict the rotor wake rather accurately. Thus, the swirl velocity induced by the hub vortex field stabilizes the otherwise unconditionally unstable Joukowski model. Although the hub vortex field described here is too complicated to be modeled as a simple Rankine vortex, the observed trend is consistent with the analysis of Okulov and Sørensen [70]. The minor oscillations in the hub vortex as discussed earlier cause increase in the azimuthal-averaged fluctuations, as evident in Figure 6.34(d-f). These profiles also show rapid decrease in fluctuations away from the axis in the hub vortex region.

6.4 Mechanisms of propeller wake instabilities

The mutual inductance mode of instability has been suggested to drive the transition to unstable wake in rotors. Experimental investigation of propeller wakes by Felli et al. [77] for a variety of operating conditions and number of blades indicate that the mutual-inductance mode of instability dominates the wake evolution. Nevertheless, short-wave and long-wave mode of instabilities first predicted by Widnall [66] were also observed in their experiments. A number of recent works on wind turbine wakes have also established the dominance of mutual-inductance mode as the prime mechanism for driving the rotor wake instabilities [82–84]. Although the general characteristics of propeller and wind turbine wakes are same i.e. similar hub (and/or root) and tip vortices, there are some important fundamental differences.

Wind turbine rotors are designed to extract energy from the flow and hence, the wind turbine wake has lesser momentum in comparison to freestream unlike propeller wake, which pushes flow downstream increasing momentum. Therefore, the wind turbine wake has maximum axial velocity near the edge of wake. This makes the tip vortex move faster than the weak and thin blade trailing edge wakes. These blade wakes dissipate rapidly in the near field where as the tip vortices come close to each other, making them susceptible to mutual inductance mode of instability through a so called *leap-frogging* mechanism [162, 163]. This leap-frogging mechanism is also observed by Felli et al. [77] mainly for higher loading conditions for four-bladed propeller. As expected, this mechanism is commonly observed for those rotor wakes which have small spiral-to-spiral distance. Thus, increasing the number of blades or decreasing the advance ratio facilitates the leap-frogging mechanism.

In marine propellers however, there are other possible mechanisms of mutual-inductance mode of instabilities. The interaction between tip vortex and adjacent blade wake is highly likely mainly for marine propellers which have higher number of blades. This mechanism is particularly preferred when the spiral-to-spiral distance is large (large advance ratio) i.e. the propeller is not highly loaded. Figure 6.35 illustrates this mechanism of mutual inductance in both axial (xy) and transverse (yz) planes.

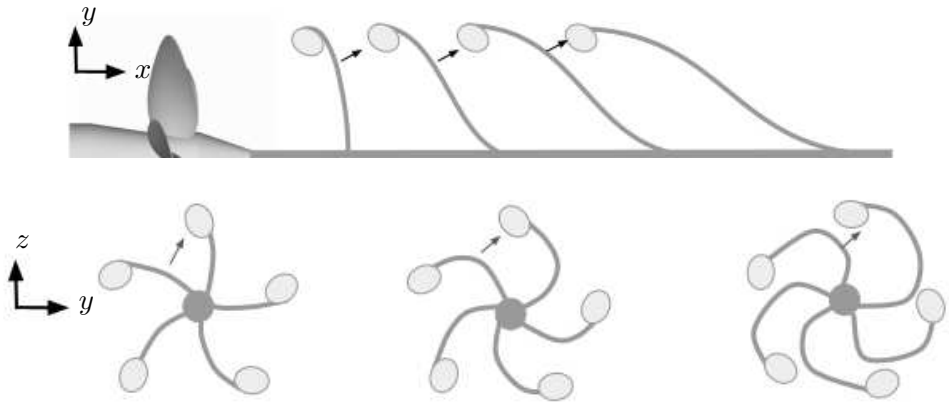

Figure 6.35: Schematic diagram showing mutual interaction between tip vortex and adjacent blade wake in xy (top) and yz (bottom) plane. The flow is from left to right in xy plane (top). The axial evolution is shown in yz plane (bottom) from left to right. The sense of rotation is clockwise in this view.

Another important physical phenomenon which is active in the propeller wake is spiral roll-up of blade trailing edge vortex sheet as mentioned in Section 6.3.2. This phenomenon is responsible for detaching the tip vortices from the blade trailing edge wake after complete roll-up and formation of smaller fragments of trailing edge wake, which eventually dissipate to form far wake as described by Joukowski [64], consisting of only tip and hub vortices. However, as observed by Felli et al. [77], mutual interference between consecutive spirals of tip vortices were much more important than the complete development of the trailing edge wake roll-up. The present case seems different from what has been observed in earlier experiments. As already pointed out earlier, the propeller used in the present simulations is designed to have weaker tip vortices as compared to the propeller used by Felli et al. [77] and others. As the mutual-inductance between tip vortices is not strong, the trailing edge wake get time to undergo roll-up in both axial xy and transverse yz plane. The schematic of roll-up in yz plane is shown in Figure 6.36.

The analysis of Okulov and Sørensen [70] suggested that the occurrence of concentrated tip vortices is the consequence of complete roll-up of the blade trailing edge

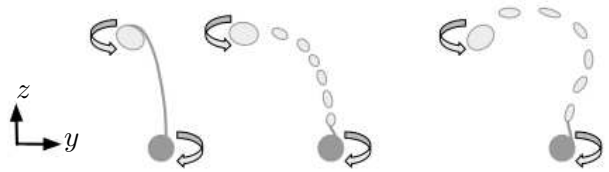

Figure 6.36: Schematic diagram showing blade trailing edge vortex sheet roll-up in yz plane. The arrows show the sense of rotation of the vortices. The axial evolution is shown as we go from left to right.

wake, which subsequently triggers instabilities. This implies that the downstream location where the propeller wake becomes unstable should be independent of number of blades as long as the tip vortex intensity is identical. However, Felli et al. [77] observed that the downstream distance where the propeller wake becomes unstable depends on the number of blades despite having identical tip vortex intensity. They argued that the formation of concentrated tip vortices is more affected by the trailing wake of the blade and the tip vortex of the previous blade.

The propeller wake simulated in the present chapter shows all of the above mentioned phenomenon in some form or other but the mutual-inductance between the rolled-up trailing edge wake and the tip vortices dominates the evolution of propeller wake from near field to far field. Figure 6.37 illustrates this mechanism. The rolling-up of trailing edge wake begins very close to the propeller in the near field. The progressive bending in yz plane (Figure 6.36) and slanting in xy plane facilitates the mutual interaction between smaller vortical structures generated by blade wake roll-up and the tip vortices in the intermediate wake. This mechanism where the roll-up of blade trailing edge wake generates concentrated vortices which subsequently interact with the tip vortices causing wake instability is different from that observed in experiments [73, 77] and is not reported in the literature to the best of our knowledge. This mechanism is expected to be dominant for propellers which generate weaker tip vortices but have higher number of blades.

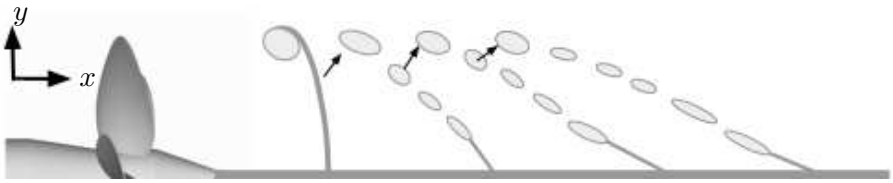

Figure 6.37: Schematic diagram showing blade trailing edge vortex sheet roll-up coupled with mutual interaction between tip vortex and adjacent blade wake in transverse xy plane. Flow is from left to right. The arrows show the mutual interactions.

6.5 Dynamic analysis of the propeller wake

In order to study the dynamics of the propeller wake, the velocity signals are acquired from LES at 30 probe points in the wake, 10 points each at: the axis (hub vortex), $70\%R$ from the axis (mid blade), and $90\%R$ from the axis (tip vortices), where R is the radius of the propeller. The locations of these probes are listed in Table 6.2. Felli et al. [77] computed power spectra of the radial velocity at the edge of the wake and showed that the near field is dominated by the blade frequency followed by the shaft frequency. As one moves downstream, the energy of the blade frequency is transferred to the shaft frequency following complex grouping mechanisms, which depend on the number of blades. They varied the number of blades from 2 to 4 and showed that for all cases, the far wake has a dominant shaft frequency followed by a power-law decay with an exponent of -0.9. A similar power-law exponent is also reported by Muscari et al. [164] in the spectra of kinetic energy obtained from simulations using DES for the same rotor as Felli et al. [77]. In order to separate the effect of periodic forcing due to blade passage, they also report spectra of phase-averaged kinetic energy, which showed -0.9 power-law decay at higher frequencies as well.

Our simulations are performed in the rotating reference frame, hence the probes record phase-average velocity signals everywhere. The phase-averaging purges the effect of forcing due to periodicity and highlights all other effects. The frequency spectra of the phase-averaged radial velocity signals are computed in the same fashion as was described earlier for the force spectra. The frequency is normalized such that the shaft (rotor) frequency is $1rev^{-1}$.

$y/D = 0$		$y/D = 0.35$		$y/D = 0.45$	
Probe	x/D	Probe	x/D	Probe	x/D
H1	0.5	M1	0.2	T1	0.2
H2	0.75	M2	0.4	T2	0.4
H3	1.0	M3	0.6	T3	0.6
H4	1.5	M4	0.8	T4	0.8
H5	2.0	M5	1.0	T5	1.0
H6	3.0	M6	1.5	T6	1.5
H7	4.0	M7	2.0	T7	2.0
H8	5.0	M8	3.0	T8	3.0
H9	6.0	M9	4.0	T9	4.0
H10	7.0	M10	5.0	T10	5.0

Table 6.2: The location of probes in xy plane.

The spectra of phase-averaged radial velocity, in the region of tip vortices, are shown in Figure 6.38. All the signals from T1-T10 show a dominant peak at $1rev^{-1}$, which is the shaft (rotor) frequency as expected. Distinct high frequency peaks appear in the near field spectra (Figure 6.38a) around $100rev^{-1}$ along with higher harmonics. This seems to be related to the complex interactions between the tip vortices and the blade trailing edge wake. Once the tip vortices become unstable and the blade trailing edge wake breaks up into smaller vortices after spiral roll-up (Figure 6.12), these high frequencies are absent as seen in Figure 6.38(b). Also, the energy in the far wake is distributed across more frequencies when compared with the near wake.

The spectra of phase-averaged radial velocity in the mid-blade region (Figure 6.39) show trends similar to those in the tip vortex region. The major difference from the spectra of the tip vortex region is a better collapse of all spectra in the far wake. The radial velocity spectra in the hub vortex region is shown in Figure 6.40. In the near field (H1-H3), the spectra contained higher energy at the frequencies lower than the shaft frequency. This can be attributed to the geometrically induced flow separation on the hub (Figure 6.12a). The energy contained at high frequencies decreases moving downstream and eventually the spectra collapse as seen in Figure 6.40(b).

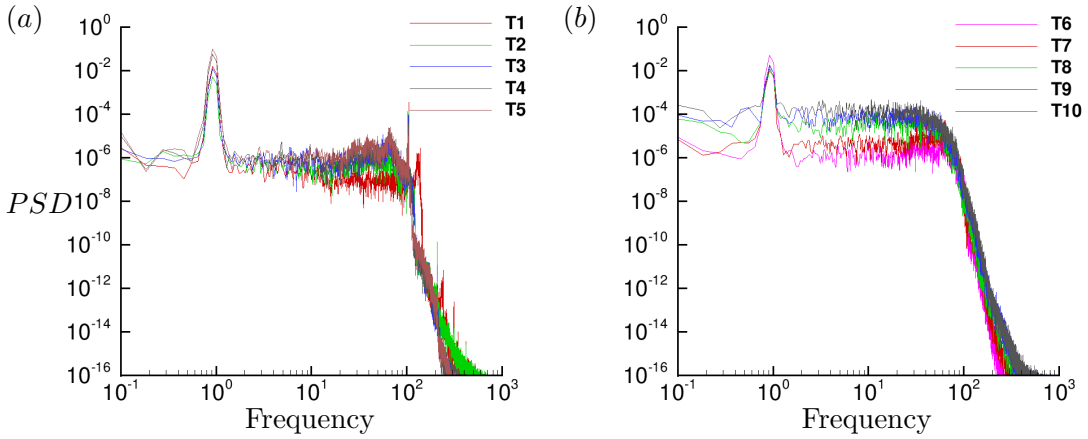

Figure 6.38: PSD of phase-averaged radial velocity at 90%R from the propeller axis: (a) probes T1-T5 and (b) probes T6-T10. See Table 6.2 for coordinates.

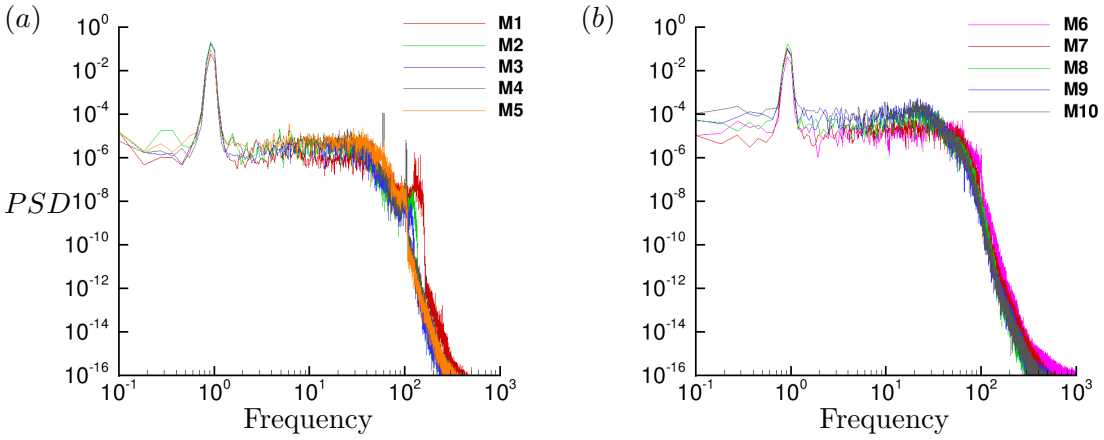

Figure 6.39: PSD of phase-averaged radial velocity at 70%R from the propeller axis: (a) probes M1-M5 and (b) probes M6-M10. See Table 6.2 for coordinates.

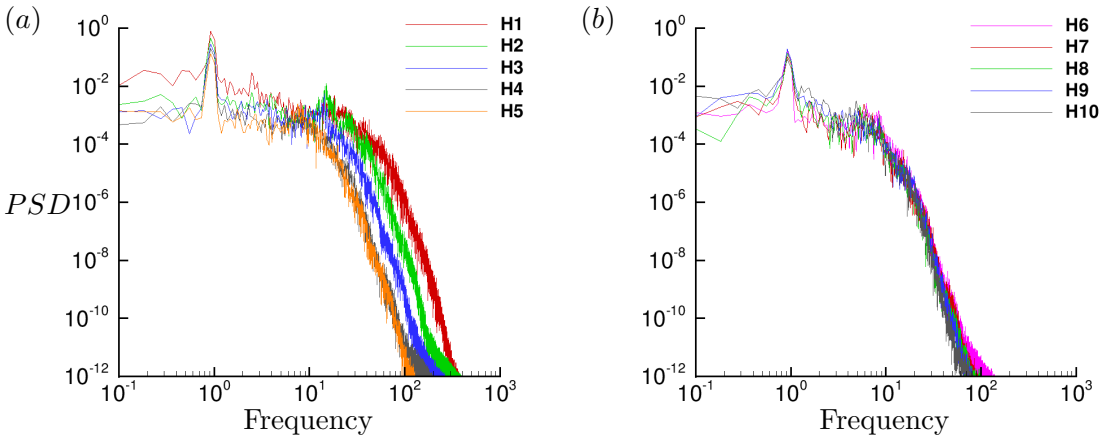

Figure 6.40: PSD of radial velocity on the propeller axis: (a) probes H1-H5 and (b) probes H6-H10. See Table 6.2 for coordinates.

6.6 Summary

Well-resolved LES is used to understand the details of the complex dynamics of the wake of a five-bladed marine propeller at design advance ratio. Care has been taken to resolve important small scales as well as the entire evolution of propeller wake from near field to far field without any confinement effects, which is known to affect propeller wake in general and tip vortex dynamics particularly.

Phase-averaged and azimuthal-averaged flow fields are used to characterize the evolution of the propeller wake from near field to far field. In the near field, the thin blade trailing edge wakes which are generated because of spanwise variation of loading on the propeller blades, undergo dissipation and Kelvin–Helmholtz destabilization leading to roll-up in both axial and transverse plane. This leads to formation of small vortical structures. Although the tip vortices break apart from the blade trailing edge wakes, they still remain stable in near field. Eventually, these tip vortices destabilize due to strong mutual induction between them and small vortical structures formed as a result of roll-up, causing them to oscillate. The nature of mutual inductance is such that the interaction between the blade trailing edge wake and the tip vortex of adjacent blade is stronger than the spiral-to-spiral [77] and tip vortex-adjacent blade wake interactions

[73] observed in earlier experiments.

It is argued that the preferred mechanism of mutual-inductance mode of instabilities in rotor wakes depends on the blade geometry and operating conditions. A propeller designed to have a strong tip vortex will have stronger mutual interactions between adjacent tip vortices. This mechanism is further aided by lower advance ratio and higher number of blades because of decreased spiral-to-spiral distance. On the other hand, a propeller with relatively weaker tip loading will have weaker mutual interactions between the tip vortices. Lower advance ratio further delays this mechanism due to higher spiral-to-spiral distance. Hence, the blade trailing edge wake completes its spiral roll-up forming discrete vortical structures. These vortices being of smaller magnitude than tip vortices, get pulled towards the edge of wake by the tip vortices as the wake evolves in the intermediate field. After becoming unstable, the oscillating vortical structures produce turbulence in the wake. In the far field, the wake can be thought of as a region of high axial and swirl velocity around an oscillating hub vortex. The wake becomes increasingly axisymmetric as it evolves in far field where it appears as a fluid mass swirling around an axial hub vortex. At design advance ratio, the hub vortex remains coherent up to the length of wake captured in our simulations ($8D$). It undergoes some minor oscillations after destabilization of the tip vortices as evident in the increase in radial velocity fluctuations. Almost all of the pressure fluctuations lie in the hub vortex. The further evolution of far wake may follow a self-similar behavior. The axial and azimuthal shear layers in the far wake are susceptible to Kelvin–Helmholtz instabilities.

The dynamics of propeller wakes is studied using point spectra at various locations in the wake. The point spectra of radial velocity are computed at various streamwise locations in the tip vortex, mid blade, and hub vortex regions to analyze the dynamics of the propeller wake. The spectra collapse much better at all radial locations in the far wake than in the near wake.

Bibliography

[1] M. Germano, U. Piomelli, P. Moin, and W. H. Cabot. A dynamic subgrid–scale eddy viscosity model. *Physics of Fluids A*, 3:7:1760, 1991.

[2] D. K. Lilly. A proposed modification of the Germano subgrid–scale closure model. *Physics of Fluids A*, 4:3:633, 1992.

[3] K. Mahesh, G. Constantinescu, and P. Moin. A numerical method for large–eddy simulation in complex geometries. *Journal of Computational Physics*, 197:1:215, 2004.

[4] T. S. Lund, X. Wu, and K. D. Squires. Generation of turbulent inflow data for spatially-developing boundary layer simulations. *Journal of Computational Physics*, 140(2):233–258, 1998.

[5] N. C. Groves, T. T. Huang, and M. S. Chang. *Geometric Characteristics of DARPA suboff models:(DTRC Model Nos. 5470 and 5471)*. David Taylor Research Center, 1989.

[6] D. H. Bridges. A detailed study of the flowfield of a submarine propeller during a crashback maneuver. Technical Report MSSU-ASE-04-1, Department of Aerospace Engineering, Mississippi State University, 2004.

[7] K. Mahesh, P. Kumar, A. Gnanaskandan, and Z. Nitzkorski. LES applied to ship research. *Journal of Ship Research*, 59(4):238–245, 2015.

[8] A. J. Smits, B. J. McKeon, and I. Marusic. High-Reynolds number wall turbulence. *Annual Review of Fluid Mechanics*, 43:353–375, 2011.

[9] J. Piquet and V. C. Patel. Transverse curvature effects in turbulent boundary layer. *Progress in Aerospace Sciences*, 35(7):661–672, 1999.

[10] R. M. Lueptow. Turbulent boundary layer on a cylinder in axial flow. *AIAA Journal*, 28(10):1705–1706, 1990.

[11] L. Landweber. Effect of transverse curvature on frictional resistance. Technical report, David Taylor Model Basin Washington DC, 1949.

[12] H. Schlichting. *Boundary-layer theory*. McGraw-Hill, 1968.

[13] R. A. Seban and R. Bond. Skin–friction and heat-transfer characteristics of a laminar boundary layer on a cylinder in axial incompressible flow. *Journal of the Aeronautical Sciences*, 18(10):671–675, 1951.

[14] H. R. Kelly. A note on the laminar boundary layer on a circular cylinder in axial incompressible flow. *Journal of the Aeronautical Sciences*, 1954.

[15] M. B. Glauert and M. J. Lighthill. The axisymmetric boundary layer on a long thin cylinder. *Proceedings of the Royal Society of London A: Mathematical, Physical and Engineering Sciences*, 230:188–203, 1955.

[16] K. Stewartson. The asymptotic boundary layer on a circular cylinder in axial incompressible flow. *Quarterly of Applied Mathematics*, 13(2):113–122, 1955.

[17] R. L. Richmond. *Experimental Investigation of Thick, Axially Symmetric Boundary Layers on Cylinders at Subsonic and Hypersonic Speeds*. PhD thesis, California Institute of Technology, 1957.

[18] Y. S. Yu. Effects of transverse curvature on turbulent boundary layer characteristics. *Journal of Ship Research*, 3:33–41, 1958.

[19] G. N. V. Rao. The law of the wall in a thick axi-symmetric turbulent boundary layer. *Journal of Applied Mechanics*, 89:237–338, 1967.

[20] T. Cebeci. Laminar and turbulent incompressible boundary layers on slender bodies of revolution in axial flow. *Journal of Basic Engineering*, 92:545–554, 1970.

[21] G. N. V. Rao and N. R. Keshavan. Axisymmetric turbulent boundary layers in zero pressure-gradient flows. *Journal of Applied Mechanics*, 39(1):25–32, 1972.

[22] D. M. Chase. Mean velocity profile of a thick turbulent boundary layer along a circular cylinder. *AIAA Journal*, 10(7):849–850, 1972.

[23] V. C. Patel. A simple integral method for the calculation of thick axisymmetric turbulent boundary layers. *The Aeronautical Quarterly*, 25(1):47–58, 1974.

[24] V. C. Patel, A. Nakayama, and R. Damian. Measurements in the thick axisymmetric turbulent boundary layer near the tail of a body of revolution. *Journal of Fluid Mechanics*, 63(2):345–367, 1974.

[25] W. W. Willmarth, R. E. Winkel, L. K. Sharma, and T. J. Bogar. Axially symmetric turbulent boundary layers on cylinders: Mean velocity profiles and wall pressure fluctuations. *Journal of Fluid Mechanics*, 76(01):35–64, 1976.

[26] R. E. Luxton, M. K. Bull, and S. Rajagopalan. The thick turbulent boundary layer on a long fine cylinder in axial flow. *Aeronautical Journal*, 88:186–199, 1984.

[27] R. M. Lueptow, P. Leehey, and T. Stellinger. The thick, turbulent boundary layer on a cylinder: Mean and fluctuating velocities. *Physics of Fluids (1958-1988)*, 28 (12):3495–3505, 1985.

[28] M. H. Krane, L. M. Grega, and T. Wei. Measurements in the near-wall region of a boundary layer over a wall with large transverse curvature. *Journal of Fluid Mechanics*, 664:33–50, 2010.

[29] N. Afzal and R. Narasimha. Axisymmetric turbulent boundary layer along a circular cylinder at constant pressure. *Journal of Fluid Mechanics*, 74(01):113–128, 1976.

[30] O. R. Tutty. Flow along a long thin cylinder. *Journal of Fluid Mechanics*, 602: 1–37, 2008.

[31] S. A. Jordan. Axisymmetric turbulent statistics of long slender circular cylinders. *Physics of Fluids (1994-present)*, 23(7):075105, 2011.

[32] S. A. Jordan. A skin friction model for axisymmetric turbulent boundary layers along long thin circular cylinders. *Physics of Fluids (1994-present)*, 25(7):075104, 2013.

[33] S. A. Jordan. On the axisymmetric turbulent boundary layer growth along long thin circular cylinders. *Journal of Fluids Engineering*, 136(5):051202, 2014.

[34] S. A. Jordan. A simple model of axisymmetric turbulent boundary layers along long thin circular cylinders. *Physics of Fluids (1994-present)*, 26(8):085110, 2014.

[35] H. H. Fernholz and D. Warnack. The effects of a favourable pressure gradient and of the Reynolds number on an incompressible axisymmetric turbulent boundary layer. Part 1. the turbulent boundary layer. *Journal of Fluid Mechanics*, 359: 329–356, 1998.

[36] D. Warnack and H. H. Fernholz. The effects of a favourable pressure gradient and of the Reynolds number on an incompressible axisymmetric turbulent boundary layer. Part 2. the boundary layer with relaminarization. *Journal of Fluid Mechanics*, 359:357–381, 1998.

[37] N. Afzal. Analysis of a turbulent boundary layer subjected to a strong adverse pressure gradient. *International Journal of Engineering Science*, 21(6):563–576, 1983.

[38] N. Afzal. Turbulent boundary layer with negligible wall stress. *Journal of Fluids Engineering*, 130(5):051205, 2008.

[39] T. Wei and J. Klewicki. Scaling properties of the mean wall-normal velocity in zero-pressure-gradient boundary layers. *Physical Review Fluids*, 1(8):082401, 2016.

[40] T. Wei, Y. Maciel, and J. Klewicki. Integral analysis of boundary layer flows with pressure gradient. *Physical Review Fluids*, 2(9):092601, 2017.

[41] J. Rotta. On the theory of the turbulent boundary layer. *NACA Technical Memorandum, No. 1344*, 1953.

[42] F. H. Clauser. Turbulent boundary layers in adverse pressure gradients. *Journal of the Aeronautical Sciences*, 21(2):91–108, 1954.

[43] H. Oertel Jr. Wakes behind blunt bodies. *Annual Review of Fluid Mechanics*, 22 (1):539–562, 1990.

[44] A. A. Townsend. *The structure of turbulent shear flow*. Cambridge University Press, 1956.

[45] S. B. Pope. *Turbulent flows*. Cambridge University Press, 2001.

[46] T. Huang, H. L. Liu, N. Grooves, T. Forlini, J. Blanton, and S. Gowing. Measurements of flows over an axisymmetric body with various appendages in a wind tunnel: the DARPA SUBOFF experimental program. In *Proceedings of the 19th Symposium on Naval Hydrodynamics*, 1992.

[47] J. M. Jiménez, M. Hultmark, and A. J. Smits. The intermediate wake of a body of revolution at high Reynolds numbers. *Journal of Fluid Mechanics*, 659:516–539, 2010.

[48] J. M. Jiménez, R. T. Reynolds, and A. J. Smits. The effects of fins on the intermediate wake of a submarine model. *Journal of Fluids Engineering*, 132(3): 031102, 2010.

[49] C. Yang and R. Löhner. Prediction of flows over an axisymmetric body with appendages. In *The 8th International Conference on Numerical Ship Hydrodynamics, Busan, Korea*, 2003.

[50] S.-E. Kim, B. J. Rhee, and R. W. Miller. Anatomy of turbulent flow around DARPA SUBOFF body in a turning maneuver using high-fidelity RANS computations. *International Shipbuilding Progress*, 60(1):207–231, 2013.

[51] N. Alin, R. E. Bensow, C. Fureby, T. Huuva, and U. Svennberg. Current capabilities of DES and LES for submarines at straight course. *Journal of Ship Research*, 54(3):184–196, 2010.

[52] G. Vaz, S. Toxopeus, and S. Holmes. Calculation of manoeuvring forces on submarines using two viscous-flow solvers. In *Proceedings of the 29th International Conference on Ocean, Offshore and Arctic Engineering, Shanghai, China*, 2010.

[53] N. Chase and P. M. Carrica. Submarine propeller computations and application to self-propulsion of DARPA Suboff. *Ocean Engineering*, 60:68–80, 2013.

[54] N. Chase, T. Michael, and P. M. Carrica. Overset simulation of a submarine and propeller in towed, self-propelled and maneuvering conditions. *International Shipbuilding Progress*, 60(1-4):171–205, 2013.

[55] A. Posa and E. Balaras. A numerical investigation of the wake of an axisymmetric body with appendages. *Journal of Fluid Mechanics*, 792:470–498, 2016.

[56] J. K. Eaton and J. P. Johnston. A review of research on subsonic turbulent flow reattachment. *AIAA Journal*, 19(9):1093–1100, 1981.

[57] H. Le, P. Moin, and J. Kim. Direct numerical simulation of turbulent flow over a backward-facing step. *Journal of Fluid Mechanics*, 330:349–374, 1997.

[58] J. Dandois, E. Garnier, and P. Sagaut. Numerical simulation of active separation control by a synthetic jet. *Journal of Fluid Mechanics*, 574:25–58, 2007.

[59] F. Stella, N. Mazellier, and A. Kourta. Scaling of separated shear layers: an investigation of mass entrainment. *Journal of Fluid Mechanics*, 826:851–887, 2017.

[60] T. T. Huang, N. Santelli, and G. Belt. Stern boundary-layer flow on axisymmetric bodies. In *12th Symposium on Naval Hydrodynamics, Washington D.C., USA*, pages 125–167, 1978.

[61] V. C. Patel and Y. T. Lee. Calculation of thick boundary layer and near wake of bodies of revolution by a differential method. In *12th Symposium on Naval Hydrodynamics, Washington D.C., USA*, 1978.

[62] V. C. Patel, Y. T. Lee, and O. Güven. Measurements in the thick axisymmetric turbulent boundary layer and the near wake of a low-drag body of revolution. In *Turbulent Shear Flows I*, pages 137–153. Springer, 1979.

[63] A. Mariotti and G. Buresti. Experimental investigation on the influence of boundary layer thickness on the base pressure and near-wake flow features of an axisymmetric blunt-based body. *Experiments in Fluids*, 54(11):1–16, 2013.

[64] N. E. Joukowski. Vortex theory of screw propeller. *Trudy Otdeleniya Fizicheskikh Nauk Obshchestva Lubitelei Estestvoznaniya*, 16(1):1–31, 1912. (in Russian).

[65] H. Levy and A. G. Forsdyke. The steady motion and stability of a helical vortex. *Proceedings of the Royal Society of London. Series A, Containing Papers of a Mathematical and Physical Character*, pages 670–690, 1928.

[66] S. E. Widnall. The stability of a helical vortex filament. *Journal of Fluid Mechanics*, 54(04):641–663, 1972.

[67] B. P. Gupta and R. G. Loewy. Theoretical analysis of the aerodynamic stability of multiple, interdigitated helical vortices. *AIAA journal*, 12(10):1381–1387, 1974.

[68] V. L. Okulov. On the stability of multiple helical vortices. *Journal of Fluid Mechanics*, 521:319–342, 2004.

[69] L. J. Vermeer, J. N. Sørensen, and A. Crespo. Wind turbine wake aerodynamics. *Progress in Aerospace Sciences*, 39(6):467–510, 2003.

[70] V. L. Okulov and J. N. Sørensen. Stability of helical tip vortices in a rotor far wake. *Journal of Fluid Mechanics*, 576:1–25, 2007.

[71] A. Stella, G. Guj, F. Di Felice, and M. Elefante. Propeller wake evolution analysis by ldv. In *Proc of 22nd Symposium on Naval Hydrodynamics, Washington DC*, pages 171–188, 1998.

[72] A. Stella, G. Guj, and F. Di Felice. Propeller wake flowfield analysis by means of ldv phase sampling techniques. *Experiments in Fluids*, 28(1):1–10, 2000.

[73] F. Di Felice, D. Di Florio, M. Felli, and G. P. Romano. Experimental investigation of the propeller wake at different loading conditions by particle image velocimetry. *Journal of Ship Research*, 48(2):168–190, 2004.

[74] S. J. Lee, B. G. Paik, J. H. Yoon, and C. M. Lee. Three-component velocity field measurements of propeller wake using a stereoscopic piv technique. *Experiments in Fluids*, 36(4):575–585, 2004.

[75] M. Felli, F. Di Felice, G. Guj, and R. Camussi. Analysis of the propeller wake evolution by pressure and velocity phase measurements. *Experiments in Fluids*, 41(3):441–451, 2006.

[76] M. Felli, G. Guj, and R. Camussi. Effect of the number of blades on propeller wake evolution. *Experiments in Fluids*, 44(3):409–418, 2008.

[77] M. Felli, R. Camussi, and F. Di Felice. Mechanisms of evolution of the propeller wake in the transition and far fields. *Journal of Fluid Mechanics*, 682:5–53, 2011.

[78] J. Stack, F. X. Caradonna, and Ö. Savas. Flow visualizations and extended thrust time histories of rotor vortex wakes in descent. *Journal of the American Helicopter Society*, 50(3):279–288, 2005.

[79] C. V. Ohanian, G. J. McCauley, and Ö. Savas. A visual study of vortex instabilities in the wake of a rotor in hover. *Journal of the American Helicopter Society*, 57 (4):1–8, 2012.

[80] R. B. Green, E. A. Gillies, and R. E. Brown. The flow field around a rotor in axial descent. *Journal of Fluid Mechanics*, 534:237–261, 2005.

[81] G. V. Iungo, F. Viola, S. Camarri, F. Porté-Agel, and F. Gallaire. Linear stability analysis of wind turbine wakes performed on wind tunnel measurements. *Journal of Fluid Mechanics*, 737:499–526, 2013.

[82] M. Sherry, A. Nemes, D. Lo Jacono, H. M. Blackburn, and J. Sheridan. The interaction of helical tip and root vortices in a wind turbine wake. *Physics of Fluids (1994-present)*, 25(11):117102, 2013.

[83] M. Sherry, J. Sheridan, and D. Lo Jacono. Characterisation of a horizontal axis wind turbines tip and root vortices. *Experiments in Fluids*, 54(3):1–19, 2013.

[84] S. Sarmast, R. Dadfar, R. F. Mikkelsen, P. Schlatter, S. Ivanell, J. N. Sørensen, and D. S. Henningson. Mutual inductance instability of the tip vortices behind a wind turbine. *Journal of Fluid Mechanics*, 755:705–731, 2014.

[85] A. Nemes, D. Lo Jacono, H. M. Blackburn, and J. Sheridan. Mutual inductance of two helical vortices. *Journal of Fluid Mechanics*, 774:298–310, 2015.

[86] H. U. Quaranta, H. Bolnot, and T. Leweke. Long-wave instability of a helical vortex. *Journal of Fluid Mechanics*, 780:687–716, 2015.

[87] J. E. Kerwin. Marine propellers. *Annual review of Fluid mechanics*, 18(1):367–403, 1986.

[88] F. Di Felice, M. Felli, M. Liefvendahl, and U. Svennberg. Numerical and experimental analysis of the wake behavior of a generic submarine propeller. In *First International Symposium on Marine Propulsors, Trondheim, Norway*, 2009.

[89] A. Di Mascio, R. Muscari, and G. Dubbioso. On the wake dynamics of a propeller operating in drift. *Journal of Fluid Mechanics*, 754:263–307, 2014.

[90] D.-G. Baek, H.-S. Yoon, J.-H. Jung, K.-S. Kim, and B.-G. Paik. Effects of the advance ratio on the evolution of a propeller wake. *Computers & Fluids*, 118: 32–43, 2015.

[91] E. Balaras, S. Schroeder, and A. Posa. Large-eddy simulations of submarine propellers. *Journal of Ship Research*, 59(4):227–237, 2015.

[92] M. Vyšohlid and K. Mahesh. Large eddy simulation of crashback in marine propellers. In *Proceedings of the 26th Symposium on Naval Hydrodynamics, Rome, Italy*, 2006.

[93] P. Chang, M. Ebert, Y. L. Young, Z. Liu, K. Mahesh, H. Jang, and M. Shearer. Propeller forces and structural responses to crashback. In *Proceedings of the 27th Symposium on Naval Hydrodynamics, Seoul, Korea*, 2008.

[94] H. Jang and K. Mahesh. Large eddy simulation of ducted propulsors in crashback. In *Proceedings of the 27th Symposium on Naval Hydrodynamics, Seould, Korea*, 2008.

[95] H. Jang and K. Mahesh. Large eddy simulation of crashback in ducted propulsors with stator blades. In *Proceedings of the 29th Symposium on Naval Hydrodynamics, Gothenburg, Sweden*, 2012.

[96] A. Verma, H. Jang, and K. Mahesh. The effect of an upstream hull on a propeller in reverse rotation. *Journal of Fluid Mechanics*, 704:61–88, 2012.

[97] H. Jang, A. Verma, and K. Mahesh. Predicting unsteady loads in marine propulsor crashback using large eddy simulation. *International Journal of Rotating Machinery*, 2012, 2012.

[98] H. Jang and K. Mahesh. Large eddy simulation of flow around a reverse rotating propeller. *Journal of Fluid Mechanics*, 729:151–179, 2013.

[99] P. Kumar and K. Mahesh. Analysis of marine propulsor in crashback using large eddy simulation. In *Fourth International Symposium on Marine Propulsors, Austin, USA*, 2015.

[100] P. Kumar and K. Mahesh. Towards large eddy simulation of hull-attached propeller in crashback. In *Proceedings of the 31st Symposium on Naval Hydrodynamics, Monterey, USA*, 2016.

[101] S. Jessup, C. Chesnakas, D. Fry, M. Donnelly, S. Black, and J. Park. Propeller performance at extreme off design conditions. In *Proceedings of the 25$^{\text{th}}$ Symposium on Naval Hydrodynamics, St. John's, Canada*, 2004.

[102] H. Jang. *Large eddy simulation of Crashback in marine propulsors*. PhD thesis, University of Minnesota, 2011.

[103] M. Beddhu, L. K. Taylor, and D. L. Whitfield. Strong conservative form of the incompressible Navier–Stokes equations in a rotating frame with a solution procedure. *Journal of Computational Physics*, 128:427, 1996.

[104] K. S. Majety. *Solutions to the Navier–Stokes equations in non–inertial reference frame*. PhD thesis, Mississippi State University, 2003.

[105] S. Ghosal and P. Moin. The basic equations for the large eddy simulation of turbulent flows in complex geometry. *Journal of Computational Physics*, 118: 24–37, 1995.

[106] J. Gullbrand. Grid-independent large-eddy simulation in turbulent channel flow using three-dimensional explicit filtering. *Annual Research Briefs, Center for Turbulence Research, Stanford Univ.*, 2002.

[107] J. Smagorinsky. General circulation experiments with the primitive equations: I. The basic experiment. *Monthly Weather Review*, 91:99, 1963.

[108] T. S. Lund, S. Ghosal, and P. Moin. Numerical simulations with highly variable eddy viscosity models. *Engineering Applications of Large Eddy Simulations, ASME*, 162:7–11, 1993.

[109] S. Ghosal, T. S. Lund, P. Moin, and K. Akselvoll. A dynamic localization model for large-eddy simulation of turbulent flows. *Journal of Fluid Mechanics*, 286:229, 1995.

[110] C. Meneveau, T. S. Lund, and W. H. Cabot. A Lagrangian dynamic subgrid-scale model of turbulence. *Journal of Fluid Mechanics*, 319:353, 1996.

[111] C. Meneveau and T. S. Lund. On the Lagrangian nature of the turbulence energy cascade. *Physics of Fluids*, 6:2820, 1994.

[112] J. I. Choi, K. Yeo, and C. Lee. Lagrangian statistics in turbulent channel flow. *Physics of Fluids*, 16:779, 2004.

[113] N. Park and K. Mahesh. Reduction of the Germano-identity error in the dynamic Smagorinsky model. *Physics of Fluids (1994-present)*, 21(6):065106, 2009.

[114] A. Verma and K. Mahesh. A Lagrangian subgrid-scale model with dynamic estimation of Lagrangian time scale for large eddy simulation of complex flows. *Physics of Fluids (1994-present)*, 24(8):085101, 2012.

[115] R. Anderson and C. Meneveau. Effects of the similarity model in finite-difference LES of isotropic turbulence using a Lagrangian dynamic mixed model. *Flow, Turbulence and Combustion*, 62:3:201–225, 1999.

[116] F. Sarghini, U. Piomelli, and E. Balaras. Scale-similar models for large-eddy simulations. *Physics of Fluids*, 11:6:1596–1607, 1999.

[117] R. Stoll and F. Porté-Agel. Dynamic subgrid-scale models for momentum and scalar fluxes in large-eddy simulations of neutrally stratified atmospheric boundary layers over heterogeneous terrain. *Water Resources Research*, 42:W01409, 2006.

[118] A. Verma. *Large eddy simulation of high Reynolds number complex flows*. PhD thesis, University of Minnesota, 2012.

[119] S. Muppidi and K. Mahesh. Study of trajectories of jets in crossflow using direct numerical simulations. *Journal of Fluid Mechanics*, 530:81–100, 2005.

[120] S. Muppidi and K. Mahesh. Direct numerical simulation of round turbulent jets in crossflow. *Journal of Fluid Mechanics*, 574:59–84, 2007.

[121] S. Muppidi and K. Mahesh. Direct numerical simulation of passive scalar transport in transverse jets. *Journal of Fluid Mechanics*, 598:335–360, 2008.

[122] R. Sau and K. Mahesh. Passive scalar mixing in vortex rings. *Journal of Fluid Mechanics*, 582:449–461, 2007.

[123] R. Sau and K. Mahesh. Dynamics and mixing of vortex rings in crossflow. *Journal of Fluid Mechanics*, 604:389–409, 2008.

[124] R. Sau and K. Mahesh. Optimization of pulsed jets in crossflow. *Journal of Fluid Mechanics*, 653:365–390, 2010.

[125] P. S. Iyer and K. Mahesh. A numerical study of shear layer characteristics of low-speed transverse jets. *Journal of Fluid Mechanics*, 790:275–307, 2016.

[126] M. A. Regan and K. Mahesh. Global linear stability analysis of jets in cross-flow. *Journal of Fluid Mechanics*, 828:812–836, 2017.

[127] P. A. Chang, A. Vargas, D. Lummer, M. Jiang, and K. Mahesh. Fully-resolved LES of weakly separated flows. In *20th AIAA Computational Fluid Dynamics Conference*. AIAA, 2011.

[128] P. Kumar and K. Mahesh. Large eddy simulation of flow over an axisymmetric body of revolution. *Journal of Fluid Mechanics*, 2017. (submitted).

[129] F. H. Harlow and J. E. Welch. Numerical calculation of time-dependent viscous incompressible flow of fluid with free-stream. *Physics of Fluids*, 8:2182–2189, 1965.

[130] URL https://computation.llnl.gov/casc/hypre/software.html.

[131] P. R. Spalart. Direct simulation of a turbulent boundary layer up to $R_\theta = 1410$. *Journal of Fluid Mechanics*, 187:61–98, 1988.

[132] P. Schlatter and R. Örlü. Assessment of direct numerical simulation data of turbulent boundary layers. *Journal of Fluid Mechanics*, 659:116–126, 2010.

[133] J. Jiménez, S. Hoyas, M. P. Simens, and Y. Mizuno. Turbulent boundary layers and channels at moderate Reynolds numbers. *Journal of Fluid Mechanics*, 657: 335–360, 2010.

[134] P. A. Monkewitz, K. A. Chauhan, and H. M. Nagib. Comparison of mean flow similarity laws in zero pressure gradient turbulent boundary layers. *Physics of Fluids (1994-present)*, 20(10):105102, 2008.

[135] M. P. Simens, J. Jiménez, S. Hoyas, and Y. Mizuno. A high-resolution code for turbulent boundary layers. *Journal of Computational Physics*, 228(11):4218–4231, 2009.

[136] M. J. Woods. *Computation of axial and near-axial flow over a long circular cylinder*. PhD thesis, University of Adelaide, Australia, 2006.

[137] S. Monte, P. Sagaut, and T. Gomez. Analysis of turbulent skin friction generated in flow along a cylinder. *Physics of Fluids (1994-present)*, 23(6):065106, 2011.

[138] Y. Maciel, K.-S. Rossignol, and J. Lemay. Self-similarity in the outer region of adverse-pressure-gradient turbulent boundary layers. *AIAA Journal*, 44(11): 2450–2464, 2006.

[139] R. Narasimha and K. R. Sreenivasan. Relaminarization in highly accelerated turbulent boundary layers. *Journal of Fluid Mechanics*, 61(3):417–447, 1973.

[140] B. E. Launder. Laminarization of the turbulent boundary layer in a severe acceleration. *Journal of Applied Mechanics*, 31(4):707–708, 1964.

[141] J. C. R. Hunt, A. A. Wray, and P. Moin. Eddies, streams, and convergence zones in turbulent flows. *Center for Turbulence Research Report CTR-S88*, page 193, 1988.

[142] P. Kumar and K. Mahesh. Analysis of axisymmetric boundary layers. *arXiv preprint arXiv:1801.04258*, 2018.

[143] S. J. Kline, W. C. Reynolds, F. A. Schraub, and P. W. Runstadler. The structure of turbulent boundary layers. *Journal of Fluid Mechanics*, 30(04):741–773, 1967.

[144] W. K. George. Asymptotic effect of initial and upstream conditions on turbulence. *Journal of Fluids Engineering*, 134(6):061203, 2012.

[145] P. B. V. Johansson, W. K. George, and M. J. Gourlay. Equilibrium similarity, effects of initial conditions and local Reynolds number on the axisymmetric wake. *Physics of Fluids (1994-present)*, 15(3):603–617, 2003.

[146] P. B. V. Johansson and W. K. George. The far downstream evolution of the high-Reynolds-number axisymmetric wake behind a disk. Part 1. single-point statistics. *Journal of Fluid Mechanics*, 555:363–385, 2006.

[147] P. C. Babu and K. Mahesh. Upstream entrainment in numerical simulations of spatially evolving round jets. *Physics of Fluids*, 16(10):3699–3705, 2004.

[148] D. K. Bisset, J. C. R. Hunt, and M. M. Rogers. The turbulent/non-turbulent interface bounding a far wake. *Journal of Fluid Mechanics*, 451:383–410, 2002.

[149] M. van Reeuwijk and M. Holzner. The turbulence boundary of a temporal jet. *Journal of Fluid Mechanics*, 739:254–275, 2014.

[150] K. Chauhan, J. Philip, C. M. de Silva, N. Hutchins, and I. Marusic. The turbulent/non-turbulent interface and entrainment in a boundary layer. *Journal of Fluid Mechanics*, 742:119–151, 2014.

[151] K. Chauhan, J. Philip, and I. Marusic. Scaling of the turbulent/non-turbulent interface in boundary layers. *Journal of Fluid Mechanics*, 751:298–328, 2014.

[152] J. A. Sillero, J. Jiménez, and R. D. Moser. One-point statistics for turbulent wall-bounded flows at Reynolds numbers up to $\delta^+ \approx 2000$. *Physics of Fluids (1994-present)*, 25(10):105102, 2013.

[153] A. Segalini and P. Inghels. Confinement effects in wind-turbine and propeller measurements. *Journal of Fluid Mechanics*, 756:110–129, 2014.

[154] R. E. Wilson. Aerodynamic behavior of wind turbines. *Wind Turbine Technology*, pages 231–232, 1994.

[155] S. Jessup, D. Fry, and M. Donnelly. Unsteady propeller performance in crashback conditions with and without duct. In *Proceedings of the 26$^{\text{th}}$ Symposium on Naval Hydrodynamics, Rome, Italy*, 2006.

[156] R. Hecker and K. Remmers. Four quadrant open-water performance of propellers 3710, 4024, 4086, 4381, 4382, 4383, 4384 and 4426. Technical Report PNSRADC 417-H01, David Taylor Naval Ship Research and Development Center, 1971.

[157] P. Chang and M. Marquardt. Private communication, 2016.

[158] J. Jeong and F. Hussain. On the identification of a vortex. *Journal of Fluid Mechanics*, 285:69–94, 1995.

[159] D. W. Moore. A numerical study of the roll-up of a finite vortex sheet. *Journal of Fluid Mechanics*, 63(02):225–235, 1974.

[160] R. Krasny. A study of singularity formation in a vortex sheet by the point-vortex approximation. *Journal of Fluid Mechanics*, 167:65–93, 1986.

[161] M. J. Shelley. A study of singularity formation in vortex-sheet motion by a spectrally accurate vortex method. *Journal of Fluid Mechanics*, 244:493–526, 1992.

[162] L. E. M. Lignarolo, D. Ragni, C. Krishnaswami, Q. Chen, C. J. S. Ferreira, and G. J. W. Van Bussel. Experimental analysis of the wake of a horizontal-axis wind-turbine model. *Renewable Energy*, 70:31–46, 2014.

[163] L. E. M. Lignarolo, D. Ragni, F. Scarano, C. J. S. Ferreira, and G. J. W. van Bussel. Tip-vortex instability and turbulent mixing in wind-turbine wakes. *Journal of Fluid Mechanics*, 781:467–493, 2015.

[164] R. Muscari, A. Di Mascio, and R. Verzicco. Modeling of vortex dynamics in the wake of a marine propeller. *Computers & Fluids*, 73:65–79, 2013.

[165] S. Muppidi and K. Mahesh. DNS of transition in supersonic boundary layers. *AIAA Paper*, 4440, 2010.

Appendix A

Numerical tripping of boundary layer

In this appendix, the tripping strategy employed in the hull simulations reported in Chapter 4 is described. A brief description of the employed numerical tripping is given in Section A.1, followed by a discussion on the test cases performed to assess the effectiveness of the tripping strategy in Section A.2.

A.1 Description

The hull simulations reported in Chapter 4 are based on the experiments of Jiménez et al. [47], who tripped the hull boundary layer using a trip wire at $0.75D$ downstream from the nose, where D is the maximum diameter of the hull. The trip wire used in the experiments was very thin compared to the diameter of the hull, hence resolving it on a computational grid is not feasible. In flow solvers using body-fitted grids, the boundary layer can be tripped by manipulating the boundary condition at the desired location on the wall. For example, Muppidi and Mahesh [165] performed DNS to study transition to turbulence in a supersonic boundary layer under periodic blowing and suction. The

wall-normal velocity (v) prescribed at the desired location on the wall was

$$v = Af(x)g(z)h(t) \tag{A.1}$$

where, x and z are the streamwise and the spanwise coordinates respectively and A is the amplitude. f and g are the streamwise and the spanwise dependences of v respectively, and $h(t)$ is a temporal jitter with zero mean. In the present study, v is modified as

$$v = Ah(t), \tag{A.2}$$

and employed over few cells around the desired location. Before employing this tripping on the hull simulations, numerous validation tests were conducted, varying both A and h, on the mid (ZPG) and the bow (FPG) portions of the hull to assess the tripping strategy.

A.2 Validation

Simulations of flow over the mid portion of the hull alone were performed using LES, to assess the tripping strategy. Recall that the hull is 14.29 units long and the mid portion has negligible pressure gradient. Only a portion of the hull ($8 < x < 11$) was used for these tripping tests. Separate simulations were performed with the boundary layer tripped at $x = 8.5$ with a steady tripping ($h = 1$) and $A = 1$, 2, 3 and 5 percent of the freestream velocity. It was found that the boundary layer did not turn turbulent for $A < 2$ percent. The profiles of mean streamwise velocity at $x = 10$ on the hull are compared to the theoretical values [29] for both $A = 3$ and 5 percent steady tripping cases in Figures A.1(a) and (b) respectively. Clearly, a steady tripping of 5 percent quickly turned the hull boundary layer turbulent, as observed in the instantaneous streamwise velocity field shown in Figure A.2. The spatial growth of the hull boundary layer is also evident.

The hull simulations of Chapter 4 require the boundary layer to be tripped on the bow at $0.75D$ from the nose. Hence, additional tripping tests were performed for the

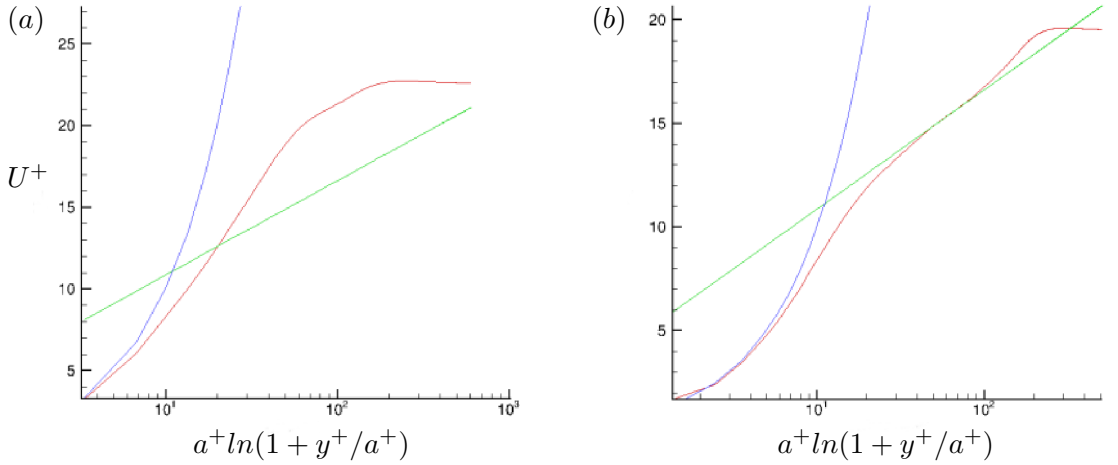

Figure A.1: Mean streamwise velocity profiles at $x = 10$ for 3 (a) and 5 (b) percent steady tripping compared to the theoretical prediction for thin axisymmetric TBL [29].

bow portion of hull, which is a region of FPG. The flow over the bow portion of the hull alone with is simulated with tripping at $0.75D$. Both steady ($h = 1$) and unsteady ($h = h(t)$) tripping tests were performed with identical A (5 percent) to assess tripping strategy. For the unsteady tripping, h was chosen to be sinusoidal in time at a desired frequency and random phase i.e. $h = sin(2\pi(24t + \phi))$, where $-1 \leq \phi \leq 1$ is random number. The results for the steady and the unsteady tripping cases are compared to each other in Figures A.3 and A.4, where the isocontours of Q-criterion [141] colored with vorticity magnitude and instantaneous streamwise velocity in xy plane are shown. Clearly, steady tripping seems more effective compared to the unsteady case. Next, C_p and C_f for the two cases are compared to the experiments of Huang et al. [46] in Figure A.5. C_p is relatively insensitive to the applied tripping. However, the plots of C_f clearly show that steady tripping is more effective. Note that even higher frequency for unsteady tripping were also tested (not shown here), which were not effective.

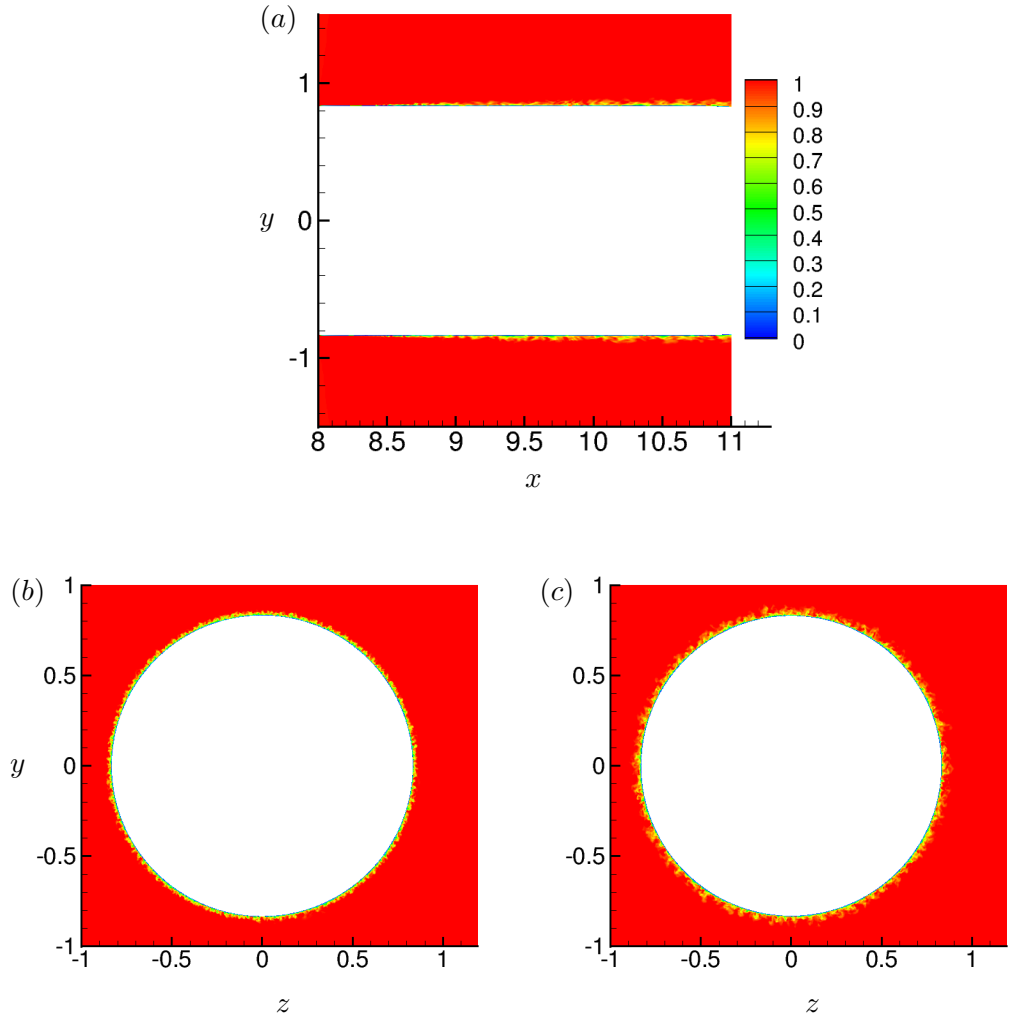

Figure A.2: Instantaneous streamwise velocity field shown in xy plane (a) and the yz planes at $x = 9$ (b) and $x = 10.9$ (c) for the flow over the mid portion of the hull tripped at $x = 8.5$ with 5 percent steady tripping.

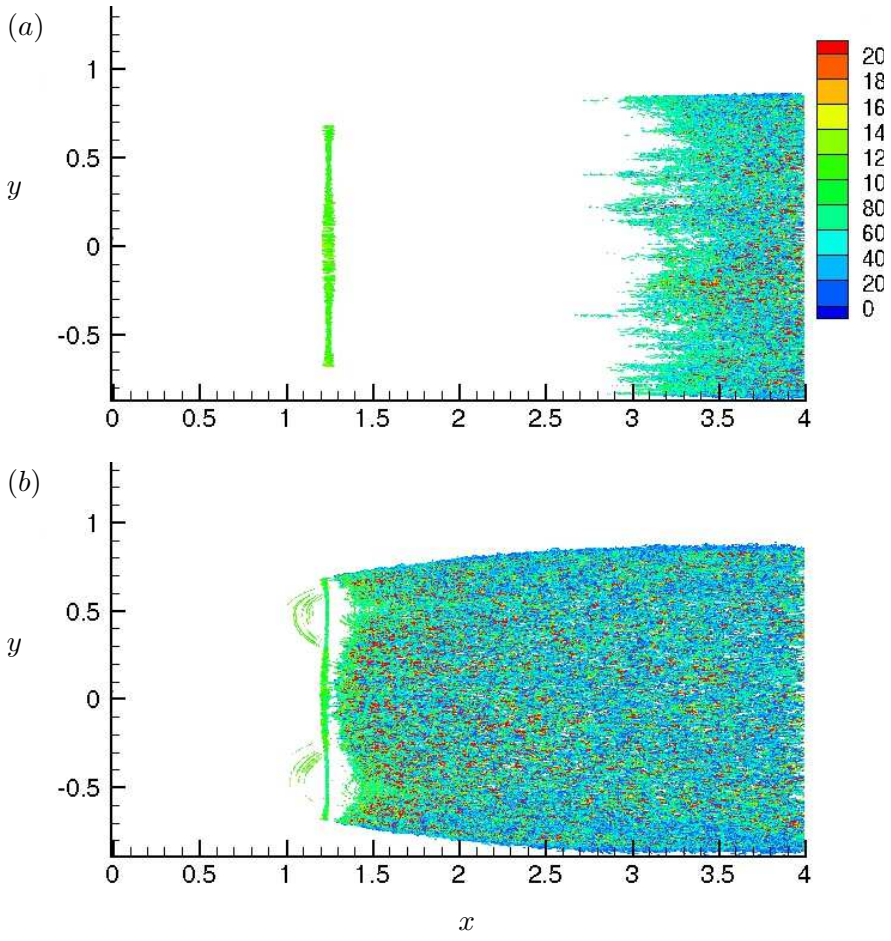

Figure A.3: Instantaneous near-wall flow structures visualized using isocontours of Q-criterion [141] colored with vorticity magnitude for the unsteady (a) and the steady (b) tripping.

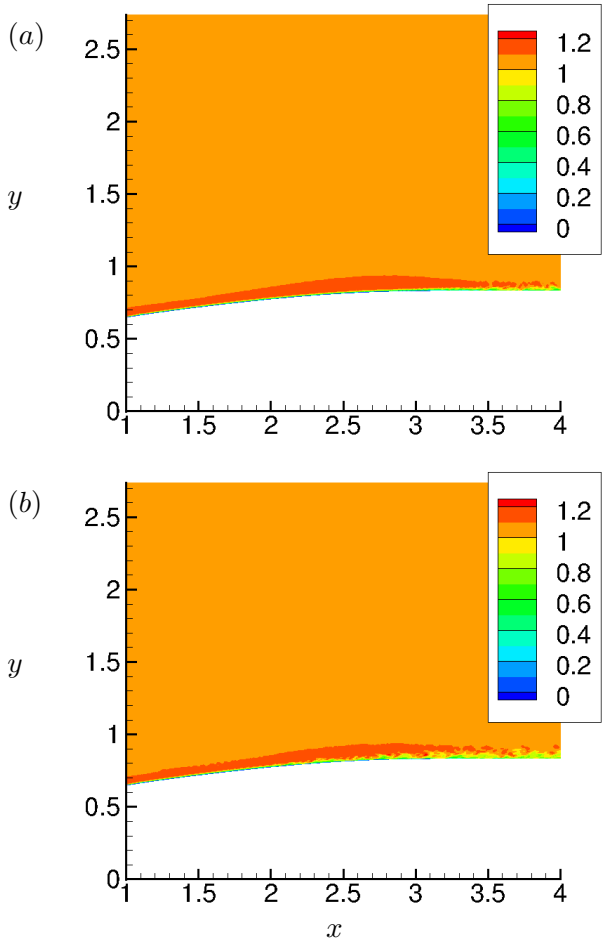

Figure A.4: Instantaneous streamwise velocity in xy plane for the unsteady (a) and the steady (b) tripping.

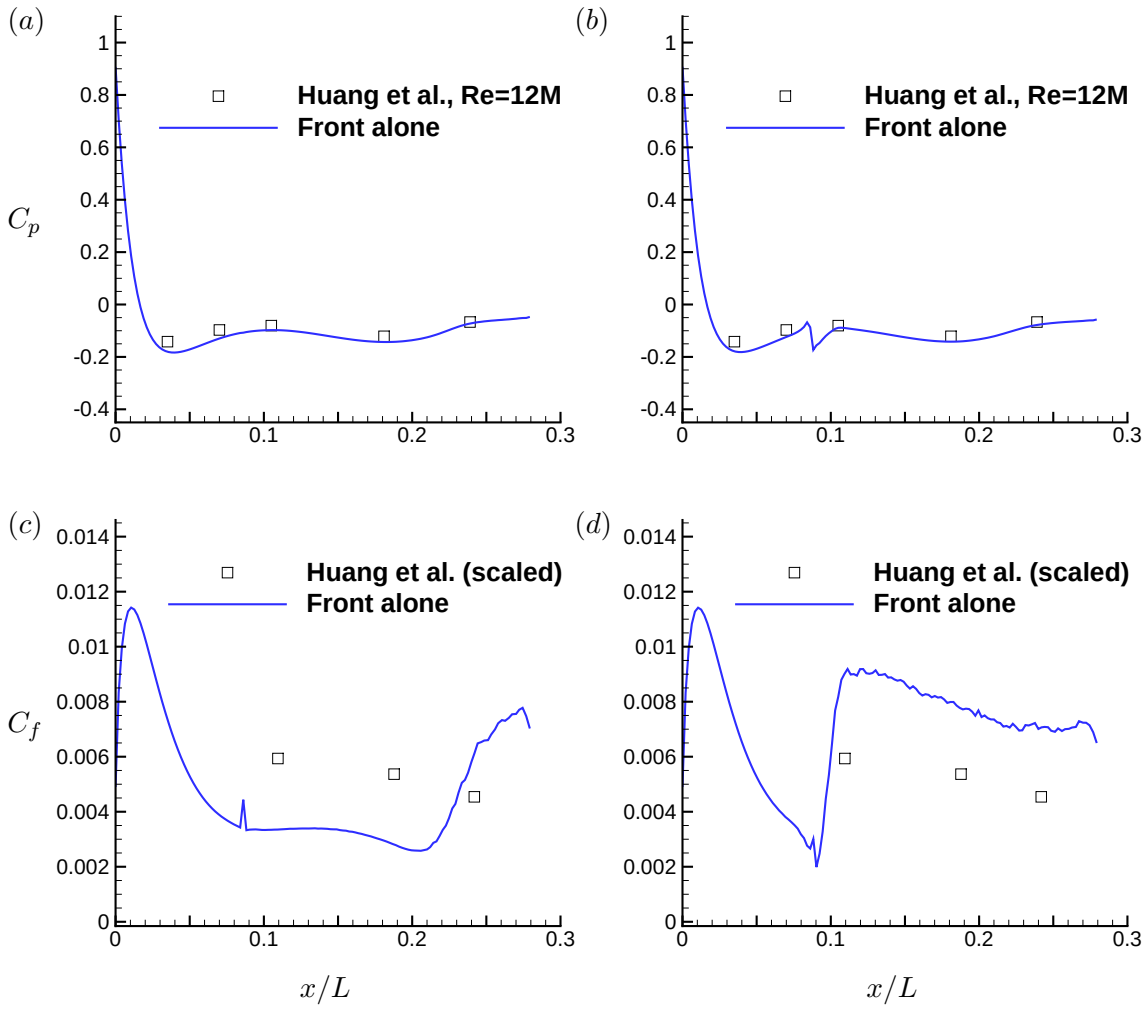

Figure A.5: Comparisons of pressure (C_p) (a,b) and skin-friction (C_f) (c,d) coefficients with the experiments of Huang et al. [46] for the unsteady (a,c) and the steady (b,d) tripping.